TUDelft

Delft University of Technology

Power Electronic Converter for an Electroactive Polymer-based Wave Energy Harvester

Todorcevic, Todor

Important note
To cite this publication, please use the final published version (if applicable).
Please check the document version above.

Power Electronic Converter for an Electroactive Polymer-based Wave Energy Harvester

Power Electronic Converter for an Electroactive Polymer-based Wave Energy Harvester

Dissertation

for the purpose of obtaining the degree of doctor
at Delft University of Technology
by the authority of the Rector Magnificus, Prof.dr.ir. T.H.J.J. van der Hagen,
chair of the Board for Doctorates
to be defended publicly on
Wednesday 21 November 2018 at 15:00 o'clock

by

Todor TODORČEVIĆ

Master in Electrical and Computer Engineering, University of Novi Sad, Serbia
born in Valjevo, Serbia

This dissertation has been approved by the promotors.

Composition of the doctoral committee:
Rector Magnificus   chairperson
Prof.dr. J.A. Ferreira   Delft University of Technology, promotor
Prof.dr.ir. P. Bauer   Delft University of Technology, promotor

Independent members:
Prof.ir C.G.E. Wijnands   Eindhoven University of Technology
Prof.ir P.T.M. Vaessen   Delft University of Technology
Prof.dr V. Katić   University of Novi Sad
Prof.dr.ir A.H.M. Smets   Delft University of Technology
Dr.ir. H. Polinder   Delft University of Technology

To my family.

Contents

Summary

Background and motivation

Utilization of renewable energy sources becomes vital for sustainable development as demand for energy is increasing, the Earth's natural resources are decreasing while the environment is affected with the associated damage. Less than 23% of globally produced electricity is from renewable energy sources and this has to be increased in the coming years.

Among the renewable energy sources, the ocean energy is one of the most unexploited, even though it exists in many of forms: wave, tidal, current, etc. When comparing wave energy with other major renewable energy sources (wind and photovoltaic energies), its biggest advantage lies in that it offers the highest energy density. Considering this variety of forms, we could think of many ways to harvest the ocean energy. However, not many methods shown reliable and/or efficient ocean energy harvesting in real-world conditions, i.e. in the harsh sea environment. Over the last decades, extensive research has been done to develop wave energy converters. Many of wave energy converter concepts are patented, but their technologies are relatively immature compared with other renewable energy technologies.

A new concept for wave energy harvesting, named S3, is under investigation in the recent years by the SBM Offshore company. The whole structure is based on a dielectric electro active polymer material. The S3 concept does not require intermediate mechanical conversion stages or interfaces; it is directly connected to the power electronics converter, as it acts as a variable capacitor from an electrical point of view.

Main Goals

This thesis deals with the new approach for harvesting renewable energy from sea waves. The main research problem is finding a way to efficiently extract the energy of the sea waves with the S3 concept using power electronics converter. The required operational high voltage of the generator limits the choice of possible power electronic converter topologies that can be employed, while a wide converter's power range is imposed with the pulsed character. A large amount of energy is circulating in the system, consequently, power electronics conversion losses are making a substantial impact on the produced power. Therefore, the efficiency of the power converter has to be optimized over the whole operating area to reduce overall losses.

The first step in this thesis research is to determine electrical parameters that will be used as a starting point for the investigation of the power electronics. Based on these, the most suitable power electronics converter topology is selected. Several different topologies are presented and evaluated in order to reveal the optimal solution. To verify the selected power electronics converter, an experimental test setup is designed and assembled in the laboratory environment.

Power converter topology survey

To satisfy the requirements for the constant electric-field energy harvesting method using dielectric elastomers, several topologies are reviewed while three are selected for further detailed investigation and comparison. The topologies studied are: two-quadrant, multiphase, flying-capacitor multilevel, diode-clamped multilevel, cascaded multilevel, modular multilevel dc-dc converters, as well as some of their variations.

A special comparison framework is created and presented to perform a comparison of different power electronic converter topologies and to satisfy the application requirements. Furthermore, the initial converter design of the investigated topologies is conducted, as well as the loss estimation and definition of the converter efficiency during harvesting cycle. Comparison results show that the cascaded multilevel converter is the most suitable topology for the dielectric elastomer energy harvesting application. Therefore, the cascaded multilevel converter, with dual active bridge modules in basis, is chosen for further development and testing.

Converter optimization and loss estimation

Following the topology study, the selected power electronics topology is input parallel output series connected modular converter, a form of cascaded multilevel converter, with dual active bridge as a main building block. The basic operation principle of the dual active bridge is presented and three other topology variations are briefly explained.

Due to great variety of dual active bridge modulation techniques, three modulations are selected and thoroughly studied: phase-shifted, trapezoidal with its two sub-modes and triangular modulation. All these modulations are presented through mathematical expressions, switching pattern, and calculated operation areas. Variable frequency modulation is further introduced to extend operation area of the modulations methods at low voltage output levels and, thus, help to deliver whole required voltage-current range of the application.

Loss modelling is carried out to provide preliminary efficiency results and for comparison purposes. Modelled power losses of the converter module consist of: conduction losses of switches, switching losses, transformer losses and power given by auxiliary power supplies for electronics. Both zero-voltage and zero-current switching behavioural are taken into account in the loss calculations.

To deliver the optimized efficiency of the dual active bridge and the dc-dc multilevel converter as a whole, a comparison of the represented modulations is carried out. Using the calculated losses and limitations of each dual active bridge modulation mode, a new modulation method is provided, which is a hybrid modulation. Three areas of operation are distinguished for the entire voltage and current ranges: I sub-mode, II sub-mode trapezoidal and triangular. Furthermore, the hybrid modulation method ensures that the efficiency is high at any operating point, therefore resulting in less losses during the energy harvesting cycles.

Since the proposed input parallel output series multilevel power electronic converter has a modular topology, individual control of the modules can improve efficiency at the lower DEAP generator voltage levels, which is shown through the calculated efficiency curves. The proposed individual module control method combines two different module control modes, thus, creating a hybrid module control.

Experiment results

An experimental test setup is assembled to validate design constraints and loss model. To overcome high-voltage isolation demand, all switches are controlled using optical fibres and power is supplied to auxiliary electronics via isolated supply system. In the first step, single dual active bridge module is built that consists of Si-based IGBT switches, while later these switches are changed with the 2nd generation of SiC-based MOSFETs. Overall, up to 50% less power loss is observed when SiC MOSFETs are used instead of Si IGBTs.

Efficiency is measured on the single module test setup and compared with the calculated values derived from the developed loss model. Further, the test setup is extended to three modules forming the input parallel output series-connected converter. The maximum reached voltage at the output is 2.2 kV, while the total power is 11 kW.

As for future work recommendations, investigation could be done on implementation of additional modulation approaches for the dual active bridge module that could result in a higher power electronic converter efficiency if coupled with optimal switch technology. Next, more improvements can be done in the loss estimation model, specifically in the switch and magnetics loss characterisations. Additionally, design of the dual active bridge module would need improvements to respect specific insulation and EMC standards. Furthermore, a suggestion is to develop an optimized harvesting cycle method according to power electronics converter efficiency curves as the input parameter. This approach is reasonable due to the fact that it is easier to change harvesting cycle than the efficiency of the power electronics converter.

Todor Todorčević

Samenvatting

Achtergrond en motivatie

Door de toenemende vraag aan energie wordt het gebruik van hernieuwbare energiebronnen van vitaal belang voor een duurzame ontwikkeling, ondertussen nemen de natuurlijke hulpbronnen van de aarde af terwijl de omgeving wordt aangetast met de bijbehorende schade. Minder dan 23% van de wereldwijd geproduceerde elektriciteit is afkomstig van hernieuwbare energiebronnen en dit moet de komende jaren worden verhoogd.

Onder de hernieuwbare energiebronnen is oceaanenergie een van de meest onbenutte, hoewel deze in vele vormen bestaat: golf, getij, stroming, enz. Vergeleken met andere belangrijke hernieuwbare energiebronnen (wind- en fotovoltaïsche energieën), heeft golfenergie de grootste energiedichtheid . Gezien deze verscheidenheid aan vormen, kunnen we veel manieren bedenken om deze te werven. Echter, in de werkelijkheid blijken veel van deze werkwijzen niet betrouwbaar of inefficiënt. In de afgelopen decennia is uitgebreid onderzoek gedaan naar de ontwikkeling van golfenergieomvormers. Veel van de concepten voor golfenergieomvormers zijn gepatenteerd, maar hun technologieën zijn relatief onrijp in vergelijking met andere technologieën voor hernieuwbare energie.

Een nieuw concept voor het werven van golfenergie, genaamd S3, wordt de laatste jaren door het SBM Offshore-bedrijf onderzocht. De gehele structuur is gebaseerd op een diëlektrisch elektroactief polymeermateriaal. Het S3-concept vereist geen tussenliggende mechanische conversiefasen of interfaces; het is direct verbonden met de vermogenselektronica-omvormer, aangezien het werkt als een variabele condensator vanuit een elektrisch oogpunt.

Belangrijkste Doelen

Dit proefschrift behandelt de nieuwe aanpak voor het werven van hernieuwbare energie uit zeegolven. Het belangrijkste onderzoeksprobleem is het vinden van een manier om de energie van de zeegolven efficiënt te onttrekken met behulp van een vermogenselektronica-omvormer gebaseerd op het S3 concept. De vereiste operationele hoogspanning van de generator beperkt de keuze van mogelijke omvormer-topologieën die kunnen worden gebruikt, bij een breed vermogensbereik van de omzetter met een gepulseerd karakter. Er circuleert een grote hoeveelheid energie in het systeem, waardoor conversieverliezen een aanzienlijke invloed hebben op het geproduceerde vermogen. Daarom moet de efficiëntie van de stroomomvormer over het gehele werkgebied worden geoptimaliseerd om totale verliezen te verminderen.

De eerste stap in dit proefschrift onderzoek is het bepalen van de elektrische parameters die zullen worden gebruikt als een startpunt voor het onderzoek naar de

vermogenselektronica. Op basis hiervan wordt de meest geschikte omvormer-topologie geselecteerd. Verschillende topologieën worden gepresenteerd en geëvalueerd om de optimale oplossing te onthullen. Om de geselecteerde vermogenselektronica-omzetter te verifiëren, is een experimentele testopstelling ontworpen en samengesteld in het laboratorium.

Omvormer topologie onderzoek

Verschillende topologieën zullen worden vergeleken, om zo te kunnen oordelen of deze voldoen aan de vereisten van de wervingsmethode met een constant elektrisch veld gebruikmakende van diëlektrische elastomeren. Hiervan zullen drie topologieën worden geselecteerd voor nader onderzoek. De bestudeerde topologieën zijn: twee-kwadrant, meer fase, vliegende condensator multi level, diode-geklemd multi level, cascade multi level, modulaire multi level gelijkstroom omvormers, evenals enkele van hun variaties.

Een speciaal vergelijkingsraamwerk wordt gemaakt en gepresenteerd om de verschillende omvormer topologieën te kunnen vergelijken en om te voldoen aan de toepassingsvereisten. Verder wordt het initiële ontwerp van de onderzochte topologieën uitgevoerd, evenals de afschatting van de verliezen en definitie van de efficiëntie van de converter tijdens de werving cyclus. Na vergelijking blijkt dat de gecascadeerde multi level-omvormer de meest geschikte topologie is voor het werven van energie gebruikmakende van diëlektrische elastomeren. Daarom is de gecascadeerde multi level-omvormer, met dubbele actieve brugmodules aan de basis, gekozen voor verdere ontwikkeling en testen.

Optimalisatie van de omvormer en verlies afschatting

Na de topologiestudie, is de omvormer met een parallel geschakelde ingang en een serie geschakelde uitgang, een vorm van een cascade multi level converter gekozen. Deze omvormer heeft een dubbele actieve brug als hoofdbouwsteen. Het basiswerkingsprincipe van de dubbele actieve brug wordt gepresenteerd en drie andere topologievariaties worden kort toegelicht.

Vanwege de vele modulatietechnieken voor dubbele actieve bruggen, worden drie modulaties geselecteerd en grondig bestudeerd: in fase verschoven, trapeziumvormig inclusief twee submodi en driehoeks modulatie. Al deze modulaties worden gepresenteerd via wiskundige uitdrukkingen, schakelpatronen en berekende operatiegebieden. Verder wordt variabele frequentiemodulatie geïntroduceerd om het werkingsgebied van de modulatiewerkwijzen bij lage spanning niveaus uit te breiden en hiermee te helpen met het bereiken van het vereiste spanning en stroombereik

Verliesmodellering wordt uitgevoerd om voorlopige efficiëntieresultaten te verschaffen en voor vergelijkingsdoeleinden. Gemodelleerde vermogensverliezen van de omvormer bestaan uit: geleidingsverliezen van schakelaars, schakelverliezen, transformatorverliezen en vermogen gegeven door hulpvoedingen voor elektronica. Zowel nulspanning als nulstroom schakelgedrag worden meegenomen in de verliesberekeningen.

Om de geoptimaliseerde efficiëntie van de DAB en de dc-dc multi level-omvormer als geheel te leveren, wordt een vergelijking van de weergegeven modulaties uitgevoerd. Met behulp

van de berekende verliezen en beperkingen van elke DAB-modulatiemodus, wordt een nieuwe modulatiemethode verschaft, die een hybride modulatie is. Drie werkingsgebieden onderscheiden zich voor het gehele spannings- en stroom bereik: I submodus, II submodus trapeziumvormig en driehoekig. Bovendien zorgt de hybride modulatiemethode ervoor dat de efficiëntie op elk werkpunt hoog is, wat resulteert in minder verliezen tijdens de energiewervingscycli.

Omdat de voorgestelde IPOS multi level omvormer een modulaire topologie heeft, kan bij lagere DEAP-generatorspanningsniveaus de efficiëntie worden verbeterd door de modules individueel te regelen, dit wordt aangetoond door de berekende efficiëntiecurven. De voorgestelde individuele regelmethode combineert twee verschillende regelingsmodi, waardoor een hybride moduleregeling wordt gecreëerd.

Experimentele Resultaten

Een experimentele testopstelling is samengesteld om de ontwerpbeperkingen en het verliesmodel te valideren. Om de vraag naar hoogspanningsisolatie te voorkomen, worden alle schakelaars aangestuurd met behulp van optische kabels en wordt de voeding via geïsoleerde voedingssystemen aan hulpelektronica geleverd. In de eerste stap wordt een enkele dubbele actieve   brug module gebouwd die bestaat uit IGBT-switches gebaseerd op Si, terwijl later deze switches worden vervangen met de tweede generatie op SiC gebaseerde MOSFET's. In totaal wordt tot 50% minder vermogensverlies waargenomen wanneer SiC MOSFET's worden gebruikt in plaats van Si IGBT's.

De efficiëntie van een enkele module wordt gemeten bij de testopstelling en vergeleken met de berekende waarden afgeleid van het ontwikkelde verliesmodel. Verder is de testopstelling uitgebreid naar drie modules die de in serie verbonden omvormer met parallelle uitgang vormen. De maximaal bereikte spanning aan de uitgang is 2,2 kV, terwijl het totale vermogen 11 kW is.

Wat toekomstige werkaanbevelingen betreft, zou onderzoek kunnen worden gedaan naar de implementatie van aanvullende modulatiebenaderingen voor dubbele actieve brug modules die zouden kunnen resulteren in een hogere elektronische efficiëntie van de converter, in combinatie met optimale schakeltechnologie. Vervolgens kunnen er meer verbeteringen worden aangebracht in het verliesschattingsmodel, met name in de karakteristieken van de schakelaar en magnetisch verlies. Bovendien zou het ontwerp van de module met twee actieve modules verbeteringen vereisen om specifieke isolatie- en EMC-normen te respecteren. Verder wordt het aanbevolen om een geoptimaliseerde wervingscycli methode te ontwikkelen met de omvormer efficiëntiecurven als invoerparameter. Deze benadering is redelijk vanwege het feit dat het gemakkelijker is om de wervingscyclus te veranderen dan de efficiëntie van de omvormer.

Todor Todorčević

Chapter 1

Introduction

1.1 RENEWABLE ENERGY

The utilization of renewable energy sources is vital for sustainable development as demand for energy is increasing and Earth's natural resources are diminishing, while the associated damage to the environment is substantial. Furthermore, renewable energy sources ensure the security of a sustainable energy supply and can help improve industrial competitiveness [1].

Figure 1.1 shows that 73.5% of the globally produced electricity is from non-renewable sources and has to be reduced significantly in the coming years. One of the first political organizations to recognize and take actions in this field is the European Union, which set a goal to increase the electricity generated by renewable technologies to 20% of the total energy consumption by year 2020 [1] and to 27% by year 2030 [2]. With the help of European government-supported projects, major investments are planned in the field of renewable energy.
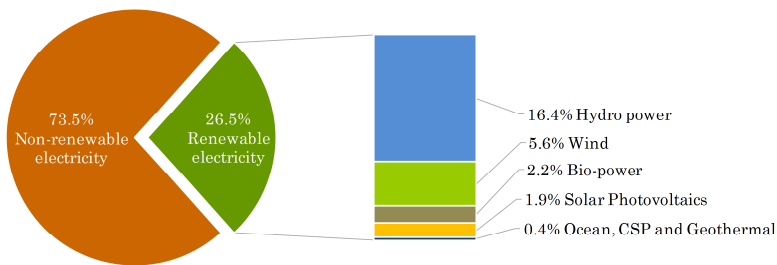
Figure 1.1: Estimated renewable energy share of global electricity production for 2017 [3]

Figure 1.1 shows that hydropower is widely applied as a source of electricity [3]. On the other hand, ocean energy is one of the most underrated, and so far, unexploited energy sources. The ocean energy contributed only 1.1 TWh, while total world-wide energy production was 25,518 TWh for the year 2017. Ocean energy exists in different forms including: wave (kinetic and potential energy), current (kinetic energy of flowing ocean currents), tidal (from the rises and ebbs of tides), thermal (utilizing the natural temperature gradient as a function of depth in tropical oceans) and salinity (chemical electric potential formed by the difference in salt concentrations between fresh water and sea water) [4].

Considering the variety of ocean energy forms, there are many ways to harvest energy, transform it into a desirable form and transport it to the final consumer. Many research projects are conducted to find the most efficient method to convert the mechanical energy of waves into electricity [5-8]. Usually, these conversion systems consist of many mechanical sub-systems, including linear hydraulic actuators, hydraulic motors, valves and accumulators. After transforming wave energy into a suitable mechanical energy, a hydraulic motor drives an electrical generator. The electrical generator role is to finally

produce electricity and to supply it to the electrical grid. In some cases, to keep the generator rotating at the same speed, necessary to produce 50 Hz, mechanical sub-systems are employed including valves to rectify the bi-directional fluid flow and hydraulic accumulators to provide a smoothing effect for the hydraulic motor. To decrease the number of mechanical parts, power electronic converters can be employed. Thanks to them, it is possible to connect the electrical generator to the mechanical system avoiding many mechanical sub-systems, while the control system is substantially simpler.

1.2 WAVE ENERGY CONVERTER CONCEPTS

Because of the differential heating of the Earth's surface by solar energy, winds are created. As winds blow over water, they create waves and transfer their energy into them. The amount of energy transferred depends on the wind speed, time applied, and distance covered. The world's potentially exploitable wave power resource is on the order of 1 TW [9]. Like most forms of renewable energy sources, wave energy is distributed unevenly over the world. The following regions offer the highest wave energy potentials over the globe: the Western European coast, the coasts of Canada and the United States, and the south-western coasts of Australia, New Zealand, South America, and South Africa [10], see Figure 1.2. When comparing wave energy with other major renewable energy sources (wind and photovoltaic energies), its biggest advantage lies in that it offers the highest energy density [11]. Another important factor is that wave energy represents a more constant and predictable energy source. Compared with the above-mentioned renewable energy sources, a negative environmental impact is also noticeably less for wave energy [12]. In addition, waves have a unique feature, i.e., they can travel large distances with little energy loss (if they do not encounter head winds) [5].
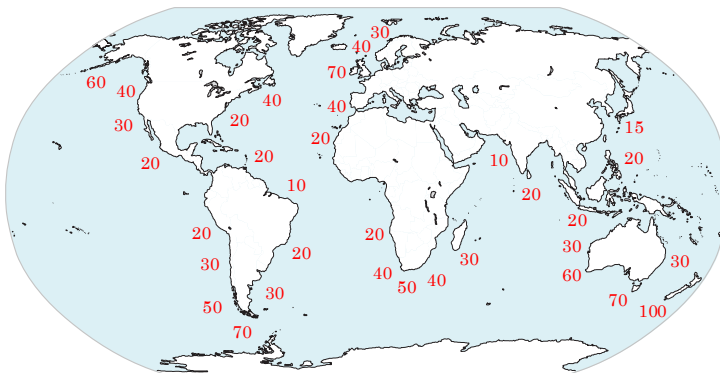
Figure 1.2: Global wave power distribution in kW/m of wave crest length [10]

The devices comprising the mechanical actuator that captures the energy from the waves are called wave energy converters (WECs). Over the last 30 years, extensive research has been done to develop WECs, which are described in several surveys [4, 5, 8, 11, 13-16]. Many

WEC concepts are patented [16], but their technologies are relatively immature compared with other renewable energy technologies.

Currently, the number of existing wave energy companies approaches 100, while the number of WECs is larger. A list of the existing technologies and the leading companies can be found in [17, 18]. Here, only a few important devices are given in Table 1.1 [12].

Table 1.1: Comparison of different WEC concepts [12]

Parameter	LIMPET	Pelamis	Wave Dragon	Archimedes Wave Swing
Operation principle	Oscillating water column	Attenuator	Overtopping terminator	Point absorber
Location	Onshore	Offshore floating	Offshore floating	Offshore submerged
Power take-off	Wells turbine	Hydraulic	Hydro-turbine	Permanent magnet linear generator
Power conversion system	2 asynchronous gen.	6 asynchronous gen.	16 back-to-back conv.	Back-to-back conv.
Power quality	+	++	++	-
Development stage	++	++	+	0

1.2.1 Dielectric electroactive polymer wave energy converter

A new concept for wave energy harvesting is being investigated by the SBM Offshore company, named S3. The whole structure is based on a dielectric electroactive polymer (DEAP) material. It is planned that the farm for energy harvesting will consist of separated DEAP WECs covering an area in the sea.

The DEAP WEC consists of several DEAP generators (Figure 1.3), where each generator represents a single DEAP WEC's segment that is electrically separated and physically coupled with other segments to create a long tubular actuator. DEAP generators independently produce power via harvesting cycles that consist of charging and discharging processes during each wave period. Furthermore, each segment requires its own bidirectional high-voltage power electronic converter (PEC) to provide the electromechanical energy conversion, see Figure 1.4.

1.3 PROBLEM DEFINITION AND THESIS OBJECTIVES

This thesis deals with the new approach for harvesting renewable energy from sea waves. The DEAP WEC concept [19] has many advantages over other WEC concepts, hence, effort must be put into its further development and investigation. The DEAP WEC does not have any pistons, bearings or pressurized oil lines, and therefore, is more suited for the severe

sea environment. Furthermore, the DEAP WEC does not require intermediate mechanical conversion stages or interfaces; it is directly connected to the electrical power converter, as it acts as a variable capacitor from an electrical point of view. On the other hand, the DEAP WEC concept requires DEAP material that does not currently exist in mass production.
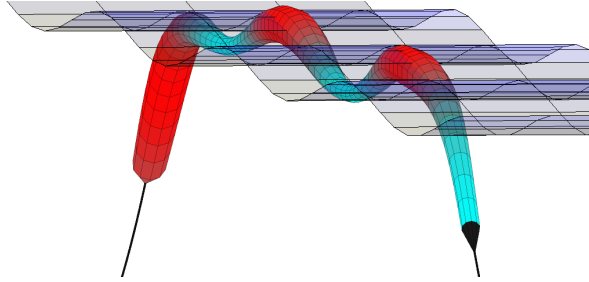
Figure 1.3: DEAP WEC comprised of DEAP generators as segments, a three-dimensional model of S3 concept
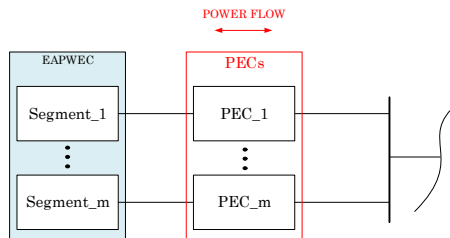
Figure 1.4: DEAP generators (DEAP WEC segments) connected to individual bidirectional high-voltage PECs

Figure 1.5 presents the DEAP WEC development stage at the beginning of this PhD research and the contribution of this thesis to the development process. At the first stage of the DEAP WEC concept investigation, an understanding of the sea wave behaviour and the modelling of the waves are required for a specific site. Next, a DEAP WEC mechanical model is developed, and its interaction with the sea waves is determined. Thus, the DEAP WEC's response to the waves is obtained, and therefore, its capacitance variations. Knowing the DEAP's capacitance variation characteristics, the required current waveform is determined for basic energy harvesting approaches. Consequently, the DEAP generator voltage and current waveforms are acquired, thus, the PEC's requirements can be defined.

The main research problem is finding a way to efficiently extract the energy using the DEAP WEC concept. The DEAP generator operation voltage reaches high values (in the range of kilovolts) because of manufacturing limitations in terms of the dielectric layer thickness. The required operational high voltage of the DEAP generator limits the choice of possible power electronic converter topologies that can be employed due to the electronic switch blocking voltage constraint. Therefore, first goal of the research is to choose the best suitable electronic power converter topology.

A large voltage and current range are covered during the harvesting cycle, implying a wide converter operating range, while the pulsed power character with a high peak to average power rating increases the converter power rating. The efficiency of the power conversion process is crucial, as it directly affects the energy production. A large amount of energy is circulating in the system, consequently, power electronic conversion losses are making a substantial impact on the produced power [20]. Therefore, the efficiency of the power electronic converter has to be optimized over the whole operating area to reduce overall losses. An analytical model should be derived to estimate overall conversion losses during harvesting cycles.

To prove the power electronic converter modulation concepts, analytical models and efficiency improvements, an experimental setup is required.

1.3.1 Thesis objectives

Thesis objectives are as follows:

- Determine power electronic converter requirements;
- Identify suitable power electronic converter topologies and select the best one based on specifications of the DEAP WEC application;
- Model the selected power electronic converter topology and its interaction with the DEAP WEC;
- Find converter operation modes to minimize overall conversion losses in the power electronic converter;
- Design and implement the power electronic converter, the proposed modulation strategy and validate loss models and modulation approaches.
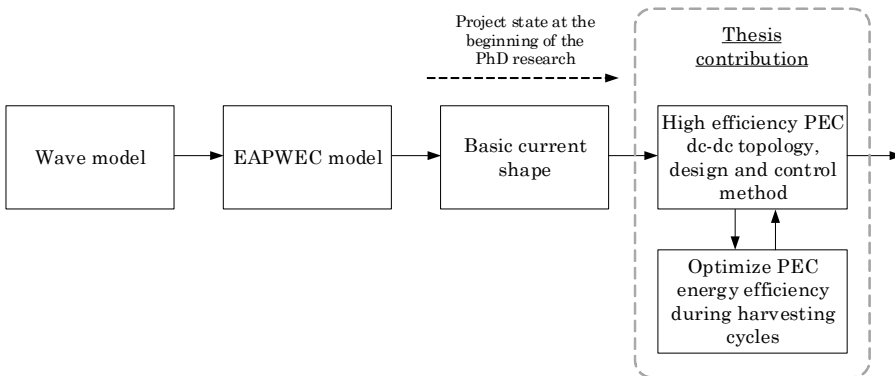
Figure 1.5: DEAP WEC concept development stages and this PhD thesis contribution

1.4 THESIS OUTLINE

Chapter 2 presents the electro active polymer method and basics of the energy harvesting. Furthermore, details about the DEAP WEC concept, electrical system definition and requirements for the dc-dc power converter stage are given.

Chapter 3 gives a power electronic converter topology study for the DEAP WEC system. An overview of dc-dc converter topologies is presented, as well as their comparison through a special framework. The loss modelling method is conducted to provide data for comparison criteria. Next, an estimation of the losses in the electrical power converter during DEAP energy harvesting is defined, as the only proper way to express converter influence on the DEAP generator energy harvesting.

Chapter 4 presents the overview of several power electronic converter modulation modes. For each of the modulation modes an analytical model is given, as well as limitations depending on the output voltage and current levels. Given the results from the topology comparison, modifications on the chosen converter are made to increase efficiency. The variable switching frequency modulation method is introduced to meet the output voltage and current requirements. This chapter also provides loss modelling results (loss distribution and efficiency curves) for the given modulation modes.

Chapter 5 presents the design and realization of a single power electronic converter module using the forced-air cooling method. Furthermore, the realized power electronic converter module is used to compare two different power switch technologies. The expected overall power electronic converter efficiency and DEAP generator energy gain are given for comparison. Furthermore, efficiency measurements are provided for the loss model validation.

Chapter 6 introduces an individual module control method as an approach for further improvement of the overall converter efficiency. A basic theoretical explanation for modular topologies is given, as well as a comparison of different module control methods with the basic example. The results of the investigation and proposed module control method are given through efficiency improvement and the converter efficiency during DEAP generator energy harvesting.

Chapter 7 gives the conclusions of the research and future work recommendations.

Chapter **2**

DEAP Energy Harvesting and Electrical System Requirements

2.1 INTRODUCTION

Nowadays, some materials are employed in the sea to transform mechanical energy into electrical energy [21]. Electro active polymers are such materials that are used as transducers. In comparison with ceramic piezoelectric materials, DEAPs can provide significantly larger strains, up to 380%, while sustaining large forces [22].

A special type of polymers are called electroactive polymers. These polymers react to an applied electric field by changing their shape or size. They are capable of transforming mechanical energy into electrical, and vice versa, depending on if it is used as an actuator or a generator. They are also used as sensors, as their deformation can be detected through the electrical capacitance change. This thesis deals with the use of DEAPs in the generator mode, thus, in this chapter are discussed DEAP material characteristics, power electronic converter (responsible for energy harvesting) requirements and the electrical system definition.

The main issues addressed in this chapter are:

- Influence of electronic power converter efficiency on energy harvesting;
- Determination of DEAP material size for the given application;
- Definition of the electrical system requirements.

2.2 DIELECTRIC ELASTOMER

The proposed DEAP WEC concept uses a dielectric electroactive polymer material that belongs to the group of electroactive polymers (EAPs), see Figure 2.1. DEAPs are fabricated using two layers of the EAP material, where one side of the each EAP is covered with a metal electrode. Each EAP layer represents an incompressible and highly deformable dielectric medium, and two EAP layers are cemented together to form a structure – DEAP, where the dielectric medium is put between two metal electrodes, see Figure 2.2. As a result, from the electrical point of view, the formed structure is a capacitor. The material used for the dielectric medium is either a silicone- or polyurethane-based polymer [23].

When the material is exposed to an electric field applied between the electrodes, the charges start to attract each other because of Coulomb forces, thus, squeezing the elastomer film. Because of the attraction of charges, a generated movement causes the elastomer to decrease in thickness and expand its lateral area [23-25]. However, the applied electric field must be limited, since the DEAP material has a breakdown electric field above which the DEAP will be destroyed. The breakdown electric field strength of the dielectric material is in the region of $30 - 100$ V/µm, while the typical thickness of the combined layers is approximately $50 - 200$ µm. Accordingly, the maximum operating voltage of the DEAP is in

the range of 1.5 – 10 kV [26-28]. Generally, the strain induced in a material is proportional to the square of the applied electric field and the dielectric constant of the material.

Figure 2.1: Roll of silicone dielectric electro active polymer
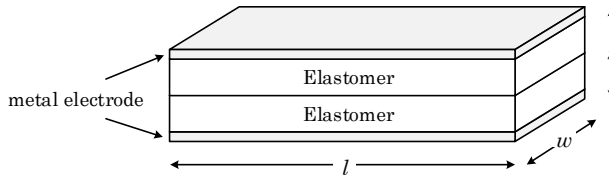
Figure 2.2: DEAP structure, formed by two electrodes and the polymer (dielectric) in between

Since the DEAP structure is highly deformable, fundamentally, it acts as a variable capacitor. The DEAP capacitance varies as the area and thickness change. Furthermore, the DEAP can operate in either actuator or generator mode. The actuator mode is described as follows: If a voltage is applied to the electrodes, electrostatic forces will squeeze the dielectric elastomer material, reducing its thickness and expanding its area. For this thesis, specifically, the generator mode is of interest. The working principle for the generator mode is the following: When the material is stretched, caused by applied excitation forces, the capacitance increases, and when the extension reaches its maximum value, charges are placed into the material (charging process). At this instant, the DEAP's area is the largest, while its thickness is the lowest. As the forces continue to influence the DEAP, the material eventually starts to contract, and when the DEAP reaches its smallest area (minimum capacitance value), a displacement of the charges takes place (discharging process). To achieve the maximum energy yield in one cycle, the charging and discharging processes should be exactly defined in line with the excitation force. Additionally, the DEAP material can be used as a sensor for strain measurements, as the strain will change its capacitance, which can be further converted to an electrical signal.

The observed DEAP structure can be seen as a parallel plate capacitor with the infinitely large area of the compliant electrodes and the polymer as the dielectric medium. Since the thickness (z) of the dielectric medium is very small compared with the total area ($A = l \cdot w$), the assumption of an infinitely large area (A) is reasonable. Therefore, the electric field can be assumed as uniformly distributed over the area A. The ideal parallel plate capacitor capacitance is given by:

$$C = \varepsilon_r \varepsilon_0 \frac{A}{z} \tag{2.1}$$

where ε_0 is the permittivity of vacuum, ε_r the relative permittivity of the dielectric, A the area, and z the thickness of the dielectric medium. In actuality, the capacitor area is not infinitely large and is defined by the compliant electrodes' overlap area. In this analysis, it is assumed that the overlap is always present.

2.2.1   Harvesting cycles

Three operation conditions can be distinguished within both actuation and generation modes, and therefore, three harvesting cycle methods are defined for the energy production [23, 29]. These conditions are constant charge, constant voltage and constant field approaches. Figure 2.3 depicts all three mentioned operation conditions. The DEAP deformation (change in area and thickness) is represented by the stretch ratio, λ ($\lambda = l/l_0$). The stretch ratio (λ) is the relation between the instantaneous (l) and initial state (l_0) of the DEAP film length, when the material is exposed to deformation. The electrostatic potential energy is a function of the electric field, V_{DE}/z , as in $E_e = 0.5 \cdot \varepsilon_r \cdot \varepsilon_0 \cdot z \cdot A \cdot \left(V_{DE}/z \right)^2$, where V_{DE} is the voltage over the DEAP.

The ideal operation principles of the constant voltage, constant charge and constant electric field harvesting cycles can be described as follows (see Figure 2.3) [29]:

- State 1: This is the stretching state. Therefore, the DEAP material is deformed due to an external excitation force, and as a result, its area is increased, while the thickness is decreased. The mechanical energy input is converted to potential energy by the elasticity of the dielectric elastomer.

- State 2: This is the charging state. At the instant when the film is maximally stretched, the capacitance of the film is the highest, and the electrical charge on the film is increased. The amount of charge placed on the DEAP film is limited by the breakdown electric field $\left(V_{DE}/z \right)_{\max}$ of the material.

- State 3: This is the relaxation state. The film contracts due to the decrease of the excitation force. Thus, the DEAP film area decreases, and the thickness increases. As the charges on the electrodes are separated from each other, the electrostatic potential energy of the DEAP is increased. Furthermore, as the film area contracts, the similar charges are compressed together, which is another mechanism behind the electrostatic potential energy increase. The term "constant", which is used in the names of the harvesting cycles, is related to the electrical performance of the DEAP during the relaxation state.

- State 4: This is the discharging state. At the instant when the film is contracted, the capacitance of the film is the lowest, and the charges are removed partially or completely.

The area enclosed by the cycle is directly proportional to the total amount of energy converted by the single cycle.
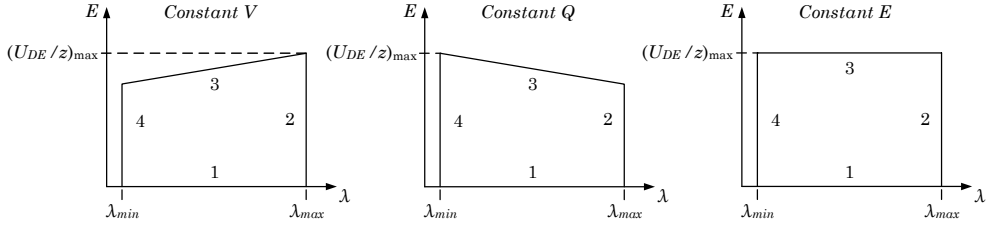
Figure 2.3: Comparing the three different DEAP harvesting cycles [29]

Ideally, for maximum energy conversion, the charging and discharging states should be infinitely short, therefore requiring the charges to be delivered and withdrawn from the DEAP with infinitely high current pulses. This is not a practical approach, since losses inside the electronic circuit performing the charging/discharging processes would be very high when high current peaks are required. Therefore, a practical solution is to limit the current, and by that, cause wider current pulses. Consequently, part of the mechanical energy is not converted, hence, affecting the energy yield. This is usually defined as conversion losses [20]. Figure 2.4 depicts one harvesting cycle (generator mode) of the DEAP with the applied constant electric field method and practical current waveform limit. The presented signals are the capacitance of the DEAP structure, voltage over the DEAP and current that charges and discharges the DEAP according to constant field operation conditions.
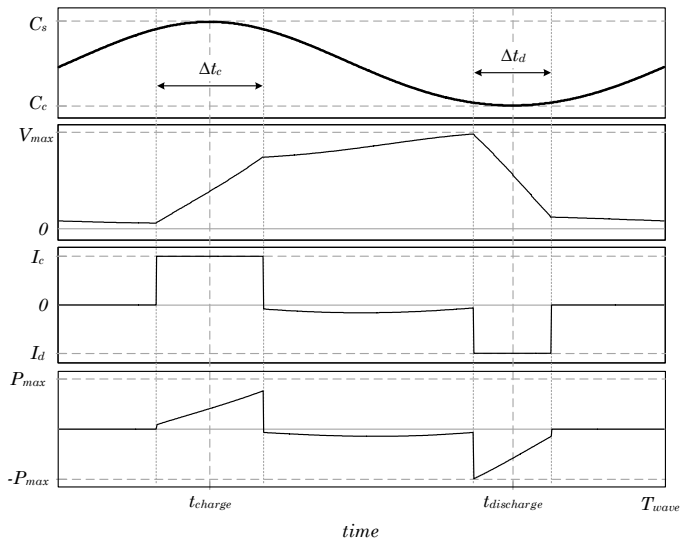
Figure 2.4: DEAP capacitance, voltage, current and power during one harvesting cycle using the constant electric field method and practical current waveform limit

2.2.1.1 *Comparison of the energy output*

Figure 2.5 presents the calculated energy output of each operation condition approach based on [29]. It is shown that the amount of converted energy is equal for the constant charge and constant voltage operation conditions. The constant electric field approach yields the highest energy output when compared with the other operation conditions, as expected. Therefore, the constant field approach will be further used for all investigations on power electronic units employed for DEAP charging and discharging processes. Note that the energy yield for the analysed operation approaches is almost equal for very small relative deformations below 40%. The reason behind this is the fact that the DEAP potential energy can be maintained almost constant and at a maximum for small deformations [29].
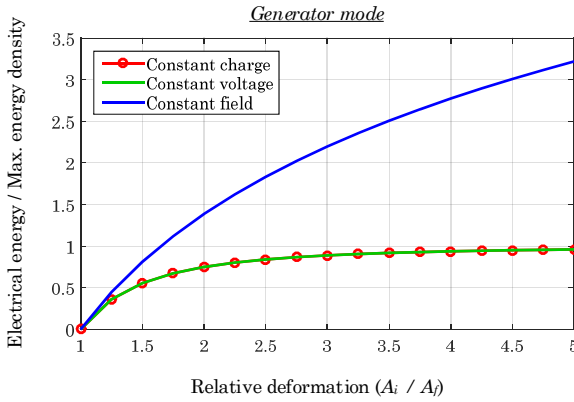
Figure 2.5: Comparison of the maximum energy conversion of the constant voltage, constant charge and constant field approaches [29]

2.2.2 **DEAP generator electrical model**

The DEAP generator is presented as a variable capacitor (C_{DE}, Figure 2.6) with series (R_s) and parallel (R_p) resistances. The capacitance (C_{DE}) and parallel resistance (R_p) change with the stretch of the material (λ), as caused by the sea waves. The stretch ratio depends on the amplitude (Λ_a), pre-stretch amplitude (Λ_0) and period of the waves as:

$$\lambda(t) = \Lambda_0 + \Lambda_a \sin(\omega t) \tag{2.2}$$

$$C_{DE} = \varepsilon_0 \varepsilon_r \frac{A_0}{z_o} \lambda^2 \tag{2.3}$$

$$R_p = \frac{z_0}{\sigma_d L_0 W_0} \frac{1}{\lambda^2} \tag{2.4}$$

$$\lambda = \frac{l}{L_0} \tag{2.5}$$

where l is the final length; and A_0, z_0, L_0, and W_0 are the initial area, thickness, length and width of the DEAP in the relaxed state, respectively. In the further analysis, R_p is considered infinite, thus, no leakage current can be observed in the DEAP structure through the parallel resistance. Series resistance R_s is combination of series resistances of metal electrodes, wires and connections.
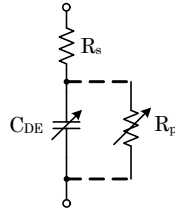
Figure 2.6: Electrical model of the DEAP generator consisting of a variable capacitor, series resistance and variable parallel resistance

2.3   DEAP WEC CONCEPT

In this section, details about the DEAP WEC concept are given. A farm for wave energy harvesting would consist of 25 separated DEAP WECs. It is estimated that each DEAP WEC device can yield up to 100 kW, thus, the whole farm can provide a maximum of 2.5 MW.

The DEAP WEC device consists of 20 segments (Figure 2.7) of rolled DEAP material. Each segment is electrically separated and mechanically coupled with other segments so they create a long tubular WEC, which is further filled with water. Segments can produce a maximum output power of 5 kW (average power of one cycle, one cycle consists mainly of charging and discharging processes).
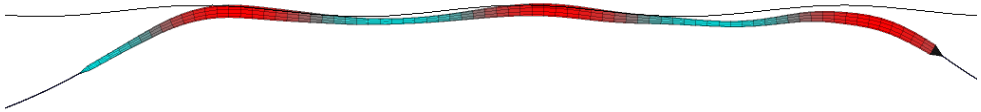
Figure 2.7: DEAP WEC (S3 concept) with created bulges that propagate with the sea waves

The planned distance for the DEAP WEC farm from the shore is 10 km. The estimated active WEC part has a length of 200 m and a diameter of 1.7 m, as preliminary indicative numbers of a device under development that will be used for initial design and optimized at a later stage. Every segment is 10 m long and 1.7 m in diameter (Figure 2.8). On both ends of the WEC, there are rigid body noses made from a rigid material. The length of the rigid body nose is ~4 m and has the same diameter as the rest of the device. The approximate volume of one rigid body nose is 7 m3, and it should be used for power electronic converters,

cable connections and the cooling system. Ten PECs are in one, and ten in the other rigid body nose of the DEAP WEC.
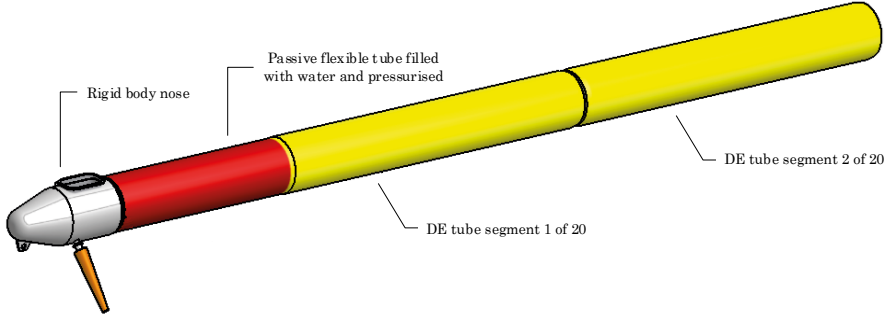
Figure 2.8: DEAP WEC device with more details on the construction: the first part is the rigid body nose, painted in red is the low-pressure part used for the stretching measurement, and painted in yellow are the power segments for energy production

Table 2.1: Summarized system and generator specifications

Parameter	Value
Power rating of DEAP WEC farm	2.5 MW
Number of DEAP WEC devices	25
Power rating of one DEAP WEC	100 kW
Distance from shore	10 km
Number of segments per DEAP WEC	20
Segment average power of one cycle	5 kW (planned)
Length of segment, w	10 m
Length of rigid body nose	4 m
Total length of DEAP WEC	208 m
DEAP WEC diameter, d	1.7 m

Determining the optimal size of the DEAP film for every segment requires the calculation and optimization of the charging/discharging process (one cycle) for a given wave. From the DEAP WEC mechanical design, it is given that segments are each 10 m long. However, the DEAP film has a thickness, width and length. The DEAP is rolled in such a way that the length of the segment is actually the width of the DEAP, as the tubular device is created using an N_t number of DEAP turns, see Figure 2.9. Therefore, only the DEAP's length must be found, since the width (length of the segment) of the DEAP is initially assumed.

The PEC's maximum current is preliminary indicated with the value of 5 A to set a reasonable ratio (ten) for maximum power to average power output of a single DEAP WEC segment. Taking into account that the maximum current of the PEC is 5 A and assuming

that the PEC's efficiency is 95%, several calculations are carried out to determine the DEAP's length. In this thesis, a certain operating area is assumed within the sea wave behaviour. The most common cycle period durations are between 4.5 s and 8 s, as marked in Figure 2.10. As for capacitance changes, the most common ratio, $(C_{max} - C_{min})/C_{av}$, is from 0.2 to 0.7. This is also important for determining the minimum voltage over the DEAP generator and the voltage range in which the efficiency of the PEC must be high. Inside this area, when the maximum PEC current is not set, the optimum calculated current is always higher than 5 A for DEAP film lengths larger than 20 m, and according to [30]. As the PEC can give a maximum of 5 A, the calculation determines the optimum residual charge while the current is held at 5 A, except for the constant electric field period when the current is very low (<1 A).
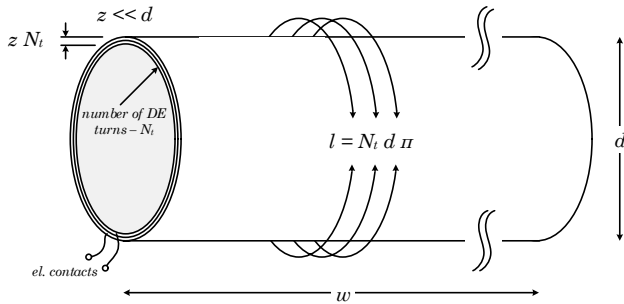
Figure 2.9: DEAP WEC segment (DEAP generator) made of a rolled DEAP film
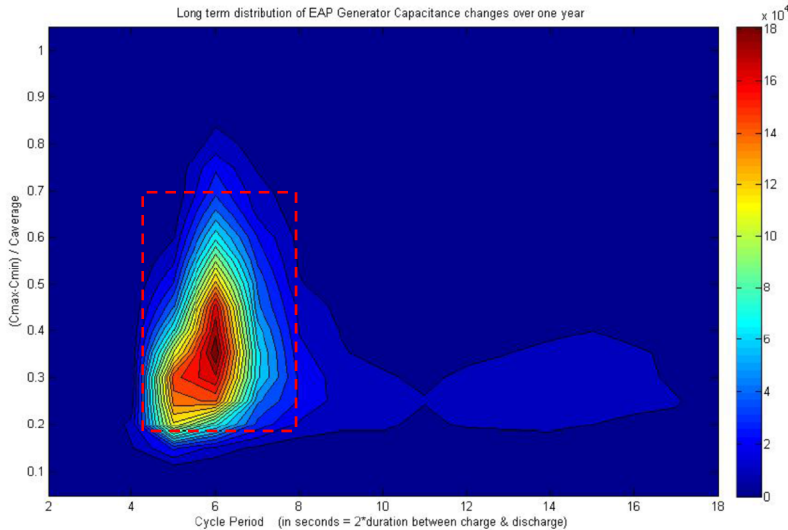
Figure 2.10: Scatter diagram of the DEAP capacitance variation and cycle (wave) periods for the specific site over one year; the area of interest is marked

Taking all the above into the calculation leads to the optimal DEAP length based on the graph results in Figure 2.11. The most common cycle period and capacitance ratio are 6 s and 0.35, respectively, as seen from Figure 2.10. The power is calculated using optimization algorithm, as given in [29], for constant electric field method, with the given cycle periods and capacitance ratio variations for corresponding sea states, which in return gives voltage and current waveforms during each cycle. It is shown that the average power density (generated average power output per volume of used DEAP film) is high for very small DEAP lengths. The reason for this is that the PEC used has a maximum 5 A current output, $I_{DE(\max)}$. As the DEAP's current optimization result, this current (5 A) is optimum for an approximate DEAP length of 20 m. However, if 20 m of film is used, the ratio of maximum PEC power rating and average produced power is very high (> 30). To decrease this ratio, a larger DEAP film has to be employed. However, in that case, the power density of the DEAP material will be sacrificed, and this is a reasonable choice as the film is less expensive than the PEC. For the DEAP film length, the chosen value is 250 m. For a given area of the capacitance states, the 250-m long DEAP always gives a positive average power output per cycle, and its average output power is close to the values of longer films, according to Figure 2.11.
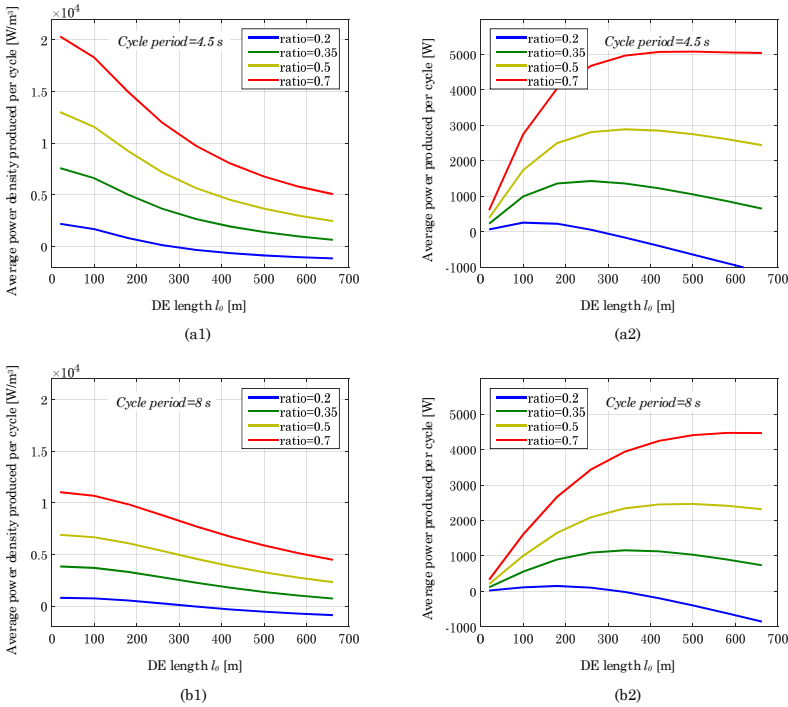
Figure 2.11: Average power density of the DEAP film and average power produced per cycle for different capacitor ratios and cycle periods of 4.5 s (a) and 8 s (b). $I_{DE(\max)}$ = 5 A, with a PEC efficiency of 95%

The series resistance of the DEAP generator can be high because of complicated electromechanical connections between the film and connection cables. Beside WEC active part dimensions and PEC maximum current, it is given that the preliminary value of the series resistance is 1 Ω of the DEAP device under development. The series resistance must be taken into account while designing the PEC because of increasing losses from possible high current ripples. Together with length, all parameters of the DEAP film that are further used are listed in Table 2.2.

Table 2.2: Parameters of the used DEAP film

Parameter	Value
Capacitance at rest, C_0	885 μF
Film area at rest, A_0	2500 m^2
Film width at rest, w_0	10 m
Relative permittivity, ε_r	6
DEAP gen. series resistance, R_S	1 Ω
Conductivity of electrodes, σ_e	$6.3*10^7$ S/m
Film thickness at rest, z_o	150 μm
Film length at rest, l_0	250 m
Maximum operating dielectric strength, E_{max}	80 V/μm
Average stretch (pre-stretch), λ_0	1.4
Conductivity of dielectric material, σ_d	$0.33*10^{-12}$ S/m
Electrode thickness, t_{el}	0.1 μm

2.4 POWER TAKE-OFF ELECTRICAL SYSTEM DEFINITION AND REQUIREMENTS

Figure 2.12 depicts the power take-off (PTO) system block diagram and the PEC's integration within the WEC system. The PEC is a part of the whole PTO system. On one side, it is directly connected to wires from the DEAP generator, and on the other side, it is connected with the rest of the PTO system. The power rating of each PEC is 50 kW with a maximum V_{DE} of 10 kV and maximum current of 5 A at the output (the maximum voltage that can appear over the DEAP generator and given maximum current through the DEAP generator). The presented PTO block diagram focuses on the power conversion, and it doesn't show, for example, wave measurement units responsible for sending data about coming sea waves. This data is used for the computation of the optimal harvesting cycle, depending on the wave period and height. Furthermore, the PEC's operation is synchronized according to the sea wave, since the precise timing of the DEAP WEC segment charging and discharging process is critical for the wave energy harvesting.
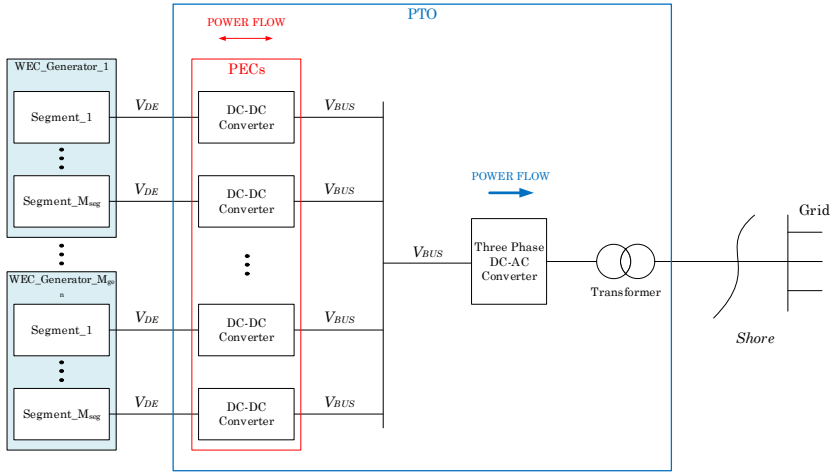
Figure 2.12: DEAP WEC and PTO system block diagram

The PEC must provide bidirectional power flow to charge and discharge the generator. This can be performed using two unidirectional converters (one for charging and another for discharging) or one bidirectional converter. Basically, two unidirectional converters occupy more space than one bidirectional converter, while the power ratings are the same. Clearly, the better solution is one bidirectional converter per generator segment because the physical location of the PEC is off-shore and inside the DEAP WEC device rigid body nose. Based on the DEAP WEC size and the generator rigid body nose volume estimation, a realistic requirement for the PEC power density would be a minimum of 1 kW/dm^3.

In the case of PEC malfunction, it must be easily accessible and changeable. Since off-shore work has a high price, a good solution would be changing the whole rigid body nose. Then, the malfunctioning PEC can be replaced at the site and later investigated and repaired on-shore. This requires a number of spare rigid body noses prepared for the case of PEC failure.

The input voltage of the PEC is the voltage of the connection with the rest of the PTO system. It is taken that the dc bus (input voltage, V_{BUS}) is in a range of up to 1 kV, and for investigation purposes in this thesis, is set to 800 V dc. In that way, it would be easy to process power and send it over a transformer to the transmission grid, using the appropriate inverters. The anticipated output power capacity of the system is rated for 2.5 MW. Taking the system power capacity into account and the distance to the shore for power transmission, a higher voltage must be used. Therefore, a transformer is employed to step-up the voltage to 11 kV. The allowed maximum deviation of the dc bus is set to 5% of the rated voltage.

The power that is delivered and withdrawn from the DEAP generator has very high peaks, as can be observed in Figure 2.4. This mainly affects the power rating of the PEC, while the average power per cycle is approximately ten times lower. Therefore, the PEC is rated for ten times higher than the average power it delivers due to long cycle periods.

The PEC's high power operation would require an inverter of the same power capability (if the inverter's equivalent dc link capacitor is not oversized proportionally with the stretching period), in the case of one standalone DEAP generator. Additionally, in the same case, the inverter and all further power transmission stages would have to work with the bidirectional power transfer together with the PEC (again, if there is no large energy storage to prevent this), see Figure 2.12. However, the DEAP WEC contains many DEAP generators, while the mechanical structure and sea wave propagation provide each PEC operation to be shifted in time in regards to the other PEC's connected to the same DEAP WEC. This, so called, spatial operation of PECs allows the inverter to experience a higher frequency than that of the sea wave. Moreover, the power can circulate between different PECs as they are connected in parallel, which also increases the equivalent capacitance of the dc bus. Furthermore, the connection of number of DEAP WECs (in the same energy farm) to the same dc link would further decrease the effect of the high power peaks seen by the inverter and allow for power to directly circulate between DEAP WECs as well. This spatial operation principle can be related to the interleaving of modules in multimodular converters.

Figure 2.13 presents an example of a PEC spatial operation within a single DEAP WEC device. Power is withdrawn from the dc-bus to charge the DEAP material when the DEAP WEC segment is stretched because of the inner bulge created by the wave propagation (high capacitance state). When the DEAP is contracting (low capacitance, high energy state), power is transferred to the dc-bus, since the DEAP is being discharged. Therefore, that power can be immediately used by another PEC in the charging process, and the rest is sent to the grid through the dc-ac converter. Note that the given example in Figure 2.13 shows the overall negative power transfer at a specific time; hence, the dc-bus is being charged but with significantly lower power compared with the peaks that appear at the instant.
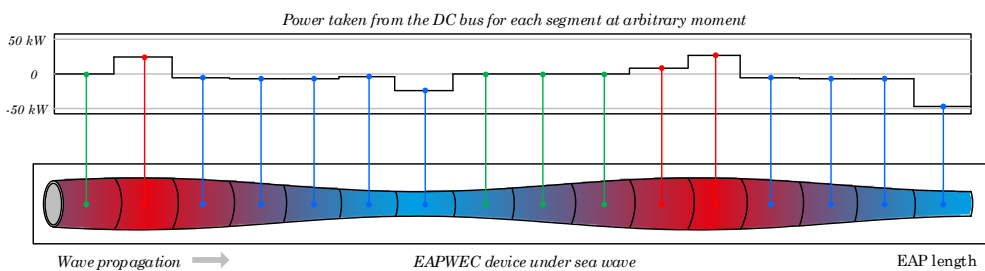
Figure 2.13: Spatial operation of the PECs and the instantaneous power circulation between each PEC and the dc-bus at an arbitrary moment. Explanation of points: green – no power is transferred, red – power is withdrawn from the dc-bus, and blue – power is delivered to the dc-bus

The efficiency of the PEC is very important, since the concept of energy generation implies that a large amount of reactive power must be displaced. For example, with an efficiency below 80%, power cannot be produced, and each additional percentage of efficiency gained above 80% will make a considerable difference. The target efficiency of the PEC is larger

than 95%. In Figure 2.14, it is shown how the efficiency of the PEC affects the average power that is produced per one cycle. In the case of a 4.5 s cycle period and 0.7 capacitance ratio, one percent of PEC efficiency adds about 280 W of produced power per cycle; in the case of 95% efficiency, this is 6.5% more produced power than the case of 94% efficiency. Note that for the calculation of the average power output a constant efficiency is used over the entire voltage-current range. In real application, employing a real converter, the converter's efficiency is not flat (constant) over the operational power range. However, this is demonstrated in the following chapters, and here, only a constant efficiency value is used to simplify the calculation.
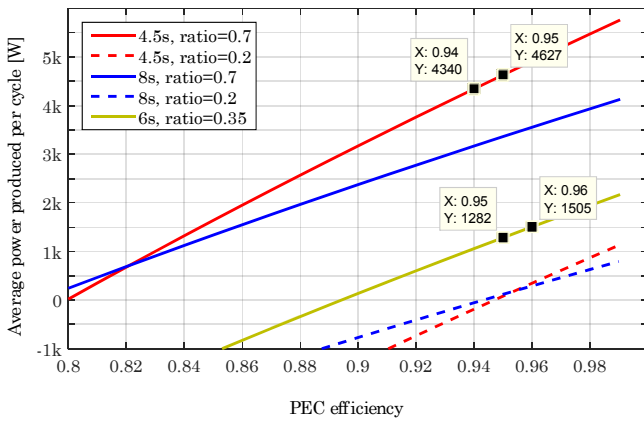
Figure 2.14: DEAP generator average produced power (for one cycle) dependency on PEC efficiency; the parameters are different cycle periods and capacitance ratios, based on a constant PEC efficiency and fixed DEAP length of 250 m

Based on a previously taken length of the DEAP film of 250 m, a minimum voltage over the DEAP appears just before the start of a new charging process. Based on [29], a higher energy gain is achieved when a residual charge is left on the DEAP film after the discharging process. For a cycle period of 8 s and $(C_{max} - C_{min})/C_{av}$ of 0.2, the optimal residual charge is 2.8 C; the corresponding voltage is 950 V, and that is the minimum voltage that can appear in the chosen range of the DEAP generator (sea) states. Consequently, the PEC should have a high efficiency over the DEAP generator voltage range of $0.95 - 10$ kV, however, the taken range is $1 - 10$ kV, as the rounded value. Moreover, operation voltages below 1 kV are also investigated, since residual charge may not always be applied during harvesting cycles.

Inside the chosen area of the DEAP generator (sea) states from the SBM Offshore data, the optimum calculated current is always higher than 5 A for film lengths greater than 20 m. The PEC can provide a maximum of 5 A; therefore, optimization will calculate the optimum

residual charge, while the current is held at 5 A, except for the constant electric field period where the current is very low (< 1 A).

An important characteristic of the PEC, but less important than efficiency, is the output current ripple (current that flows to the DEAP generator). The reason for this is that the DEAP generator has a high series resistance. It is given that the value of this series resistance is 1 Ω. It produces a loss, and additional to that, it can change the DEAP film characteristics because of increased temperature stresses. However, the exact influence of the DEAP generator series resistance loss on the DEAP characteristics is not known at the moment. It is assumed that the influence of the series resistance on total losses must be below 1% of the total power inside the chosen area of the DEAP generator states. For V_{DE} of 1 kV and below, the percentage of DEAP generator series resistance loss is always higher than 1% of the total power. The case when the DEAP generator voltage is lower than 1.5 kV is very rare, so it can be neglected. The taken maximum allowed ratio between rms and the maximum DEAP generator current is 1.2, based on results shown in Figure 2.15.
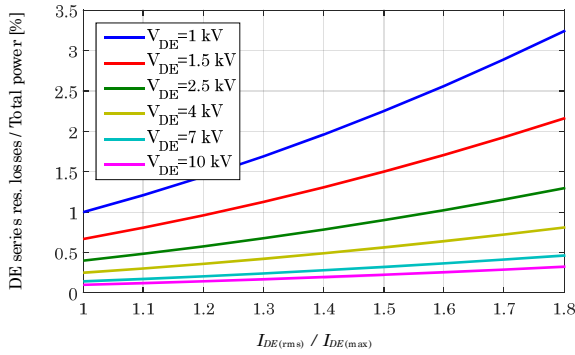
Figure 2.15: Power loss based on the DEAP gen. series resistance (1 Ω) vs. rms-to-maximum current ratio, I_{DE}=5 A

Table 2.3: Summarized PEC specifications

Parameter	Value
Power rating	50 kW
Input voltage, V_{BUS}	800 V dc
Maximum input voltage deviation	5%
Maximum input current	62.5 A
Output voltage range (over DEAP), V_{DE}	0 – 10 kV
Maximum output current, $I_{DE(max)}$	± 5 A
Desired efficiency	> 95%
Maximum ratio $I_{DE(rms)}/I_{DE(max)}$	1.2
Minimum power density	1 kW/dm³

2.5 CONCLUSIONS

Three basic methods for energy harvesting from the DEAP are analysed and compared through energy yield. These methods are: constant charge, constant voltage and constant electric field. The constant electric field provides the highest energy yield among the three basic methods of energy harvesting from DEs. Therefore, the constant electric field method is further used as a reference for the definition of harvesting cycles and interaction with the PEC.

The efficiency of the PEC plays an important role in the energy harvesting from the DEAP generator, as shown in this chapter. For the estimated sea wave conditions, the efficiency of the PEC should be above 95% to produce power at all assumed sea states. The dimensions of the DEAP WEC are determined and further used in calculations and the estimation of the produced energy, as well as for the PEC design. The PEC specifications are obtained from the electrical power take-off system requirements following the initial DEAP WEC system conditions. The spatial operation built-in characteristic of the DEAP WEC can lead to the usage of a low-power-rated inverter, while large power circulates between separated segments and other DEAP WECs in the energy harvesting park.

The main focus of the following investigations is the estimation of the PEC's efficiency and methods to achieve high PEC efficiency values during harvesting cycles. Therefore, PEC interaction with the DEAP generator is necessary for proper loss estimation.

Chapter 3

Bidirectional large voltage variation dc-dc PEC topology study

3.1 INTRODUCTION

From the typical waveforms in Figure 3.1, it can be seen that the power electronic converter has to provide a large range of voltages (0 – 10 kV) over the DEAP generator, while the current is kept constant and at a maximum. Additionally, low DEAP generator current values should be covered during the constant electric field period of the harvesting cycle. Therefore, voltage and current values that have to be delivered to the DEAP generator create a large power surface that defines the power converter operation area, see Figure 3.1.

The power converter operating area in combination with the required high efficiency (> 95%) is the most important parameter for the topology study, design and control of the power electronic converter. Some electronic power converters interfacing the DEAP generator are discussed in [31-37], however, the power levels (up to 1,000 W peak power) are significantly lower than what is analysed in this thesis.

This chapter provides an overview and comparison of the suitable power converter topologies for the DEAP WEC application. Topologies are compared through a special comparison framework that includes different criteria, initial loss estimation and design of each investigated power converter topology. Finally, the results of the comparison are presented in the form of total rating for each topology.
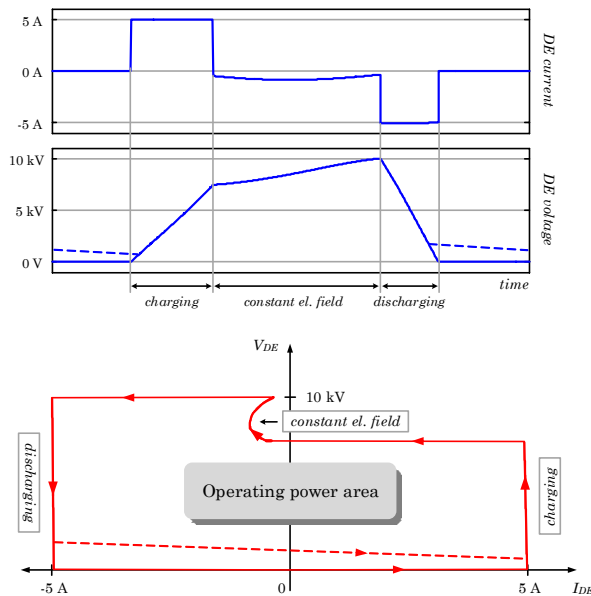
Figure 3.1: Typical DEAP generator current and voltage waveforms during one harvesting cycle (top), the matching curve and required power converter operating area (bottom); constant el. field with non-residual charge (solid line) and residual charge (dash line) harvesting approach

The main issues addressed in this chapter are:

- Power converter topology overview for the DEAP WEC application;
- Initial loss modelling and loss estimation for the investigated topologies;
- Initial converter design;
- Comparison framework definition and comparison results.

3.2 CANDIDATE MEDIUM-VOLTAGE DC-DC TOPOLOGIES

The power electronic converter is a part of the complete power take-off system, which harvests energy from the DEAP generator. On the one side, it is directly connected to the terminals of the DEAP generator, and on the other side, it is connected to the rest of the PTO system (see Figure 2.12). The given converter power rating is 50 kW, with a maximum voltage of 10 kV (maximum voltage that can appear over the DEAP generator) and a maximum charging/discharging average current of 5 A at the DEAP generator side. The input voltage (V_{BUS}) is fixed at 800 V dc and is balanced by the inverter that is connected to the grid on the other side.

The power electronic converter must provide bidirectional power flow to charge and discharge the DEAP generator. In the following text, all proposed candidate converter topologies are described.

3.2.1 Two-quadrant converter

A two-quadrant converter (2QC), or half-bridge, is a basic topology used for this application [29], see Figure 3.2. It requires a complex stacking of switches to block the full DEAP generator voltage of 10 kV; when commonly used, up to 6.5 kV, switches are employed. Nevertheless, it is modelled because it represents a basic charging/discharging concept for the DEAP energy harvesting. However, the problem of series switches stacking is not included in the modelling but is considered as the topology's drawback. The 2QC serves mostly as a benchmark for other topologies in further investigation.

The working principle of the 2QC is well known and can be seen as a voltage step-up or step-down operation. The step-up operation mode provides the energy (charge) to the DEAP generator, while the step-down mode discharges the DEAP generator, see Figure 3.3. The inductor L is a magnetic energy storage and serves as a current filter during the step-down operation, while it helps boosting the voltage during step-up mode. In all mentioned modes, the inductor L accumulates and releases the energy E_L from its magnetic field. Therefore, the inductor L can be seen as a decoupling component between low and high voltages. In the steady-state operation of the converter, the inductor's energy build-up and release are equal; thus, the energy change in the inductor's magnetic field is zero, when one switching time period is observed (or a whole number of switching periods).
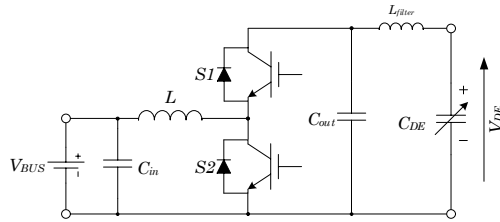
Figure 3.2: Two-quadrant converter connected to the DEAP generator

(a) voltage step-up mode

(b) voltage step-down mode
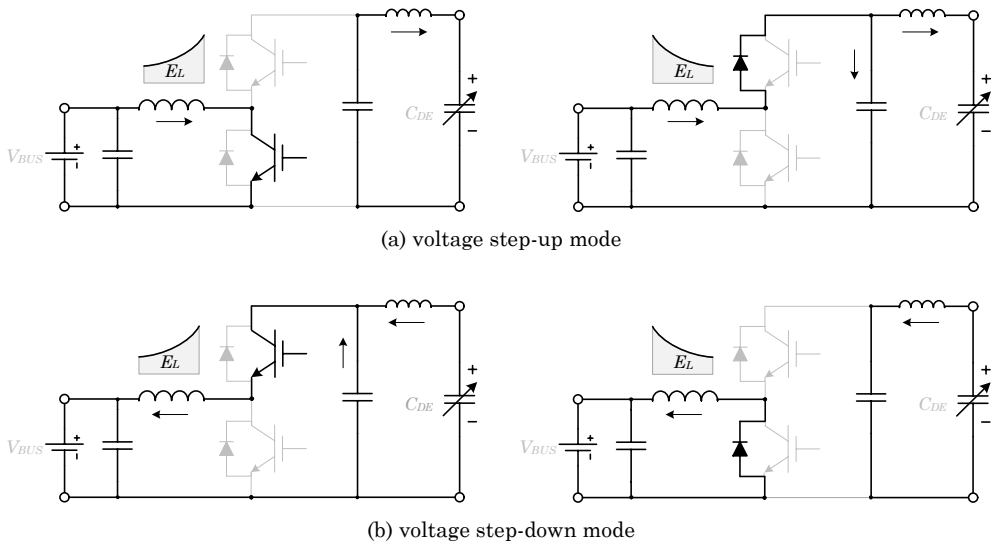
Figure 3.3: Operation mode of the 2QC: step-up mode for the DEAP generator charging (a) and step-down mode for the DEAP generator discharging

Every switch stack, upper or lower, in the 2QC has to block the maximal voltage that appears in the circuit, which is 10 kV. The current rating of the switches mainly depends on the maximal current that circulates in the 2QC, and as the ratio of V_{BUS} and V_{DE} rises, for the constant pulse current at the DEAP generator side, the circulating current increases as well. This leads to the high power rating of the converter, even if it operates at the maximum power point for a very short time during every cycle. This may affect efficiency at the high step-up or step-down ratio, exactly where most of the power is transferred.

In Table 3.1 are given 2QC design parameters for several switching frequencies. The design procedure and method are given in the Appendix. Later, these parameters are used for comparison purposes.

Table 3.1: 2QC design parameters

	Parameter	Value at switching frequency					
	Switching frequency [kHz]	5	8	10	12	15	20
Inductor, input	Inductance [µH]	3680	2300	1840	1530	1230	920
	Current peak / ripple [A]	82.5 / 40	82.5 / 40	82.5 / 40	82.5 / 40	82.5 / 40	82.5 / 40
	Winding resistance [mΩ]	144	123	112	116	97	100
	Number of turns	53	68	74	86	86	102
	Air gap [mm]	27.3	35	38	44	44	53
	Core volume [mm³], 202000 ·2·	39	19	14	10	8	5
	Core effective area [mm²], 738·	39	19	14	10	8	5
Inductor, filter	Inductance [µH]	4000	2500	2000	1700	1300	1000
	Current peak / ripple [A]	5.5 / 1	5.5 / 1	5.5 / 1	5.5 / 1	5.5 / 1	5.5 / 1
	Winding resistance [mΩ]	196	100	95	65	73	41
	Number of turns	63	49	53	44	53	39
	Air gap [mm]	1.5	1.2	1.2	1	1.2	0.9
	Core volume [mm³], 22700 ·2·	5	4	3	3	2	2
	Core effective area [mm²], 233·	5	4	3	3	2	2
Cap.	Capacitance, input [µF]	25	16	12.5	10.5	8.3	6.3
	Capacitance, output [µF], 169·	23	14	12	9.5	7.7	5.8
	Number of switches (chips)	78	78	78	78	78	78

3.2.1.1 Multiphase converter

A multiphase two-quadrant converter (MPC) is considered as a possible solution for the power electronic unit, see Figure 3.4. It consists of a number of half-bridge (2QC) cells connected in parallel for both input and output. By shifting the phases of the cells in time, filter components may be reduced as the outputs and inputs of each cell are interleaved [38-41]. Moreover, half-bridge cells are splitting the large input current, thus, paralleling of the switches in the stack is not required. Additionally, because of the topology configuration, a modularity is achieved.

Each half-bridge cell of the converter works as one phase and is shifted in time in relation to the other cell phases. Since the blocking voltage of each switch is rated to the maximum voltage in the system (V_{DE}), these switches must be stacks of several lower voltage switches. This leads to a high number of switch components and several high voltage inductors (depending on the number of phases). Since interleaving may reduce filter components, the filter capacitors should be mostly reduced. Large input inductors could allow for a higher current ripple, in expense of additional input capacitance, but this could lead to a poorer converter efficiency, as the cell may operate in discontinuous conduction mode (DCM). Therefore, the optimization of choosing the right filter components has to be done to achieve the best results using this topology. However, the MPC is not investigated through analysis here, but its parameters can be estimated based mostly on the 2QC results.
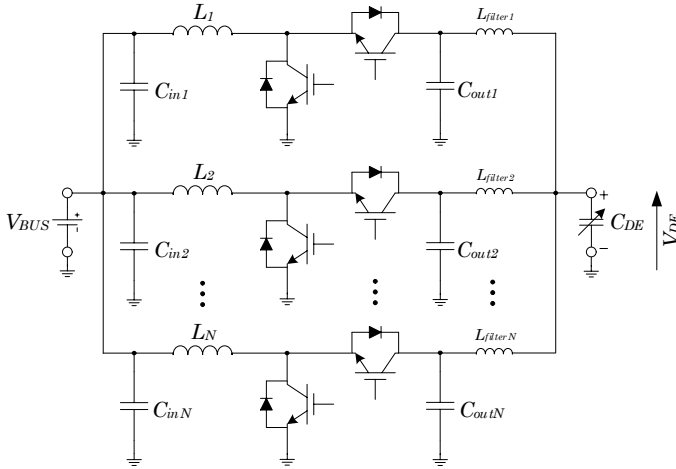
Figure 3.4: Multiphase converter connected to the DEAP generator

3.2.2   Flying-capacitor multilevel converter

The flying-capacitor (or capacitor-clamped) multilevel converter (FCMC) is presented in Figure 3.5 as a solution for using low voltage switches. The FCMC is one of the basic multilevel topologies [42-44], and it mostly provides smaller filter components and a voltage clamping mechanism for the balancing of the voltages over each low voltage switch. Multilevel converters are the only way, except series stacks, to overcome the problem of high voltages, in the sense that they increase the voltage capability of the system regardless of the switch limitations. However, the special modulation technique has been employed to provide normal operation of the converter.

This is a perfect place to provide an explanation and definition of the multilevel term associated with the power electronic converters. The multilevel term is usually used together with four basic multilevel converters: diode-clamped, flying-capacitor, cascaded and modular-multilevel converters. All four are able to provide multiple voltage levels at the low voltage or the ac voltage side (depending on the configuration, dc-dc or dc-ac), while each switch blocks only $(N-1)^{th}$ part of the high voltage dc link. The N is the number of levels associated with the multilevel converter, and it tells how many voltage levels are available to provide at the converter output, including zero voltage. Each voltage level is defined with $mV_{DC}/(N-1)$, where m is an integer number that is $0 \leq m \leq N-1$ for dc-dc and $-(N-1)/2 \leq m \leq (N-1)/2$ for dc-ac converters. Nowadays, the common thing in the literature is the direct association between the multilevel term and multiple voltage level capability of the converter. However, this is not the original philosophy behind multilevel converters. The multilevel term comes from the ability of the converter to provide the $(N-1)^{th}$ part of the high dc voltage over each single switch, regardless of the voltage ripples. Hence, the switch technology and material limitations related to the voltage rating are overcome.
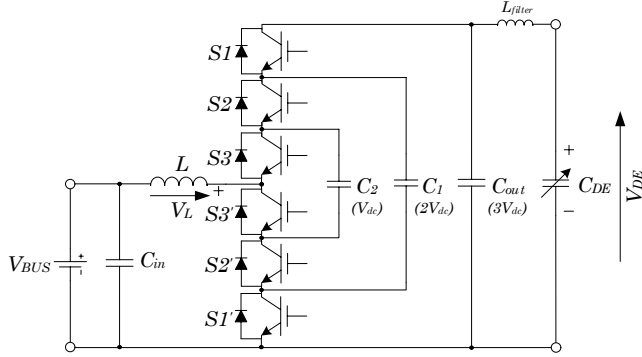
Figure 3.5: Four-level flying-capacitor multilevel converter connected to the DEAP generator

The FCMC uses the input inductor L in the same manner as the 2QC. Additionally, the FCMC uses voltages over flying capacitors to reach a high voltage at the DEAP generator side. In this thesis, the FCMC topology is modelled with its capability to give different voltage levels and voltage balancing in the steady state. The modulation technique that provides the voltage balancing involves time-shifted modulation carriers for each complementary switch pair. This leads to a smaller inductor on the input side, as the effective frequency "seen" by the inductor is (N-1) times higher than the modulation carrier frequency. However, the actual voltage must be regulated at every capacitor stage, because those voltages are responsible for voltages over of the switches. On the other hand, the advantage of this topology compared with the diode-clamped, for example, is that FCMC has more redundant switching states. This provides more possibilities when choosing the proper switching state during the balancing process.

As a modulation method for FCMC, a phase-shifted sinusoidal PWM (PS-SPWM) technique was proposed in [45-50] for the application of paralleling identical inverters to form a large uninterruptible power supply system. For a four-level flying capacitor converter, the sinusoidal modulation signal is compared with three triangular carrier signals that are phase-shifted by 90°. The resulting PWM signals control the corresponding switches. This control method is given for the constant high voltage side. In this application, the high voltage side is variable, so control must be further investigated to keep capacitor voltages balanced. In the following text, the modulation of the FCMC is presented using a four-level converter and constant DEAP generator voltages.

For a given four-level topology in Figure 3.5, all modes of each flying capacitor during the process of DEAP generator discharging are presented in Table 3.2. The voltage V_{out} refers to the voltage before the inductor L, that is the voltage across the converter's lower arm (set of switches).

Table 3.2: Four-level flying-capacitor converter voltage levels and their switching states for the DEAP generator discharging process

$V_{out}=V_{BUS}+V_L$	Switching states			Capacitors charge(+) / discharge(−)		
	S1	S2	S3	C_1	C_2	C_{out}, C_{DE}
V_{DE}	1	1	1			−
2/3 V_{DE}	1	1	0		+	−
	1	0	1	+	−	−
	0	1	1	−		
1/3 V_{DE}	1	0	0	+		−
	0	1	0	−	+	
	0	0	1	−		
0	0	0	0			

Figure 3.6 illustrates the phase-shifted PWM method applied to a four-level FCMC. It can be seen that the phase-shifted PWM produces the symmetrical switching control signals that can maintain the capacitor voltage to a certain degree by applying the same time for the charging and discharging switching states. Therefore, this method with the self-balancing property was suggested and widely used for FCMCs [51, 52].

However, despite the symmetrical control scheme, the voltage unbalance of the flying capacitor in practical implementation is present. This is mainly due to the unequal parameters of the converter caused by different switch device tolerances, different dv/dt and different values of the capacitors. Therefore a feedback loop is required to eliminate the accumulative error and make capacitor voltages stabilize at the desired reference value [53].
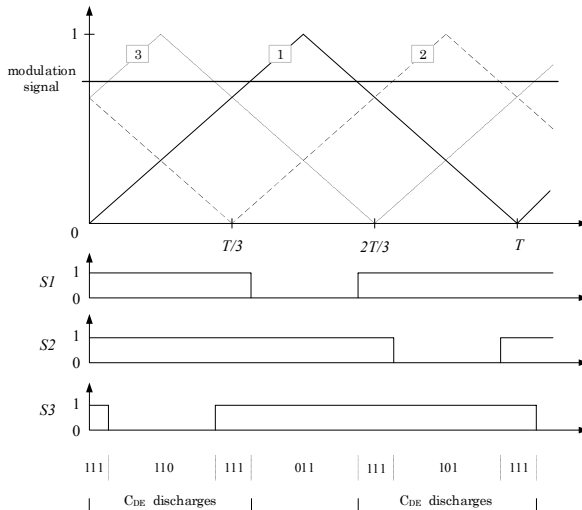
Figure 3.6: Generation of switch gate signals for a four-level FCMC based on the phase-shifted PWM method

During the start-up of the converter, precaution has to be taken that the power switches are not exposed to over-voltage because of unequally charged or uncharged capacitors [46]. At the beginning of the DEAP generator charging process, after it was discharged in previous cycle, voltages over the capacitors may be very low. This causes an increase in inductor current during charging when there is no start-up procedure before each harvesting cycle.

For the overall rating of the topology, the balancing of the capacitor voltages is addressed as a problem, as well as pre-charging, the inability to leave the optimal amount of charge on the DEAP generator and a high number of capacitors. However, some methods were proposed for the balancing of the capacitor voltages, as in [46, 53].

In Table 3.3 are given FCMC design parameters for a range of switching frequencies. The design procedure and method are given in the Appendix. Later, these parameters are used for comparison purposes.

Table 3.3: FCMC design parameters

	Parameter	Value at switching frequency					
	Switching frequency [kHz]	5	8	10	12	15	20
Inductor, input	Inductance [µH]	300	200	150	130	100	75
	Current peak / ripple [A]	63.5 / 2	63.5 / 2	63.5 / 2	63.5 / 2	63.5 / 2	63.5 / 2
	Winding resistance [mΩ]	54	62	35	26	45	25
	Number of turns	44	59	44	38	59	44
	Air gap [mm]	17.5	23.2	17.5	15.1	23.3	17.5
	Core volume [mm³], 79000 · 2 ·	4	2	2	2	1	1
	Core effective area [mm²], 540 ·	4	2	2	2	1	1
Inductor, filter	Inductance [µH]	4000	2500	2000	1700	1300	1000
	Current peak / ripple [A]	5.5 / 1	5.5 / 1	5.5 / 1	5.5 / 1	5.5 / 1	5.5 / 1
	Winding resistance [mΩ]	196	100	95	65	73	41
	Number of turns	63	49	53	44	53	39
	Air gap [mm]	1.5	1.2	1.2	1	1.2	0.9
	Core volume [mm³], 22700 · 2 ·	5	4	3	3	2	2
	Core effective area [mm²], 233 ·	5	4	3	3	2	2
Cap.	Capacitance, input [µF]	0.072	0.045	0.036	0.030	0.024	0.018
	Capacitance, output [µF], 169 ·	23	14	12	9.5	7.7	5.8
	Capacitance, clamping [µF], 650 ·	9.2	5.7	4.6	3.8	3.1	2.3
	Number of switches (chips)	78	78	78	78	78	78

3.2.3 Diode-clamped multilevel converter

One of the basic multilevel topologies is the diode-clamped multilevel converter (DCMC) [44]. The diode-clamped multilevel boost/buck converter is shown in Figure 3.7 and is used

for the charging and discharging of the DEAP generator. It is seen that a bidirectional converter, in one direction, from V_{BUS} as a source, works as a boost (step-up) by using the same principle of inductor energy accumulation/release, as in the 2QC and FCMC, until the required voltage over C_{DE} is achieved. To maintain a constant level of charging current to the DEAP generator, a constant rise of voltage at the converter output is needed, since the DEAP generator behaves as a capacitive load. Another direction of power transfer, the discharging DEAP mode, can be explained in the same manner as with the FCMC.

The first noticeable drawback of this topology is the presence of many diodes. The number of diodes has a quadratic dependence on the number of levels. This directly affects efficiency and cost and has a bad outcome because of the diode body on-resistance during the conduction state. However, it is possible to reduce the number of clamping diodes, as in [54].

The present problem is with the voltage balancing of the output capacitors (C_1, C_2, C_3) when using multiple level voltage generation. These capacitors split the high voltage dc-link, at the DEAP generator side, and provide the blocking voltage of switches through the clamping diodes. Because of the DCMC configuration, during the discharging process of the DEAP, the lowest positioned capacitor (C_1) in the dc-link is charged (as well as the higher positioned capacitors) only when all switches (higher set) are open, and in any other case, the capacitor C_1 is discharged. Thus, higher positioned capacitors C_2 and/or C_3 may be charged during this process (depending on the output voltage level, some other lower positioned capacitors can be discharged as well, i.e., C_2) above the allowed voltage level. This results in the imbalance of the dc-link capacitor voltages, and the high blocking voltage may appear over the switches causing instantaneous switch destruction. If this operation continues without switch destruction (meaning that V_{DE} is lower than the single switch rated blocking voltage), the upper capacitors C_2 and C_3 will keep charging, and capacitor C_1 will be discharged to zero [45] after some time.
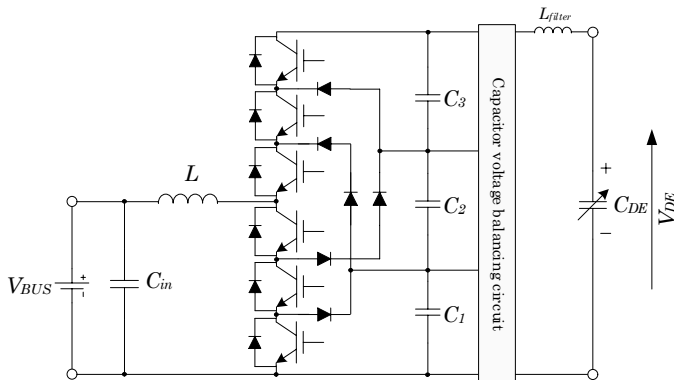
Figure 3.7: Four-level diode-clamped multilevel converter connected to the DEAP generator. A voltage balancing circuit is included for balancing the capacitor voltages

In contrast from above, during the DEAP generator's charging mode, the lower positioned capacitor C_1 is charged, while C_2 and C_3 are discharged, and over time the entire DEAP generator voltage appears over the lowest positioned capacitor, C_1. Then, it seems like there is no problem in this operation, as the lower positioned capacitors are predominantly charged while the DEAP generator is being charged and predominantly discharged during the DEAP generator discharging process (the opposite is valid for higher positioned capacitors). The only condition is the proper sizing of the dc-link capacitors to provide enough energy storage so that the capacitor voltage does not vary above the switch voltage blocking capability. And that is exactly the problem, since the DEAP energy harvesting cycle has a frequency of approximately 0.15 Hz, which requires enormous storage capacitances.

The one reasonable solution is an additional electrical circuit that would balance each individual capacitor voltage in the high voltage dc-link. For that purpose, another DCMC can be employed sharing the same dc-link capacitor bank, see Figure 3.8. However, this solution is not discussed nor deeply investigated (modelled) due to anticipated high losses caused by the high number of switches carrying the large circulating current.

Another circuit that also comprises an additional DCMC is depicted in Figure 3.9 [55]. It cannot individually balance the voltages over dc-link capacitors if it operates in dc-dc mode, but the idea of operation principle relies on the above-mentioned mechanism of overcharging the lower or upper positioned capacitors in a single DCMC. During one operation mode, e.g., DEAP generator charging, the first DCMC would try to overcharge the lower positioned capacitors, while the second DCMC would try to undercharge the same
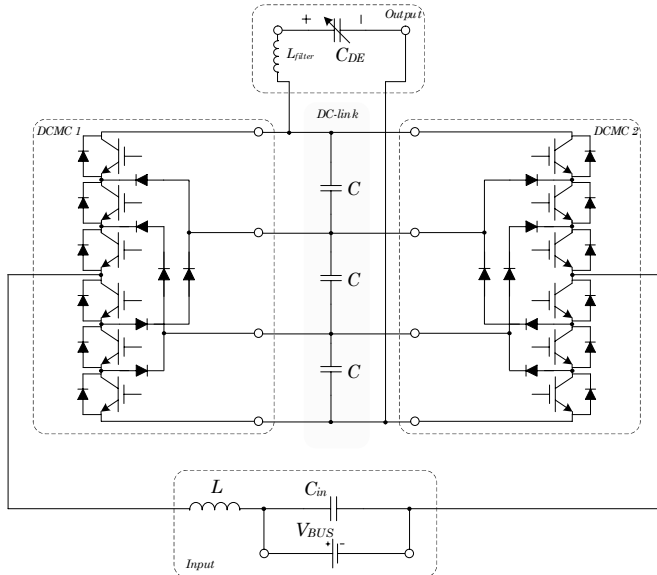
Figure 3.8: Two DCMC circuits employed for the voltage balancing of individual dc-link capacitors
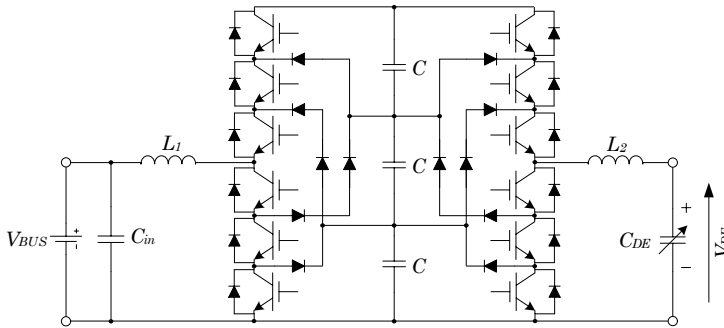
Figure 3.9: Two DCMCs used for voltage balancing of the entire dc-link voltage

capacitors. However, the whole circuit fails to keep the dc-link capacitor voltages balanced as the DEAP generator voltage rises. This follows from the fact that the DCMC cannot step-up the voltage over the whole dc-link to a high level without sacrificing the voltage clamping mechanism, i.e., it cannot operate at voltages above the switch blocking capability.

3.2.4 Cascaded multilevel converter

The cascaded multilevel converter (CMC) is another basic multilevel topology (see Figure 3.10), thus, it also allows for the usage of low voltage switches. The CMC has a modular configuration as it consists only out of interconnected modules [44]. The cascaded converter is sometimes called a chain converter because switch bridges are connected in a cascade like the links of a chain to build up the voltage. The chain-link or sub-module is usually a full-bridge (H-bridge) circuit, however, for this application the negative voltage is not required; thus, the half-bridge (HB) is employed as one of CMC's sub-modules. Furthermore, each HB sub-module, using PWM, modulates the voltage of its dc-link and basically operates as a 2QC. However, for the DEAP generator charging process the HB sub-module operates in a step-down mode, and vice versa, hence, the inductor is needed.
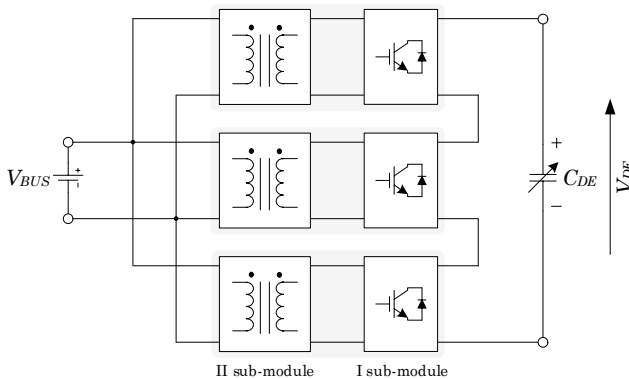
Figure 3.10: Cascaded multilevel (chain) converter connected to the DEAP generator

Since there are no switches that can block the potential difference between the dc-bus and the DEAP generator, additional voltage isolation must be provided. The voltage isolation barrier is achieved using a transformer that operates at high frequency (kilohertz range), thus, the transformer volume and overall converter size are minimized. Furthermore, to optimally use the transformer capability, ac voltages are applied over its windings. To provide those voltages, in most cases, a single H-bridge is utilized for each of the transformer windings, thus, the dual active bridge (DAB) circuit is obtained, see Figure 3.11.

The commonly used modulation approach for the DAB is the phase-shifting modulation [56, 57]. The same modulation is employed here for investigation purposes at the initial stage. The DAB's purpose, besides providing the voltage isolation, is to maintain the voltage over the intermediate capacitor (C_{out}) positioned between the DAB sub-module and the associate HB sub-module circuit. The HB sub-module and the DAB sub-module are the main parts of one single CMC module.

The main transformer limitation is the leakage inductance, required for the suitable power transfer at the specified frequency, which is affected by the high voltage isolation requirement. Since this topology can use both zero voltage switching (ZVS) and zero current switching (ZCS), the expected efficiency is high. However, the number of switches is very high, which may result in a low converter reliability. On the other hand, the modular CMC structure provides high operation robustness, as the converter can function even if the whole module fails. Furthermore, the modular structure with modules connected in parallel at the input side (low voltage) spreads the high input current into individual modules, thus, eliminating the need for switch paralleling.

The CMC topology can make use of space-shifting between modules or chain-links to minimize inductor L size, as an effective frequency would be N times higher. Furthermore, the CMC allows full control of charges at the DEAP generator, while the DAB has many known modulation methods that can be used to increase the overall efficiency [56-68].

In Table 3.4 are given the CMC design parameters for several switching frequencies. The design procedure and method are given in the Appendix. Later, these parameters are used for comparison purposes.
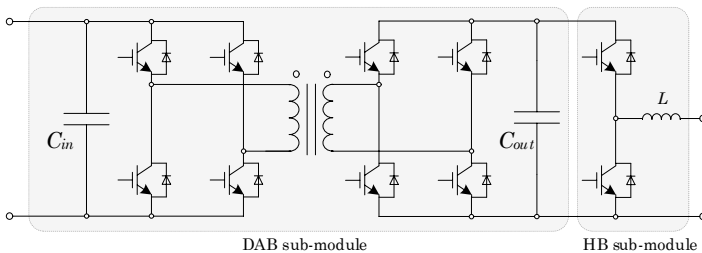
Figure 3.11: Single CMC module consisting of a dual active bridge and a half-bridge circuit

Table 3.4: CMC design parameters of a single module, 13 modules needed

	Parameter	Value at switching frequency					
	Switching frequency [kHz]	10	15	20	25	30	40
Inductor, output	Inductance [µH]	120	80	60	47	40	30
	Current peak / ripple [A]	5.5 / 1	5.5 / 1	5.5 / 1	5.5 / 1	5.5 / 1	5.5 / 1
	Winding resistance [mΩ]	83	98	103	66	147	83
	Number of turns	34	46	52	42	70	52
	Air gap [mm]	3	4	4.5	3.6	6	4.5
	Core volume [mm³], $1930 \cdot 2 \cdot$	6	3	2	2	1	1
	Core effective area [mm²], $39 \cdot$	6	3	2	2	1	1
Transformer	Leakage inductance [µH]	1280	850	640	510	430	320
	Winding resistance [mΩ]	33	28	27	26	34	19
	Number of turns per winding	27	30	34	36	45	33
	Core volume [mm³], $202000 \cdot 2 \cdot$	10	6	4	3	2	2
	Core effective area [mm²], $738 \cdot$	10	6	4	3	2	2
Cap.	Capacitance, input [µF]	0.5	0.33	0.25	0.2	0.17	0.13
	Capacitance, output [µF]	0.5	0.33	0.25	0.2	0.17	0.13
	Number of switches (chips)	10	10	10	10	10	10

3.2.5 Modular multilevel dc-dc converter

Even though the M2C [69-75] is used as a dc-ac (or an ac-dc) converter, its technique of balancing voltages over sub-module capacitors employing circulating power (either with fundamental or higher harmonics) can be applied on the dc-dc conversion as well [76-78].

The drawback of the M2C topology is the required capacitance of the sub-modules, for a given voltage ripple, that is inversely proportional to the output frequency of the inverter. This problem can be addressed by superimposing a common mode voltage on the output ac voltage. This second ac voltage, which has to be at a different frequency, is inherent to the mechanism whereby energy is exchanged between the capacitors of the top and bottom power cells by generating a second ac voltage at a different frequency [76].

A new topology, of M2C family, can be employed for the DEAP WEC application. The proposed M2DC converter from [76, 77] uses the mentioned energy mechanism and can be used in dc-dc applications. The independence of the active power at different frequencies makes possible a converter without a power source that can generate active power at one frequency and absorb the same amount of power at different frequencies.

This leads to the push-pull circuit where an ac current is circulated between two parallel strings of sub-modules, as shown in Figure 3.12. The sub-module is the same as in M2C, that is, a two-quadrant converter. However, a four-quadrant converter, or H-bridge, can be also employed as the sub-module, and therefore, provide a higher voltage swing if necessary.
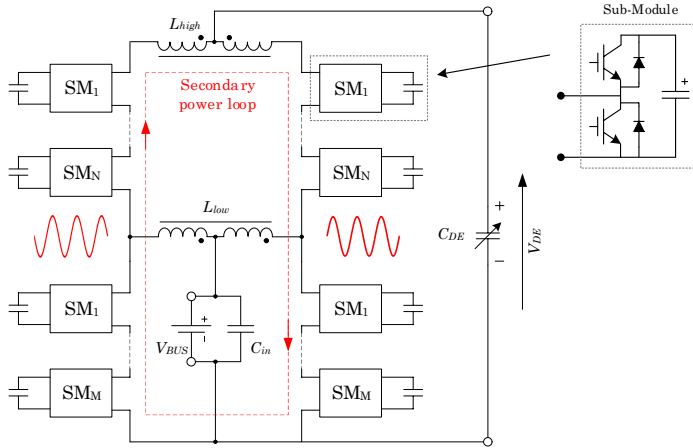
Figure 3.12: Push-pull modular multilevel dc-dc (M2DC) converter [77]

A centre tap inductor (L_{low}) is included that has a conveniently large reactance at the secondary loop frequency. The dc source is connected at the centre tap, and therefore, the dc current polarities oppose each other. A coupled inductor (L_{high}) is used at the input, but the winding polarities are the opposite. The mutual inductance of L_{high} serves as an input filter function, while the leakage inductance smooths out the ripple of the circulating current.

From [77] follows that, for the same wave energy application, the M2DC topology in comparison with the DAB based solution, has a simpler voltage isolation design, and fewer switch gate drivers and magnetic components, as well as a simpler magnetic components design. Most of the advantages follow from the fact that module capacitor voltages are balanced without additional circuits. However, the number of necessary switch chips is higher due to higher circulating currents. Since the M2DC does not benefit from ZVS and employs a large number of switch chips that have to deal with the large circulating currents, the M2DC is omitted from further investigation. At this moment, the M2DC concept is proven through simulation, while experimental test results are currently in progress.

3.2.6 Summary of candidate topologies

In the previous sections the candidate dc-dc medium voltage topologies are presented, and their operation briefly explained. Most importantly, the overview of the disadvantages is given with respect to DEAP WEC application requirements.

The first presented topology is a two-quadrant converter, i.e., half-bridge circuit, which is the simplest converter that can be employed for the given application. It's simple from the topology configuration perspective and controllability but requires a complex stacking of switches in series to provide a blocking voltage of up to 10 kV. Furthermore, the employed inductor has to be large as it experiences very high voltages because of high voltage ratios

between the input and output. Moreover, because of the same high voltage ratios, the circulating current that flows through the input inductor increases the current rating of the switches, as well as the size of the filter components. Nevertheless, the 2QC is modelled to provide the initial loss data and for comparison purposes. The multiphase converter is basically a converter with a multiple number of 2QCs, operating in a space-shifted manner, thus, minimizing filter components. However, the same problem of switch stacking is present as in the 2QC.

The flying-capacitor multilevel topology is known as the circuit that can deal with high voltage ratios between the input and output, while employing low voltage switches to block only part of the converter full voltage rating. As it is capable of providing low voltage steps over the inductor, the input inductor size can be reduced compared with the 2QC, which is also due to the space-shifting operation that creates the effect of a higher frequency seen by the inductor. However, the same circulating current is present as in 2QC. Moreover, it comprises a large number of capacitors that have to carry a circulating current, which could affect the converter reliability and lifetime.

The diode-clamped topology is investigated as it represents a basic multilevel diode clamping mechanism. However, it fails to operate standalone, and it is necessary to employ an additional circuit for the balancing of high voltage dc-link capacitors responsible for blocking the voltages of the switches. A possible solution is presented, comprised of two DCMC connected to the same high voltage dc-link, but it includes more switch components carrying the circulating current, thus, affecting efficiency. The DCMC is not investigated further due to its drawbacks found within operation in the DEAP WEC system.

The cascaded multilevel converter provides the modular structure that allows minimizing the filter inductor, in the same manner as in the FCMC. Moreover, the high level of modularity provides robustness while operating with the CMC. The employed dual active bridge circuit can operate at high frequencies, since the ZVS and ZCS can be achieved easily, thus, minimizing the isolation transformer. Furthermore, in contrary to previous topologies, the CMC can completely discharge the DEAP generator, as it boosts the voltage within the DEAP generator discharging process. On the other hand, to provide all mentioned benefits, the CMC comprises a large number of switch components, which, however, do not carry the large currents presented in, e.g., 2QC.

The modular multilevel dc-dc converter is a novel approach for dc-dc power transmission within high voltage systems for stepping-up or stepping-down the voltage. Its operation principle is briefly given here, and further investigation is not carried out as it provides efficiency results inferior to the DAB-based circuits employed for large voltage ratios.

3.3   LOSS MODELLING METHOD AND LOSS ESTIMATION

Loss modelling is carried out to provide preliminary efficiency results used for the cycle energy loss estimation, as well as to determine the switching frequency that is required for the calculation of the magnetic and electrostatic components. Initially, the loss modelling is performed using Si IGBT switches. If it is necessary to put more than one IGBT in parallel to meet requirements for the current, it is done in such a way that the number of paralleled switches is not higher than what is needed. Thus, the switches are not paralleled to minimize total losses but only to satisfy the current requirement.

To determine all currents and voltages that appear in the analysed circuit, the analytical model is developed and based on a lossless converter operation. Next, the main requirement is the power, i.e., the voltage and current that has to be delivered to the DEAP generator, which determines the modulation parameters of the converter. In the following, the converter output, i.e., the DEAP generator, the current and voltage is used for any loss or efficiency results presentation.

3.3.1   Loss modelling

Modelled power losses of the converter consist of: the conduction losses of switches, switching losses, transformer losses, inductor losses and the power given by auxiliary power supplies for electronics. Loss modelling is done for the steady state of the converter. For the case when the generator voltage is changing fast, the loss modelling is not considered since the DEAP WEC application does not require large voltage slopes. In the case of large DEAP generator voltage slopes, the converter would have to operate in a transition mode, which would further affect efficiency. However, the transition mode would mean that more power is processed within the electronic converter than what is delivered to the DEAP generator. The excess power is actually reactive power provided to the output filter capacitor, hence, the output voltage increases.

3.3.1.1   Switch conduction losses

The switch conduction losses are calculated based on an expression derived from:

$$
\begin{aligned}
P_{sw(\text{con})} &= \frac{1}{T}\int i_C(t)v_{CE}(t)dt \\
&= \frac{1}{T}\int i_C(t)\big(v_{CE0}+r_Ci_C(t)k_{Tc}\big)dt \qquad . \\
&= v_{CE0}\frac{1}{T}\int i_C(t)dt + r_Ck_{Tc}\frac{1}{T}\int i_C^2(t)dt
\end{aligned}
\tag{3.1}
$$

Therefore, the IGBT conduction losses are calculated based on the collector-emitter on-state resistance (r_C), on-state zero-current collector-emitter voltage (v_{CE0}), the average IGBT

current ($I_{C(\mathrm{av})}$), the rms IGBT current ($I_{C(\mathrm{rms})}$) and temperature scaling function for the collector-emitter on-state resistance (k_{Tc}), as in:

$$P_{sw(\mathrm{con})} = I_{C(\mathrm{av})}v_{CE0} + I_{C(\mathrm{rms})}^2 r_C k_{Tc} \,. \tag{3.2}$$

The temperature scaling function defines how certain switch parameters are changing with the junction temperature. The junction temperature is described as a linear function of the power that the converter delivers, with a set maximum estimated value. The same calculation is used for the anti-parallel diode and MOSFET conduction losses. However, the MOSFET conduction losses do not include the on-state zero-current drain-source voltage (v_{CE0}), since MOSFETs are unipolar components. The conduction losses of all switches are contained in $P_{sw(\mathrm{con})(\mathrm{tot})}$.

3.3.1.2   Switching losses

The IGBT turn-off losses are calculated using datasheet values for the applied test blocking voltage (v_{CE}) and current (i_C), as there is no snubber capacitor to assist (hard switching). The equations for turn-off and turn-on energy losses are given respectively:

$$E_{off} = k_{Ts(\mathrm{off})}(T_j)k_v(V_{dc})E_{off(\mathrm{datasheet})}(v_{CE},i_C) - \frac{1}{2}C_{oss}V_{dc}^2 \quad, \tag{3.3}$$

$$E_{on} = k_{Ts(\mathrm{on})}(T_j)k_v(V_{dc})E_{on(\mathrm{datasheet})}(v_{CE},i_C) + \frac{1}{2}C_{oss}V_{dc}^2 \quad, \tag{3.4}$$

where k_v is a voltage linear scaling function, k_{Ts} is a temperature scaling function for switching losses, and C_{oss} is the switch output capacitance. The voltage scaling function is used to scale the datasheet parameters to the applied switch blocking voltage (V_{dc}). The obtained datasheet switching turn-on energy ($E_{on(\mathrm{datasheet})}$) includes the energy of the diode reverse recovery effect.

It is assumed that the datasheet measured energy data during the turn-off transient includes the energy stored in the switch output capacitance. This energy is included in the turn-on loss calculation, and therefore, is subtracted from sampled datasheet values for the turn-off energy. For the turn-off energy calculation, it is taken that the snubber capacitor is not added in parallel to the switch, and therefore, the snubber-assisted decrease of the turn-off losses combined with the ZVS are not considered, if they apply to the circuit operation. Generally, the snubber capacitor would increase the switch output equivalent capacitance and cause turn-off losses to decrease; the snubber would store the energy instead of being dissipated in the switch, as given in (3.3). The larger the equivalent capacitance is, the lower the turn-off energy.

The ZVS turn-on will occur if the energy stored in the inductor L carrying the current is enough to fully discharge the IGBT's equivalent output capacitance before the actual turn-

on takes place, thus, the turn-on losses are neglected. The current required for the ZVS can be calculated as:

$$I_L = \sqrt{\frac{C_{oss}V_{dc}^2}{L}} \, ,$$

(3.5)

assuming that the total switch output capacitance (C_{oss}) is charged to the dc-link voltage (V_{dc}), while I_L is the instantaneous inductor current at which the complementary switch turns-off. The important parameter is the dead-time, i.e., the time period during which both switches in the single leg are turned-off to prevent a dc-link short circuit. The dead-time has to be long enough to allow the actual output capacitance discharge until the anti-parallel diode conducts.

Otherwise, additional losses appear during IGBT turn-on ($E_{on(add)}$), and the ZVS is lost. These additional losses are calculated using residual energy stored in the equivalent output capacitance of the switch. The effect of ZCS on the losses is not described here, since it does not appear in the modelled operation of investigated converters, at this moment. It is described in Chapter 4 of this thesis, as its effect makes a significant impact on the efficiency of the later analysed modulation methods and is included in $E_{on(add)}$.

The switching energy losses of all switches are contained in $E_{off(tot)}$, $E_{on(tot)}$ and $E_{on(add)(tot)}$ for turn-off, turn-on and additional losses because of the lost ZVS turn-on, respectively, while the total switching power is:

$$P_{sw(sw)(tot)} = \left(E_{off(tot)} + E_{on(tot)} + E_{on(add)(tot)} \right) f_{sw} \, ,$$

(3.6)

where f_{sw} is a switching frequency.

3.3.1.3   Inductor, transformer and capacitor power losses

The power losses in the inductors and transformers consist of wire and core losses. If the air-core inductor is considered, the core losses are simply neglected.

The wire or copper losses are the power lost by current flowing through the winding. In the case of both the inductor and transformer, wire losses are calculated using:

$$P_{wire} = R_{wire}I_{wire(rms)}^2$$

(3.7)

where R_{wire} is the dc resistance of the winding wire, and $I_{wire(rms)}$ is the rms value of the current running through the winding. The skin and proximity effects are neglected due to the assumption that the wire used consists of a high number of separately insulated strands, which is a Litz wire. If the skin and proximity effects would be taken into account, additional ac losses would appear in the wire as the current would tend to flow near the surface of the inductor.

The core losses are caused by the variable magnetic field in the core material, and they directly depend on the frequency and magnetic flux swing. Since the ferrite materials are

usually used at the kilohertz frequency range, the eddy current losses in the core are neglected due to the high ferrite electrical resistance.

The magnetic core losses are calculated using a modified Steinmetz equation (MSE) [79] in the following way. The maximum reached (peak) flux density is calculated for the inductor and transformer as:

$$B_{ind(\max)} = N_{ind}\, I_{ind(\max)}\, \frac{\mu_0}{l_g} \tag{3.8}$$

$$B_{trafo(\max)} = \frac{1}{2N_{trafo}\, A_{core} f_{sw}} \int\limits_{0}^{1/2f_{sw}} v_{Lm}(t)dt \tag{3.9}$$

where N_{ind} and N_{trafo} are the number of winding turns for the inductor and transformer, respectively, $I_{ind(\max)}$ is the peak inductor current, μ_0 is the permeability of free space, l_g is the inductor air gap, A_{core} is the magnetic core effective cross section area, and v_{Lm} is the voltage applied over the transformer magnetizing inductance.

Next, the flux density change is determined by:

$$\Delta B_{ind} = N_{ind}\, \mu_0 \frac{\left(I_{ind(\max)} - I_{ind(\min)}\right)}{l_g}\,, \tag{3.10}$$

$$\Delta B_{trafo} = 2B_{trafo(\max)}\,. \tag{3.11}$$

Furthermore, the equivalent frequency is defined with:

$$f_{eq} = \frac{2}{\Delta B^2\, \pi^2} \int\limits_{0}^{1/f_{sw}} \left(\frac{dB}{dt}\right)^2 dt\,. \tag{3.12}$$

Finally, the core power losses for both the inductor and transformer are calculated using:

$$P_{core} = V_{core} \left(C_m\, f_{eq}^{\ \alpha-1}\, B_{(\max)}^{\ \beta}\right) f_r \tag{3.13}$$

where V_{core} refers to the total core volume, and f_r is the remagnetization frequency. C_m, α and β are the core material constants used for the calculation of losses in the original Steinmetz equation [80]. Those constants are determined using the core material documentation, where the power loss per volume dependence on the peak flux density and frequency is given. This data is usually given for the fixed temperature; therefore, the core loss temperature scaling coefficient can be included for a more accurate loss estimation because the ferrite core permeability tends to rise with the temperature until approx. 100 °C.

The capacitor power losses are determined using the same way as given in (3.7), since the dominant loss parameter in the capacitor is the equivalent series resistance (ESR):

$$P_{cap(\text{ESR})} = R_{ESR} I_{cap(\text{rms})}^2\,. \tag{3.14}$$

3.3.2   Converter efficiency during harvesting cycle definition

The PEC efficiency has different values for different voltages and currents, as required by the DEAP harvesting cycles. Therefore, the commonly used peak or average efficiency value does not give any information about the converter efficiency effect during DEAP energy harvesting. Thus, to determine the converter efficiency influence on the energy cycling, the converter efficiency during the harvesting cycle has to be defined.

The total power loss within the PEC, including losses in all switches, is calculated as:

$$P_{loss} = P_{sw(con)(tot)} + P_{sw(sw)(tot)} + P_{trafo(core)} + P_{trafo(wire)} + P_{ind(core)} + P_{ind(wire)} + P_{cap(ESR)} + P_{aux} , \qquad (3.15)$$

where ($P_{trafo(core)}$ + $P_{trafo(wire)}$) and ($P_{ind(core)}$ + $P_{ind(wire)}$) denote the power loss in transformer and inductor, respectively. The PEC efficiency during the DEAP generator charging (the power flow direction towards the DEAP generator) is further calculated using the total power loss and the DEAP generator power as:

$$\eta_c(i_{DE}, v_{DE}) = \frac{p_{DE}}{p_{DE} + p_{loss}}, \quad i_{DE} \geq 0 , \qquad (3.16)$$

whereas, during the DEAP generator discharging process, the PEC efficiency is given as:

$$\eta_d(i_{DE}, v_{DE}) = 1 - \frac{p_{loss}}{|p_{DE}|}, \quad i_{DE} < 0 . \qquad (3.17)$$

In (3.16) and (3.17), $p_{DE} = i_{GEN} \cdot v_{GEN}$ relates to the instantaneous DEAP generator power that goes to and from the DEAP generator during charging and discharging, respectively. Therefore, the PEC efficiency for the entire power range is defined as:

$$\eta(i_{DE}, v_{DE}) = \begin{cases} \eta_c(i_{DE}, v_{DE}), & i_{DE} \geq 0 \\ \eta_d(i_{DE}, v_{DE}), & i_{DE} < 0 \end{cases} \qquad (3.18)$$

For calculation purposes, the required DEAP generator current (i_{DE}) and voltage (v_{DE}) are obtained through simulation and a current optimization algorithm for the given sea wave conditions [29, 30]. Furthermore, the DEAP generator current and voltage are used as inputs to the equations for the energy loss of the converter:

$$E_{loss} = \int_0^{T_{cycle}} |i_{DE}(t)| v_{DE}(t) \cdot \begin{cases} \dfrac{1}{\eta(i_{DE}, v_{DE})} - 1, & i_{DE} \geq 0 \\ 1 - \eta(i_{DE}, v_{DE}), & i_{DE} < 0 \end{cases} \cdot dt \qquad (3.19)$$

and

$$\begin{aligned} E_{loss(cha)} &= E_{loss}\big|_{i_{DE} \geq 0}, \quad \text{DE charging} \\ E_{loss(discha)} &= E_{loss}\big|_{i_{DE} < 0}, \quad \text{DE discharging} \end{aligned} , \qquad (3.20)$$

where $E_{loss(\text{cha})}$ and $E_{loss(\text{discha})}$ denote the energies dissipated in the PEC during charging and discharging processes, respectively, and T_{cycle} denotes the cycle (wave) period. The total energy dissipated in the power electronic converter during one harvesting cycle is:

$$E_{loss} = E_{loss(\text{cha})} + E_{loss(\text{discha})} . \tag{3.21}$$

Finally, the converter efficiency during the harvesting cycle is defined as:

$$\eta_{conv(\text{cycle})} = \left[1 - \frac{E_{loss}}{E_{DE} + E_{loss(\text{cha})}} \right] \cdot 100\% , \tag{3.22}$$

where E_{DE} is the total (circulating) energy delivered to and withdrawn from the DEAP generator during charging and discharging processes, respectively, and it is defined as:

$$E_{DE} = \int_{0}^{T_{cycle}} |i_{DE}(t)| v_{DE}(t) dt . \tag{3.23}$$

The E_{DE} does not include losses in the DEAP material and its connections (but only theoretical DEAP energy), while the factor ($E_{DE}+E_{loss(\text{cha})}$) in the $\eta_{conv(\text{cycle})}$ calculation designates the total energy processed by the PEC during both energy transfer directions.

3.3.3 Loss estimation results

In the following, the results of the loss modelling are presented. The power loss distribution is given for each individual analysed converter at different switching frequencies, as well as efficiency surfaces and curves. At the initial stage, the employed switch is Si IGBT rated for a blocking voltage of 1.2 kV and a current of 30 A. This provides a good balance between switching and conduction losses, while still providing a high blocking voltage capability.

Each analysed converter is set to operate at six different switching frequencies. Each switching frequency filter component is defined and losses calculated. The inductor, transformer and capacitor components are rated for each individual frequency. The current ripple requirement for the inductors are kept constant, as well as the voltage ripple for capacitors, over the whole switching range. The same is valid for the transformers. Each component is designed to be optimized in terms of losses, as given in the Appendix.

Finally, all design results are used in the final topology comparison. However, the most important DEAP WEC application requirement, the converter cycle efficiency, has to be fulfilled. On the other hand, the converter overall volume is not considered at this stage, but that doesn't mean that the filter component is over-dimensioned.

3.3.3.1 Two-quadrant converter

In Figure 3.13 is given the loss distribution within the 2QC that operates at the maximum power point while discharging the DEAP generator. Different switching frequencies are

covered as well, while the filter components' size follow the frequency change. This can be noted in the given graph as the conduction losses remain unchanged while frequency varies.

As mentioned, the converter operates in the DEAP generator discharging mode, and that can be seen from Figure 3.13, as the diode conduction losses are significantly larger than the IGBT conduction losses. This is a result of the large step-down ratio that determines the switch duty cycle. Switching losses rise with the frequency, while the large inductor losses are almost unchanged; this is, again, a result of the inductor optimization for each frequency.

Figure 3.14 presents the 2QC efficiency surface for a 15 kHz switching frequency and different DEAP generator voltages and currents, all within the required power range. It can be seen that the surface tends to fall down slightly as the DEAP generator voltage and current increase above ~50% of their rated values. Overall, it maintains a high efficiency with the peak detected at 96.4%.

As previously presented in Figure 3.1, the converter mostly operates with the pulse current, while the DEAP generator voltage varies in a large spectrum. Therefore, attention has to be mainly pointed at the constant current – variable voltage efficiency curve. Figure 3.15 depicts these curves, again, for different switching frequencies.

3.3.3.2   Flying-capacitor multilevel converter

For the FCMC, similar efficiency behaviours can be observed, as previously described for the 2QC. However, the FCMC introduces significant losses in the capacitors that carry the main circulating current, as they are connected in series with the input inductor. The same as for the 2QC, here it can be observed that conduction losses remain unchanged for different switching frequencies, see Figure 3.16.

3.3.3.3   Cascaded multilevel converter

Contrary to the 2QC and FCMC, the CMC has significantly less losses at the same switching frequency, approximately 40% less (Figure 3.19). The presence of a large number of switches and driver circuits takes an impact on the power needs from the auxiliary power supply.

From Figure 3.20, it can be seen that the CMC efficiency surface has a different behaviour than the 2QC and FCMC. It provides the peak efficiency at the maximum power point, and then efficiency decreases as the power drops. For extremely low DEAP generator currents and voltages, the CMC efficiency drops rapidly, however, this is the part of the surface where the lowest power levels are transferred.
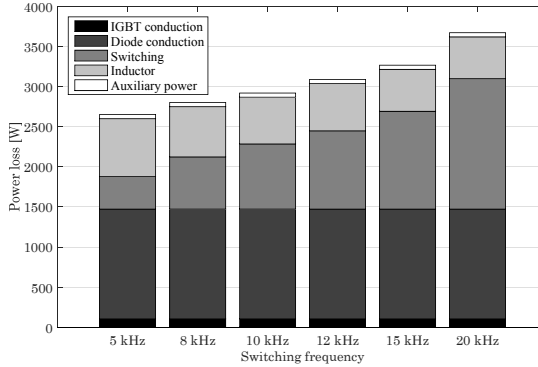
Figure 3.13: Two-quadrant converter loss distribution for different switching frequencies at the maximum power during the DEAP generator discharging process (V_{DE} = 10 kV and I_{DE} = 5 A); filter capacitor and small filter inductor losses are not included in the graph, because they are less than 2% of the total loss
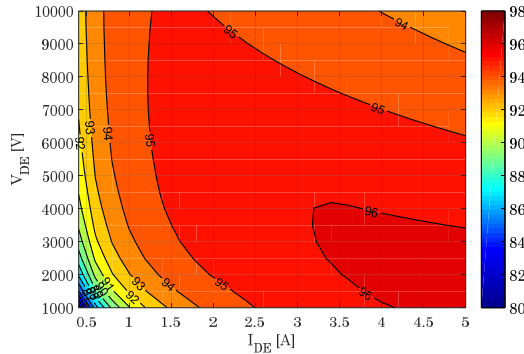
Figure 3.14: Two-quadrant converter efficiency surface for the DEAP discharging process and 15 kHz switching frequency
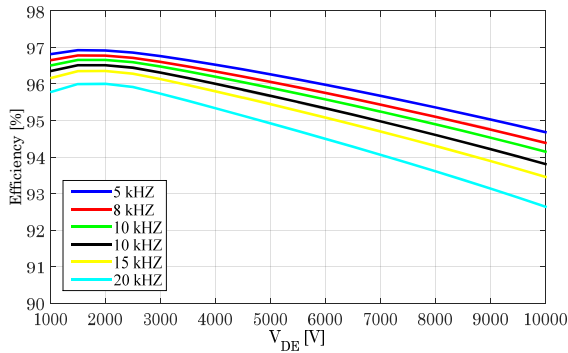
Figure 3.15: Two-quadrant converter efficiency curves for the fixed DEAP generator current at 5 A and different DEAP generator voltages and switching frequencies
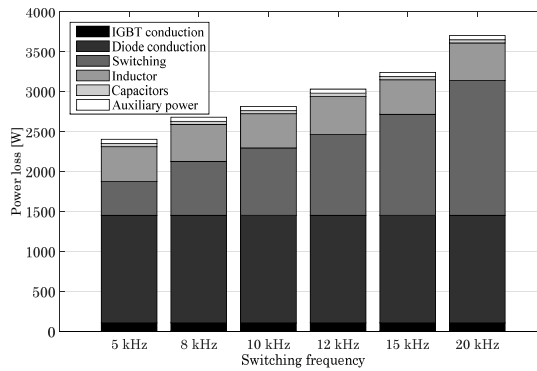
Figure 3.16: Flying-capacitor multilevel converter loss distribution for different switching frequencies at maximum power during the DEAP discharging process (V_{DE} = 10 kV and I_{DE} = 5 A); filter capacitor and small filter inductor losses are not included in the graph, because they are less than 2% of total losses
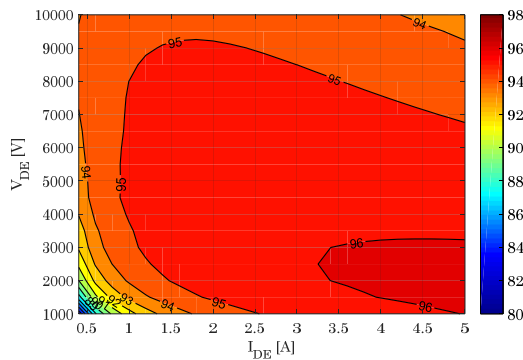
Figure 3.17: Flying-capacitor converter efficiency surface for the DEAP generator discharging process and 15 kHz switching frequency
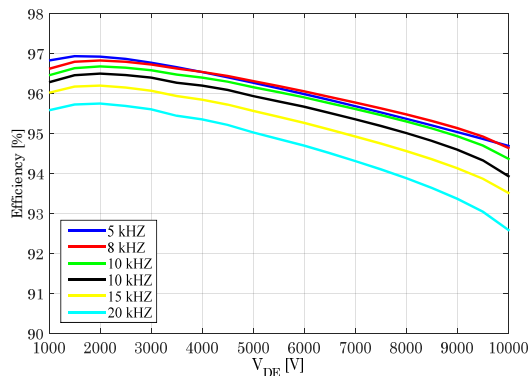
Figure 3.18: Flying-capacitor multilevel efficiency curves for the fixed DEAP generator current at 5 A and different DEAP generator voltages and switching frequencies
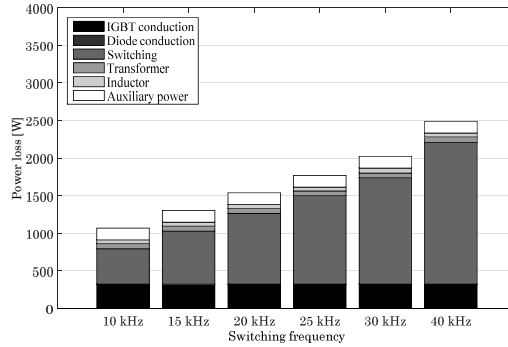
Figure 3.19: Cascaded converter loss distribution for different switching frequencies at maximum power during the DEAP discharging process (V_{DE} = 10 kV and I_{DE} = 5 A); filter capacitor and small filter inductor losses are not included in the graph, because they are less than 2% of total losses
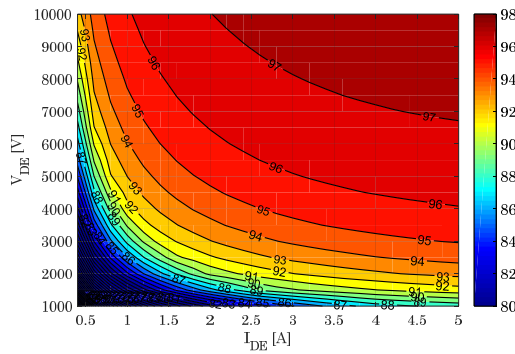
Figure 3.20: Cascaded converter efficiency surface for the DEAP discharging process and 15 kHz switching frequency
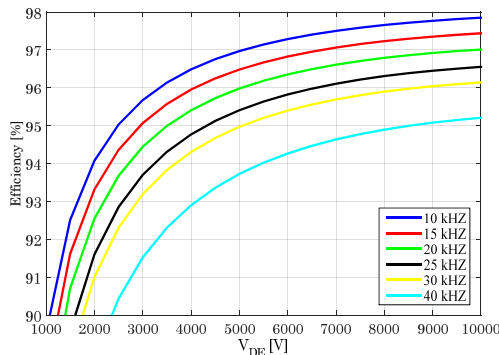
Figure 3.21: Cascaded multilevel converter efficiency curves for the fixed DEAP generator current at 5 A and different DEAP generator voltages and switching frequencies

3.3.3.4 Switching frequency determination

Figure 3.22 presents the converter cycle efficiency tendency based on the loss modelling for six different switching frequencies. The specific target sea wave condition that has the highest appearance number is taken, that is a 6 s wave period and capacitance ratio of 0.35, and its optimized waveforms are given in Figure 3.23. Note that the application that required a minimum converter cycle efficiency (95%) is marked. The converter should not be designed for a cycle efficiency below 95%, hence, the chosen switching frequencies for converters are the following:

- Two-quadrant converter: 15 kHz,
- Flying-capacitor multilevel converter: 15 kHz,
- Cascaded multilevel converter: 30 kHz.

This result clearly shows the efficiency superiority of the CMC above other analysed converters for the DEAP WEC application, as it can operate at twice the frequency while dissipating the same amount of power.
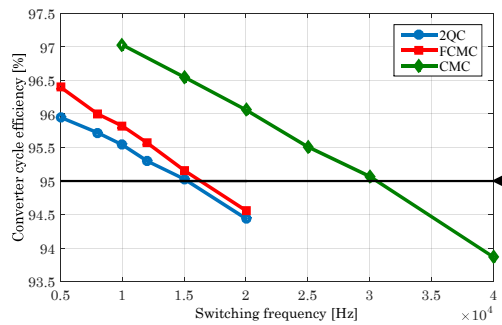
Figure 3.22: Converter cycle efficiency points and cycle efficiency tendency for variable switching frequency and wave conditions: 6 s period and 0.35 capacitance ratio. The required application minimum of 95% is marked
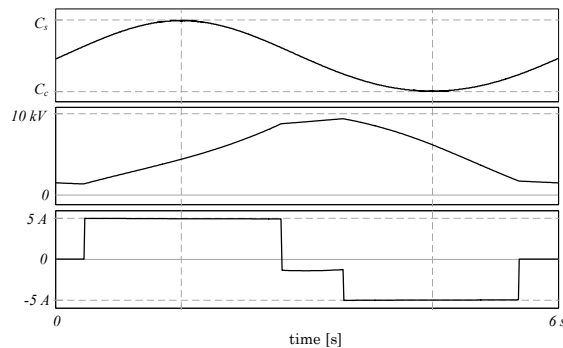
Figure 3.23: Calculated optimized voltage and current DEAP generator waveforms for a wave period of 6 s and capacitance ratio of 0.35, including the optimal residual charge left on the DEAP film

3.4   COMPARISON FRAMEWORK AND COMPARISON RESULTS

In this section, a topology comparison framework is described and overall comparison results are given. The outcome of this section determines the main course of the future dc-dc converter investigation for the DEAP WEC application.

3.4.1   Comparison framework

A framework is created for the comparative investigation of topologies to make the comparison well-founded.

In the following section, all comparison criteria are given and explained in terms of importance. The comparison is done in such way that each criterion carries its own weight factor, W (one to five). The topologies are rated (one to five) for each criterion, and then the rating (r) is multiplied with the weight factor of the particular criterion. The sum of all these multiplications per topology results in a total rating (T_i) of a certain converter, given by:

$$T_{rating,i} = \sum_{j=1}^{N_{cri}} W_j\, r_{ij} \tag{3.24}$$

where i is an ordinal number of the topology, j is an ordinal number of the criterion, and N_{cri} the total number of criteria. The converter with the highest rating is the best suited for the given DEAP energy harvesting application.

3.4.1.1   Converter cycle efficiency

The converter efficiency during the harvesting cycle ($W_1 = 5$) is the most important criterion because the converter is part of the system for energy production. It carries the highest weight of five, and the ratings are presented in Table 3.5.

Table 3.5: Converter cycle efficiency criterion ratings

	Number of switches [$W_4 = 5$, $j = 4$]				
	< 92%	92-94%	94-96%	96-98%	> 98%
rating (r)	5	4	3	2	1

3.4.1.2   Controllability

The controllability ($W_2 = 4$) addresses the control complexity of a given topology, as well as how hard it is to realize the proper operation of the converter. It carries a weight of four, and the ratings are presented in Table 3.6. An unknown controllability means that the converter is completely new. Solvable means that it is possible to apply certain control methods, but it is not fully tested yet. A hard control method is known but difficult, complex and CPU intensive. A control with minor problems appoints small problems, while easy means that many control methods are known and tested, which are simple to implement.

Table 3.6: Complexity criterion ratings

	Controllability [$W_2 = 4, j = 2$]				
	unknown	solvable	hard	minor problems	easy
rating (r)	1	2	3	4	5

3.4.1.3 Stacking of switches

The stacking of switches ($W_3 = 5$, $j = 3$) criterion appoints a requirement for a special investigation, the time to develop and test stacked switches. It carries the highest weight of 5. The rating is determined based on the stacked switches requirement. If the converter requires a series stack of switches, its rating for this criterion is 1, and if not, then $r = 5$.

3.4.1.4 Number of switches

The number of switches ($W_4 = 4$) directly affects the complexity and cost of the converter. For this criterion, the lowest rated switch of all modelled switches is used (Si IGBT including an anti-parallel diode, with maximum ratings of a 1.2 kV blocking voltage and 30 A of continuous drain current). It carries a weight of four, and the ratings are presented in Table 3.7.

Table 3.7: Number of switches criterion ratings

	Number of switches [$W_4 = 4, j = 4$]				
	< 50	51-90	91-130	131-170	> 171
rating (r)	5	4	3	2	1

3.4.1.5 Number of diodes

The number of additional diodes ($W_5 = 2$) affects the cost of the converter. This criterion does not include the anti-parallel diodes, and all diodes are assumed to have the same blocking voltage rating of 1.2 kV. This carries a weight of two, and the ratings are presented in Table 3.8.

Table 3.8: Number of diodes criterion ratings

	Number of diodes [$W_5 = 2, j = 5$]				
	< 50	51-90	91-130	131-170	> 171
rating (r)	5	4	3	2	1

3.4.1.6 Total size of capacitance

The total capacitance of all capacitors ($W_6 = 3$) directly affects the cost and size of the converter. All capacitors are rated for 800 V dc, so only the capacitance required for a topology is taken for the comparison (summation of all capacitors). It carries a weight of three, and the ratings are presented in Table 3.9.

Table 3.9: Total size of capacitances criterion ratings

	Total capacitance [W_6 = 3, j = 6]				
	< 25 µF	26-45 µF	46-65 µF	66-85 µF	> 85 µF
rating (*r*)	5	4	3	2	1

3.4.1.7 Total size of inductance

The total size of the inductance (W_7 = 3, j = 7) affects the cost and size of the converter. Inductors are not rated for the same current, so for the comparison purposes, the maximum energy that can be stored in the inductor's magnetic field is used. This criterion carries a weight of 3, and the ratings are presented in Table 3.10.

Table 3.10: Total inductance criterion ratings

	Total inductance [W_7 = 3, j = 7]				
	< 5 mJ	6-50 mJ	51-250 mJ	251-500 mJ	> 500 mJ
rating (*r*)	5	4	3	2	1

3.4.1.8 Number of transformers

The number of transformers (W_8 = 3, j = 8) affects the cost and size of the converter. Because only one topology (CMC) employs transformers, this mode is given a rating of 1, while the rest of the topologies have a rating of 5. If more than one topology would have a transformer, then the best solution is to merge all inductive elements (inductors and transformers).

3.4.1.9 Efficiency improvement

Some topologies have a high potential for efficiency improvement (W_9 = 3, j = 9), thus, it is important to emphasize this characteristic. It is basically connected with the control methods that can be employed to improve the efficiency of the converter. This criterion carries a weight of three, and the converter is rated with five if there is a possibility for a much higher efficiency (at least 2% higher) improvement, and if not, the rating is one.

3.4.1.10 Output current ripple

Although the output current ripple (W_{10} = 3) has a small influence on the total system efficiency, the heating of the DEAP because of a high series resistance can cause a change in the DEAP characteristics. For comparison purposes, the ratio of I_{rms_DE} / I_{DE} (root mean square and DEAP generator current) is taken into account. This criterion carries a weight of three, and the ratings are presented in Table 3.11.

3.4.1.11 Modularity and possibility of expanding

Modularity and possibility of expanding (W_{11} = 1) are the capability of a converter to be easily upgraded or downgraded in terms of voltage processing ability. This criterion should

indicate the complexity of the production process as well. It carries a weight of one, and the ratings are presented in Table 3.12.

Table 3.11: Output current ripple criterion ratings

	Output current ripple influence [W_{10} = 3, j = 10]				
	< 1.2	1.2-1.4	1.4-1.6	1.6-1.8	> 2
rating (r)	5	4	3	2	1

Table 3.12: Modularity and expanding criterion ratings

	Modularity and expanding [W_{11} = 1, j = 11]		
	impossible	hard	easy
rating (r)	1	3	5

3.4.2   Comparison results

All criteria ratings of the compared topologies and their total ratings are summarized in Table 3.13 for the topology investigation and only one type of switch at the initial research stage.

For the comparison purposes, it is chosen to select a fixed efficiency for all topologies. For different switching frequencies, the converters are modelled, and their efficiencies are calculated. The target converter efficiency during the harvesting cycle is >95%, and when the converter satisfies this condition, other parameters (capacitances, inductors, etc.) are provided through the switching frequency.

Because only three topologies are modelled in full detail, only those three can be truly compared (2QC, FCMC and CMC). Based on the total rating, the cascaded multilevel converter is the best suited topology for this application, and it also meets all the requirements. Its modular design makes the production process easier. Furthermore, many modulation and control methods can be employed for the CMC that can directly affect or improve the efficiency. It is important to stress that once again the dc-bus voltage of 800 V is used for the topology investigation at the initial research stage.

3.5   CONCLUSIONS

To satisfy the requirements for the constant electric-field energy harvesting method using dielectric elastomers, three topologies are proposed, investigated and compared. The biggest limiting factor is the 10-kV voltage that can appear over the dielectric elastomer material, which limits the number of possible topologies. Multilevel converters allow usage of low-voltage switches, and therefore, it is not necessary to stack switches, as in the two-quadrant converter. However, multilevel converters require additional components and special control methods to keep the blocking voltages over the switches balanced.

Table 3.13: Comparison results

Criterion (j)	Weight (W_j)	Converter topology ratings		
		2QC (i=1)	FCMC (i=2)	CMC (i=3)
1. Converter efficiency	5	3	3	3
2. Controllability	4	5	3	5
3. Stacking of switches	5	1	5	5
4. Number of switches	4	2	3	3
5. Number of diodes	2	5	5	5
6. Total capacitor size	3	1	1	5
7. Total inductor size	3	1	3	4
8. Number of transformers	3	5	5	1
9. Efficiency improvement	3	1	1	5
10. Current ripple	3	5	5	5
11. Modularity	1	3	3	5
	$T_{rating(i)} =$	100	122	147

In this chapter, a special comparison framework is created and presented to perform a comparison of different power electronic converter topologies and to satisfy the application requirements. Furthermore, the initial converter design of the investigated topologies is conducted for comparison purposes, as well as the loss estimation and definition of the converter efficiency during harvesting cycle. As shown, lower switching frequencies provide an overall higher efficiency of the converter. However, the volume reserved for the power converter is the limiting factor. Comparison results show that the cascaded multilevel converter is the most suitable topology for the dielectric elastomer energy harvesting application. Therefore, the cascaded multilevel converter is chosen for further development and testing. Its modular design allows for easier and cheaper production process, especially if mass produced for wave energy applications.

Chapter 4

Modulation method for dual active bridge

4.1 INTRODUCTION

Since the selected PEC for the DEAP WEC system has a modular multilevel bidirectional topology (CMC, see Figure 4.1), with modules based on the dual active bridge circuit, further analysis investigates several modulation methods for the single DAB circuit. Furthermore, the focus is on the DAB efficiency optimization, as the wave harvesting application requires minimized losses during large energy circulation.

Here, the main challenge for the DAB, or any other converter for that matter, is special operating conditions, as described in section 3.1, i.e., a wide voltage and pulse current operation, coupled with the high efficiency requirement. These operating conditions can be provided by employing a two-stage converter design, like in the case of the CM converter. Then, the first stage takes care of the usually critical voltage levels, while the second stage provides the necessary voltage and current levels to the output. The second stage, in that case, relies on the voltage provided by the first stage. However, the two-stage converter could provide more losses than the one stage alone. This is usually applicable to the maximum output power point of the converter. Still, the overall efficiency depends on the converter's behaviour over the whole obligatory voltage-current domain. Therefore, the whole voltage-current domain must be investigated to state any further conclusions. In the literature, DAB circuits usually operate with very stiff input/output voltages and very rarely with the voltage variations up to 50%. Here, the pulse current and very wide (5–100%) voltage range are the subject of investigation, which are significantly different from the standard DAB operation conditions.
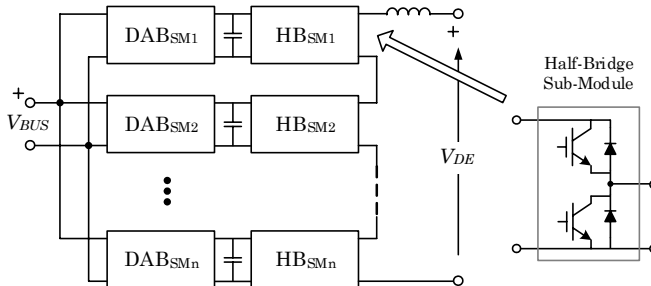
Figure 4.1: Cascaded multilevel dc-dc converter with the DAB for voltage isolation and voltage balancing of the intermediate dc capacitor voltage

The main issues addressed in this chapter are:

- Efficiency optimization by modifying the module of the previously selected CM topology;
- Modulation methods for the DAB circuit, their limitations and operating domains;
- Modulation method suitable for the very wide voltage and pulse current operation of the DAB;

- Optimized DAB modulation method from an efficiency point of view and for the required wide power operating range.

4.2 DUAL ACTIVE BRIDGE

4.2.1 Basic operation principle

The dual active bridge has many switching redundancy states, which are a result of eight employed switches. By imposing the voltage over the transformer leakage inductance, the current is controlled, and therefore, the power flow. Figure 4.2 shows the basic principle of the power transfer control in the DAB circuit using the transformer leakage inductance as an intermediate stage and energy tank.

The difference between voltages v_{T1} and v_{T2} results in a voltage v_{Lk} imposed over the inductance of L_k. Furthermore, the imposed voltage v_{Lk} increases or decreases the energy stored in the inductor L_k, depending on the v_{Lk} voltage sign and previous current direction.

Since the imposed voltage changes the inductor's energy, the current must be changed as well. The inductor current increment is defined as:

$$di_{Lk}(t) = \frac{1}{L_k} \int v_{Lk}(t) dt . \tag{4.1}$$

Therefore, if the imposed voltage, v_{Lk}, is positive the inductor current (i_{Lk}) is increasing, otherwise the current is decreasing. Note that if the applied v_{Lk} is negative, the current i_{Lk} might change the sign (direction), while its energy will grow with the negative increment of the negative current i_{Lk}.

From Figure 4.2, it can be seen that the voltage sources are alternating (ac sources). The reason for this lies in the DAB circuit structure, see Figure 4.3. The DAB consists of two full bridges and the transformer – a high frequency galvanic isolation ac link. L_k denotes the transformer leakage inductance, while n is the transformer turn ratio. The transformer turn ratio is the ratio between the number of turns in the secondary and primary winding.
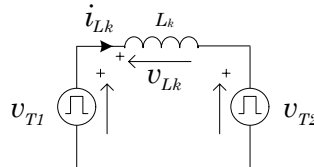
Figure 4.2: DAB power transfer basic circuit including inductance (L_k) as the transformer leakage inductance representation

Note that voltages v_{T1} and v_{T2}, from Figure 4.3, correspond to voltages v_{T1} and v_{T2}, from Figure 4.2, respectively. In Figure 4.4, the block diagram representation of the DAB circuit is presented.
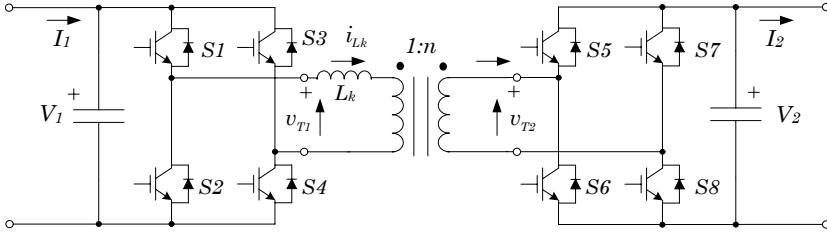
Figure 4.3: Dual active bridge circuit employing IGBT switches
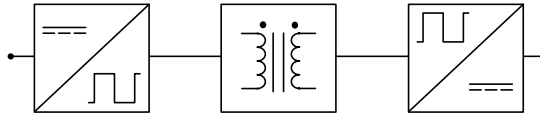
Figure 4.4: DAB block diagram representation

4.2.2   DAB topology variations

Figure 4.2 shows that it is possible to transfer power from one voltage source to another without using v_{T1} and v_{T2} as ac voltage sources, but also as dc voltage sources. Then, the question raises, "Why the ac sources are used when the dc sources could also transfer the power, and additionally, halve the number of switches in the DAB?" In that case, each dc source would comprise only one leg, thus, two switches, instead of four for the ac source (note that the bidirectional power transfer capability has to be maintained). However, in the case of dc sources, only half of the transformer magnetic hysteresis loop would be used. Therefore, significantly less power is available to transfer, while the transformer current would have high peaks (in which the switching transition occurs and high rms value because of its triangular shape). This is very similar to what can be found in a flyback converter, which is usually employed for isolation dc-dc power supplies up to 300 W.

As presented in Figure 4.5, it is possible to keep a few switches and still provide the ac voltage source to the transformer windings. This is achieved by employing dc capacitors (*C1–C4*) instead of switches in one leg per ac voltage source. The placed dc capacitors are splitting equally the main dc voltage at the input/output, while their voltages are balanced.

The DAB comprising dc capacitors and dual active half-bridge can impose only half of the main dc link voltage to the transformer windings. Therefore, to transfer the same amount of power as the DAB from Figure 4.3, the dual active half-bridge should have a two-times higher current circulating through the transformer and switches. Thus, even it counts few switching components, the dual active half-bridge needs components with a higher current
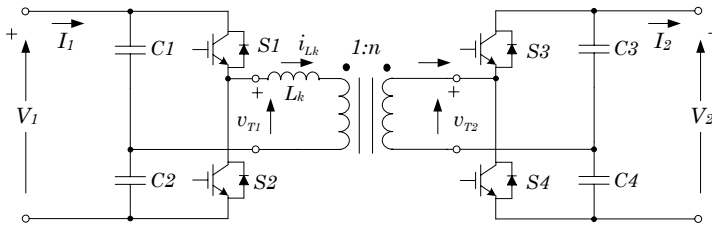
Figure 4.5: Dual active half-bridge comprising dc capacitors to split the main input/output dc voltage

rating. Furthermore, because of a few switches, it lacks the number of switching states (combinations) of the DAB circuit, e.g., it cannot provide zero voltage to the transformer winding.

Generally, power semiconductor switches have characteristics that are changing with the blocking voltage capability, accordingly. If the switch maximum blocking voltage is increased, the conduction resistance will increase as well, as more material is added to the conduction path to follow the blocking voltage change. Therefore, assuming the same maximum conduction current capability of the switch, it is better to employ lower voltage switching devices to decrease conduction losses. Consequently, the number of modules, in the overall multilevel converter, can be increased for the sake of higher efficiency, while the modules would be rated for lower voltage. However, in the case of the CM converter, an additional half-bridge at the generator side could suffer from higher losses, if the IGBT switches are employed in the circuit. The reason for this is the bipolar characteristic of the IGBT switches, as they have V_{CE0} voltage across collector-emitter during zero collector current (P-N junction polarization voltage). The V_{CE0} voltage affects conduction losses, and it does not significantly change with the blocking voltage capability of the switch. However, in the case of MOSFET switches, the V_{CE0} does not exists, as MOSFETs are unipolar devices. As a result, designing the module to deal with the lower voltages is not a straightforward solution and reduces the reliability of the whole system, as a high number of active components is involved.

Instead of going for the module with the lower voltage rating, and therefore, large number of modules, the solution could be found in multilevel converter topologies. As mentioned before, multilevel converters are employed if it is necessary to deal with high voltage in the circuit, while the switches are rated for low voltage. Additionally, multilevel converters can reduce the size of the filter components, as they can provide the step change of the output signal.

The suitable multilevel topology for the DAB is the diode-clamped, see Figure 4.6. Each used switch in the diode-clamped DAB circuit blocks half of the main module dc voltage. Therefore, two solutions could take place: to use the same voltage for the switches as in the DAB, and therefore, halve the number of modules, or to use two-times lower voltage for the switches and keep the same number of modules as with the DAB. The second option seems to have lower losses, as the lower voltage devices have better characteristics. The problem
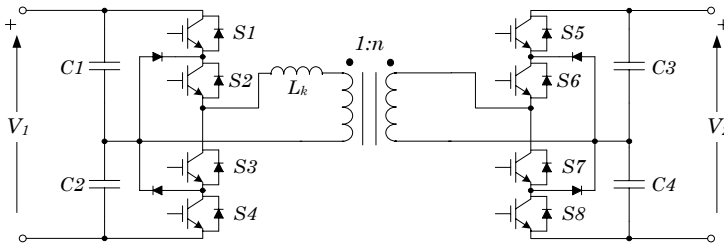
Figure 4.6: Diode-clamped DAB circuit

with the first option is that the CM additional half-bridge has to block high voltage, suggesting that another multilevel converter could be used or just high voltage switches in the half-bridge.

Furthermore, the diode-clamped DAB can impose only half of the main module voltage, as it employs the same dividing dc capacitors as the dual active half-bridge. Therefore, the DAB's components would have to be oversized in terms of current capability. Additionally, all switching transitions would occur at high current instances, which implies high switching losses, beside the high rms value of the circulating current inside the DAB. Furthermore, it is important to stress that the diode-clamped, like other multilevel topologies, requires proper balancing of the dividing capacitors voltages to keep the converter operational and without destroyed switches. This balancing requirement would come on top of the already existing balancing of each module's voltage, since the overall converter is also multilevel.

The DAB could be created using three-phase bridges on each side of the transformer, see Figure 4.7. However, the transformer needs to have a three-phase construction as well. The three-phase DAB results in an overall lower rms transformer current and smaller filter capacitors. Therefore, it is the best choice for high current applications [81-83]. However, for the DEAP WEC application the required current is low. Furthermore, the three-phase transformer has a more complex design [83], and the number of active switch devices is 50% higher than in the single-phase DAB.

As a result, further investigation continues with the single-phase DAB circuit as the best solution from an efficiency, complexity and controllability point of view. However, the system comprising DABs might have a lower reliability than the mentioned diode-clamped DABs. The detailed reliability analysis is not in the scope of the thesis but is not totally omitted from consideration.

4.3 SINGLE-STAGE MULTILEVEL CONVERTER MODULE MODULATION

Based on the DEAP WEC's electrical requirements and the investigation done in Chapter 3, the cascaded multilevel dc-dc topology is chosen as a starting point, see Figure 4.1. The basic electrical units of the CM converter are two-quadrant voltage source (half-bridge)
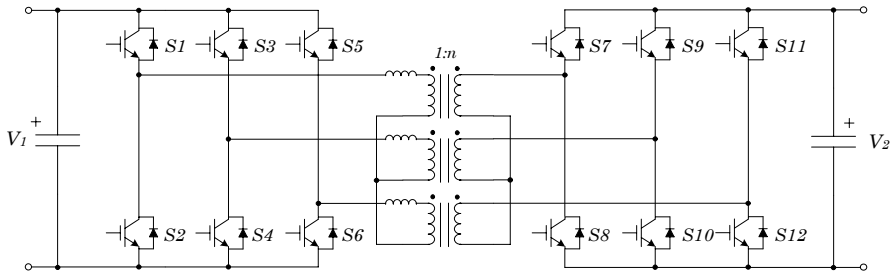
Figure 4.7: Three-phase DAB circuit

converters that are connected in cascade, thus, building up the output voltage. A desirable CM converter output voltage is achieved by controlling the half-bridge sub-modules. Nonetheless, the sub-module's dc capacitor voltage is kept constant, and its balancing is done using DAB converter. Therefore, the DAB connected to the half-bridge converter makes one module of the CM converter together with the intermediate dc-link capacitor.

However, to increase the overall module efficiency, the half-bridge could be removed from the CM module, thus, providing the DAB circuit alone to operate as a single module. This modification to the CM converter creates a modular multilevel dc-dc converter with only DAB modules connected in parallel at the input and in series at the output (input parallel output series - IPOS), see Figure 4.8. The IPOS converter differs from the CM converter as it has one stage less. This indicates a potential higher efficiency level at the high power
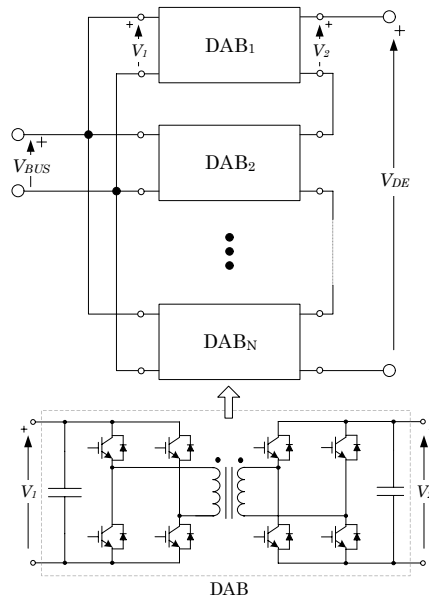
Figure 4.8: IPOS converter with a DAB module as its elementary building block

transfers. However, the applied modification does not come without additional complications, as the DAB would have to deal with the extremely wide voltage variations at the DEAP generator side, while delivered current is kept at its peak value. The following analysis investigates the limitations and operating ranges of several proposed DAB modulation techniques to find the optimal modulation.

4.3.1 Phase-shift DAB modulation

The phase-shift DAB modulation is employed in the Chapter 3 of this thesis, but has not been explained in detail. The phase-shift modulation is the most known and widely used technique for power transfer between ac sources. It is no different for the DAB circuit as well, as it has two ac voltage sources coupled with the transformer [56, 84, 85], see Figure 4.4.

As mentioned before, in the DAB circuit, the power transfer is controlled by adjusting the voltage imposed over the leakage inductance of the transformer. In the case of phase-shift modulation, the imposed voltage is defined with the phase shift (x) of the used voltage ac sources (from a transform point of view). Each full-bridge (voltage ac source) generates ac voltage at the fixed frequency and equally long positive and negative periods. Furthermore, the phase difference between primary and secondary side ac voltage sources defines the duration of imposed voltage over the inductance $L_{k,}$ and therefore, influence the transformer current accordingly. This principle is well described and analysed in the literature over the years and is widely used in the converter and power transfer applications.

Figure 4.9 shows DAB signals employing the phase-shift modulation method. Note that all switches operate with a constant duty cycle of 0.5, where the duty cycle is, by definition, the ratio between the on-state and full switching period of the switch. Additionally, in each full-bridge, the internal phase shift of half the switching period is applied between the legs to create an alternating voltage at its output, without a zero value. Additionally, a noticeable small circulating current that appears, e.g., when the positive input voltage is applied over $L_{k,}$ and the transformer current has a negative value. This results in a power that flows back to V_1. The same can be observed for the second H-bridge and V_2, when the transformer current is also negative.

The transformer current (i_{Lk}) shape is altered only with the phase-shift, output voltage, input voltage and the switching frequency. It is not possible to shape the transformer current otherwise, since the transformer ratio (n) and leakage inductance (L_k) are fixed.

To explain the phase-shift DAB modulation operation and operating voltage limitation, the basic set of equations is presented:
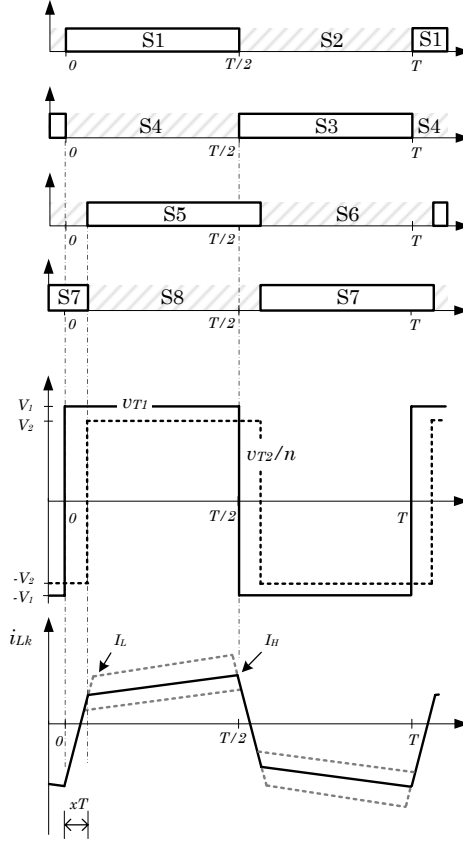
Figure 4.9: Transformer current (i_{Lk}) for the phase-shift DAB modulation

$$i_{Lk}(t) = \begin{cases} \dfrac{1}{L_k}\left(V_1 + \dfrac{V_2}{n}\right)t + i_{Lk}(0), & 0 < t < xT \\[3mm] \dfrac{1}{L_k}\left(V_1 - \dfrac{V_2}{n}\right)(t - xT) + i_{Lk}(xT), & xT < t < T/2 \end{cases}, \qquad (4.2)$$

where T is the switching period, and x is the phase shift. From the condition:

$$i_{Lk}(0) = -i_{Lk}(T/2) = -I_H, \qquad (4.3)$$

the transformer current (i_{Lk}) can be calculated at 0 s and xT as:

$$i_{Lk}(0) = \frac{1}{2L_k}\left(\frac{V_2}{n}\left(\frac{T}{2} - 2xT\right) - V_1\frac{T}{2}\right), \qquad (4.4)$$

$$i_{Lk}(xT) = \frac{T}{4L_k}\left(V_2 + V_1(4x - 1)\right) = I_L. \qquad (4.5)$$

Now, the power that the DAB delivers using the phase-shift modulation, considering lossless DAB operation, can be expressed as:

$$P_2 = V_1 I_1 = V_2 I_2 = V_1 \frac{2}{T} \int_0^{T/2} i_{Lk}(t)dt = V_2 \frac{2}{T} \int_{xT}^{xT+T/2} i_{Lk}(t)dt = \frac{T}{L_k} V_1 V_2 x \left(1-2x\right). \tag{4.6}$$

Note that the maximum power transfer is achieved for $x = 0.25$, as it can be derived from (4.6), see Figure 4.10. The DAB can even operate with x beyond 0.25, and those values are not used as the circulating current becomes very large, substantially impacting the efficiency. Therefore, the DAB mostly operates within the phase shift range of $0 < x < 0.25$.

The phase-shift DAB modulation ensures low switching losses as it employs the ZVS, however, the limits of the ZVS are determined mainly with the input to output voltage ratio. The ZVS is provided if the transformer current (i_{Lk}) has a negative sign and enough energy to discharge switch output capacitance and make the associate anti-parallel diode conductive, before the actual switch (IGBT) turn-on takes place. The same mechanism is valid for both H-bridges in the DAB, however, they require opposite signs of the transformer current. From the condition of the negative $i_{Lk}(0)$ and positive $i_{Lk}(xT)$, the following relations define the boundaries of the ZVS:

$$i_{Lk}(0) < 0 \quad \Rightarrow \quad x > \frac{1}{4}\left(1 - \frac{nV_1}{V_2}\right), \quad \frac{V_2}{n} > V_1, \tag{4.7}$$

$$i_{Lk}(xT) > 0 \quad \Rightarrow \quad x > \frac{1}{4}\left(1 - \frac{V_2}{nV_1}\right), \quad \frac{V_2}{n} < V_1. \tag{4.8}$$

According to (4.7) and (4.8), the ZVS area is defined with a minimum phase shift (x), determined using the applied voltage ratio for voltage step-up and step-down modes, separately. Figure 4.11 gives the calculated boundaries of the ZVS when different voltage
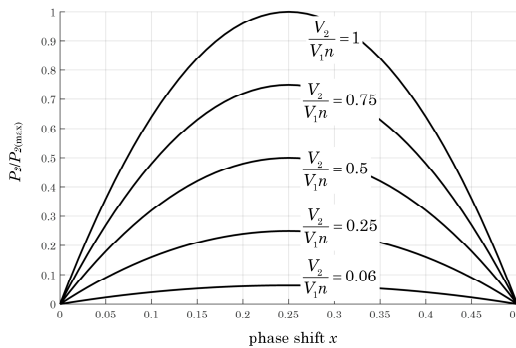
Figure 4.10: DAB under phase-shift modulation power output dependence on the phase shift and different voltage ratios
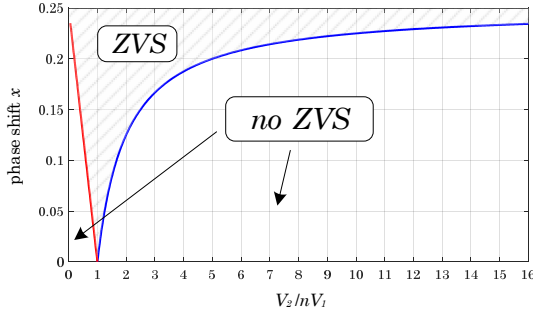
Figure 4.11: ZVS area for the DAB under phase-shift modulation

ratios are taken into consideration. Note that the ZVS area is quite narrow, and therefore, the phase-shift modulation should be applied on the DAB if voltage ratios are stiff, i.e., close to unity. However, the DEAP WEC application requires a very wide voltage ratio range, hence, the phase-shift modulation may not be suitable from an efficiency perspective, as loss of the ZVS results in significant switching losses. To maintain the ZVS in most of the operating area, the transformer inductance has to be chosen carefully. The required leakage inductance can be expressed and calculated from (4.6), as the power and voltages are known in advance; x is determined from Figure 4.11, and the switching frequency chosen based on a converter loss and/or volume criteria.

On the other hand, most of the power transfer to and from the DEAP generator is performed while keeping current at its maximum value. Therefore, the phase-shift modulation could be a good solution for the given application. However, before any final conclusions are made, other DAB modulation methods have to be analysed.

4.3.2   Trapezoidal DAB modulation

Basically, two sub-modes are distinguished within trapezoidal modulation. Both of the analysed trapezoidal DAB modulation modes are named after the transformer current shape [56, 85]. In contrary to the phase-shift modulation, the control of the transformer current is easy and has many freedoms, as each H-bridge provides a variable phase shift between its switch legs. Now, this increases the complexity of the modulation but could result in an overall better efficiency as there is no circulating currents, as in phase-shift modulation.

Assuming lossless DAB operation, a set of fundamental equations for the trapezoidal modulation is used as a starting point for both the modulation modes and sub-modes:

$$i_{Lk}(t) = \begin{cases} \dfrac{1}{L_k}V_1 t, & 0 < t < x_1 T \\ \dfrac{1}{L_k}\left(V_1 - \dfrac{V_2}{n}\right)(t - x_1 T) + i_{Lk}(x_1 T), & x_1 T < t < (x_1 + x_2)T \\ \dfrac{1}{L_k}\left(-\dfrac{V_2}{n}\right)(t - (x_1 + x_2)T) + i_{Lk}((x_1 + x_2)T), & (x_1 + x_2)T < t < (x_1 + x_2 + x_3)T \end{cases} \quad , \quad (4.9)$$

$$i_{Lk}(x_1 T) = I_L, \ i_{Lk}((x_1 + x_2)T) = I_H \tag{4.10}$$

$$x_1 + x_2 + x_3 \leq \frac{1}{2}, \tag{4.11}$$

$$I_{2(av)} = \frac{1}{T}\int_{x_1 T}^{(x_1 + x_2 + x_3)T} i_{Lk}(t)dt \ \Rightarrow \ I_{2(av)} = x_2\left(I_L + I_H\right) + x_3 I_H, \tag{4.12}$$

$$I_{1(av)} = \frac{1}{T}\int_{0}^{(x_1 + x_2)T} i_{Lk}(t)dt, \ I_{1(av)}V_1 = I_{2(av)}V_2 \ \Rightarrow \ I_{2(av)} = \frac{V_1 n}{V_2}\left(x_1 I_L + x_2\left(I_L + I_H\right)\right), \tag{4.13}$$

$$x_1 = \frac{I_L L_k}{V_1 T}, \ x_2 = \frac{\left(I_H - I_L\right)L_k}{\left(V_1 - \dfrac{V_2}{n}\right)T}, \ x_3 = \frac{I_H L_k n}{T V_2}, \tag{4.14}$$

where $I_{2(av)}$ is the average output DAB current, while x_1, x_2, x_3, I_H and I_L are marked in Figure 4.12. In the following analysis, it is taken that the DAB circuit behaves the same regardless of the power transfer direction (positive or negative output current), as lossless converter operation is assumed. Therefore, all presented graphs only show positive currents, whereas the negative current operation is similar. As the DAB forms the main building block of the proposed IPOS converter, most of the analysis is done for a single DAB module.

The trapezoidal modulation mode provides both zero voltage switching (ZVS) and zero current switching (ZCS) [56, 57]. The ZVS will occur if energy stored in the transformer leakage inductance (L_k) is enough to completely discharge the total equivalent output capacitance of the switch, as seen by the circuit. There are no special transformer current requirements that limit the ZVS area, as in phase-shift modulation. Energy stored in L_k depends on squared current value of i_{Lk} at the moment the transition occurs, while the total equivalent output capacitance of the switch includes the switch's built-in output capacitance, additional snubber (if any) and parasitic capacitances.

4.3.2.1 First trapezoidal sub-mode (I sub-mode)

The first sub-mode is depicted in Figure 4.12. It can be seen that all parameters are changing (x_1, x_2, x_3, I_L, I_H). However, the condition to be fulfilled is $x_1 + x_2 + x_3 = 0.5$. In practical implementations, for the sum of all these three periods, a value of 0.49 is chosen
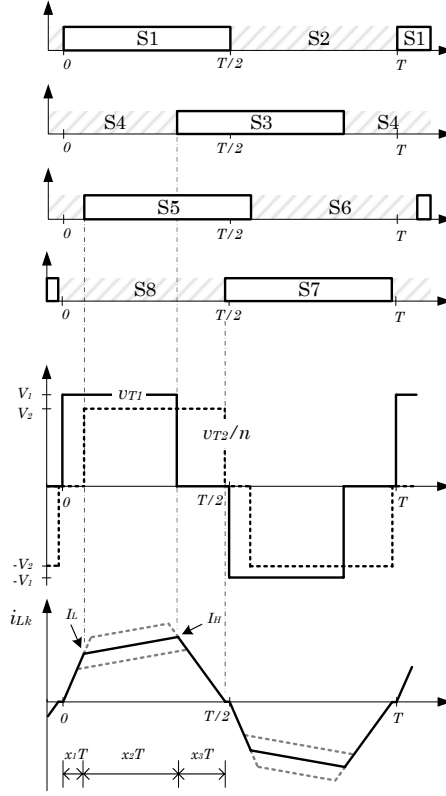
Figure 4.12: Transformer current (i_{Lk}) for the first trapezoidal sub-mode DAB modulation

to ensure i_{Lk} fully returns to zero. For the forthcoming mathematical analyses, however, the theoretical value of 0.5 is used.

From the given first sub-mode condition, x_3 is:

$$x_3 = \frac{1}{2} - x_1 - x_2 . \tag{4.15}$$

By combining all equations in (4.14) and (4.15), x_2 is expressed as:

$$x_2 = \frac{1}{2} \frac{V_2}{nV_1} - x_1 \left(1 + \frac{V_2}{nV_1} \right) . \tag{4.16}$$

Returning (4.16) to (4.15) results in:

$$x_3 = \frac{1}{2} - \frac{1}{2} \frac{V_2}{nV_1} + x_1 \frac{V_2}{nV_1} . \tag{4.17}$$

Now, both x_2 and x_3 are given as a function of x_1. Furthermore, if (4.16) and (4.17) are combined with (4.12) and (4.14), the following equation is obtained:

$$-x_1^2\left(V_1+\frac{V_2}{n}+\frac{V_2^2}{n^2V_1}\right)+x_1\frac{V_2^2}{n^2V_1}+\frac{1}{4}\frac{V_2}{n}\left(1-\frac{V_2}{nV_1}\right)-\frac{I_{2(av)}L_k}{T}=0\ . \tag{4.18}$$

Solving (4.18) in terms of x_1 and taking into account that x_1 has to be positive and real, $I_{2(av)}$ in the I trapezoidal sub-mode has to fulfil conditions (4.19), for its minimum, and (4.20), for its maximum achievable value:

$$I_{2(av)}>\frac{T}{4L_k}V_1\frac{V_2}{nV_1}\left(1-\frac{V_2}{nV_1}\right), \tag{4.19}$$

$$I_{2(av)}\le\frac{T}{4L_k}\frac{V_2}{nV_1}\frac{V_1}{1+\dfrac{V_2}{nV_1}+\left(\dfrac{V_2}{nV_1}\right)^2}\ . \tag{4.20}$$

Figure 4.13 depicts the trapezoidal I sub-mode operating area, where the output voltage is normalized to the input voltage and transformer turn ratio (n), while the output current is normalized to the input voltage, n, switching period and $1/L_k$.
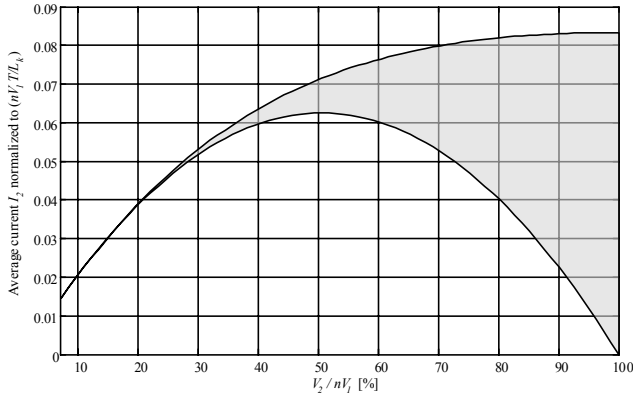
Figure 4.13: Operating area of the first trapezoidal sub-mode DAB modulation

4.3.2.2 Second trapezoidal sub-mode (II sub-mode)

The second trapezoidal sub-mode is necessary to cover low DAB output current (I_2) values as V_2 decreases.

To preserve the ZVS, the second sub-mode maintains I_L constant, and therefore, x_1, while all other parameters are varying, see Figure 4.14. The fixed I_L value ensures enough of the energy in the leakage inductance to provide the ZVS. Note that the conditions $I_L\le I_H$ and $x_1+x_2+x_3\le 0.5$ always have to be fulfilled. As a result, the rms-to-average current ratio increases as the power decreases. However, soft switching (ZVS) can be maintained in a wide range, which is more important in circuits with high switching turn-on losses and/or large snubber capacitors used to decrease turn-off losses.
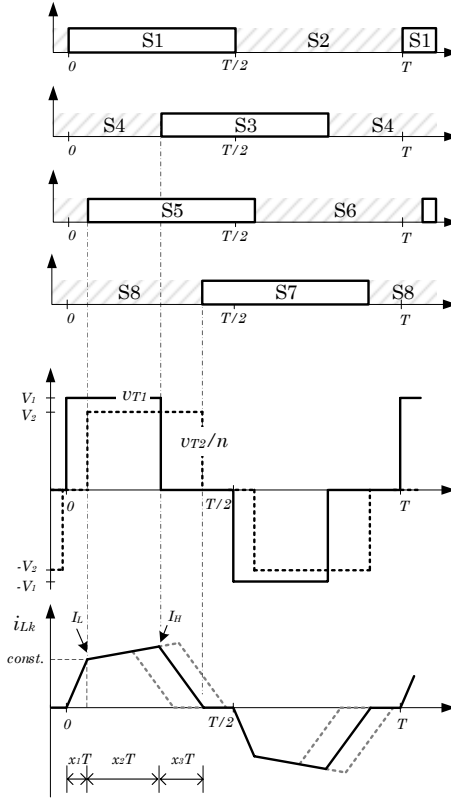
Figure 4.14: Transformer current (i_{Lk}) for the second trapezoidal sub-mode DAB modulation

The ZVS threshold current (I_L) is set by x_1 from (4.14). From the second and third expressions in (4.14), x_3 can be found as:

$$x_3 = x_2 \left(\frac{nV_1}{V_2} - 1 \right) + \frac{nI_L L_k}{V_2 T} \,. \tag{4.21}$$

Combining expressions for I_H from the second equations in (4.14) and (4.13), the quadratic equation for x_2 is provided:

$$x_2^2 \frac{nV_1}{V_2} \frac{T\left(V_1 - \frac{V_2}{n}\right)}{L_k} + x_2 \frac{2nV_1}{V_2} I_L + \frac{nV_1}{V_2} x_1 I_L - I_{2(av)} = 0 \,. \tag{4.22}$$

The constraint of strictly positive values of x_2 gives a minimum feasible value of $I_{2(av)}$ for the trapezoidal II sub-mode:

$$I_{2(av)} > \frac{L_k}{TV_1} \frac{nV_1}{V_2} I_L^2 \,. \tag{4.23}$$

The trapezoidal II sub-mode maximum achievable $I_{2(av)}$ is provided when $x_1+x_2+x_3 = 0.5$, thus, the DAB output current upper limit can be calculated using a rearranged (4.18).

Figure 4.15 depicts the trapezoidal II sub-mode operating area, where the same normalizations are applied as in Figure 4.13.
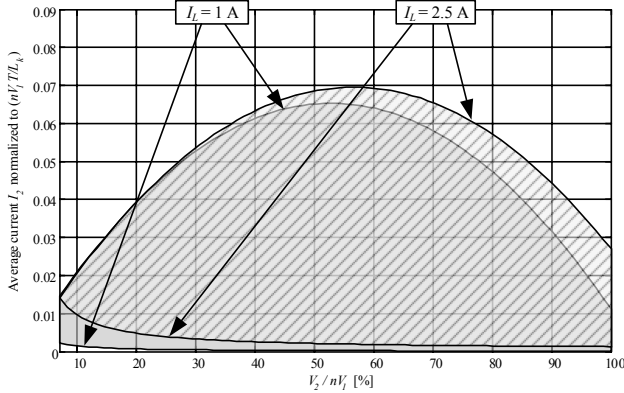
Figure 4.15: Operating area of the second trapezoidal sub-mode DAB modulation. Given are two cases for different I_L values, required for the ZVS

4.3.3 Triangular DAB modulation

The triangular modulation mode can be seen as a special case of the second trapezoidal sub-mode, where x_2 is equal to zero. Thus, the transformer current has a triangular shape [86], see Figure 4.16. Therefore, $x_1+x_3 \le 0.5$ has to be fulfilled. Furthermore, only x_1 and x_3 are changing with the power requirement. A high peak of the current I_L ensures that the snubber capacitance in combination with the switch output capacitance is discharged as much as possible to achieve low switching losses. The triangular modulation also comprises both the ZVS and ZCS.

Taking into account that $x_2 = 0$ and by equating (4.12) and (4.13), one can write:

$$x_3 = \frac{nV_1}{V_2} x_1 \,. \tag{4.24}$$

Furthermore, by combining (4.12) and (4.14), the following expression (4.25) is derived:

$$x_1 = \sqrt{\frac{I_{2(av)} V_2 L_k}{nV_1^2 T}} \,. \tag{4.25}$$

The maximum value of $I_{2(av)}$ is delivered when $x_1+x_3 = 0.5$; therefore, the triangular control mode DAB output current range is determined using:
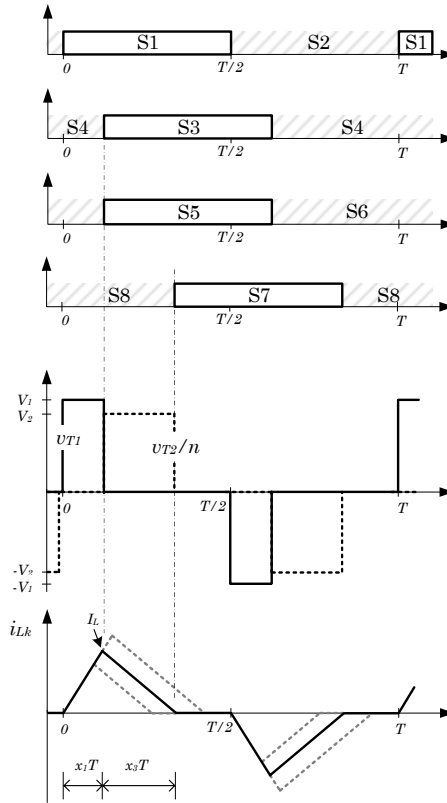
Figure 4.16: Transformer current (i_{Lk}) for the triangular mode DAB modulation

$$I_{2(\text{av})} \leq \frac{T}{4L_k} \frac{V_2}{nV_1} \frac{V_1}{\left(1+\dfrac{V_2}{nV_1}\right)^2} \, . \tag{4.26}$$

Figure 4.17 depicts the triangular control mode operating area (among others), with previously used normalizations. Note that the triangular modulation can deliver low currents, while the ZVS cannot be maintained over the entire range, since I_L can be too low.

To summarize, Figure 4.18 shows operating areas of all three investigated DAB control modes to compare them. Note that there is a slight overlap between I and II trapezoidal sub-modes. The modulation technique that should be used in this overlap area is determined in the next section of the thesis. However, the trapezoidal I sub-mode delivers approximately 28% higher maximum current than the other two modes. Furthermore, the triangular mode covers most of the deliverable power area, however, because of its current shape and indirect power transfer characteristic [86], it should be less efficient than the

trapezoidal control mode in general. Nevertheless, extremely low voltages and currents can only be covered by the triangular DAB control mode, in this case.
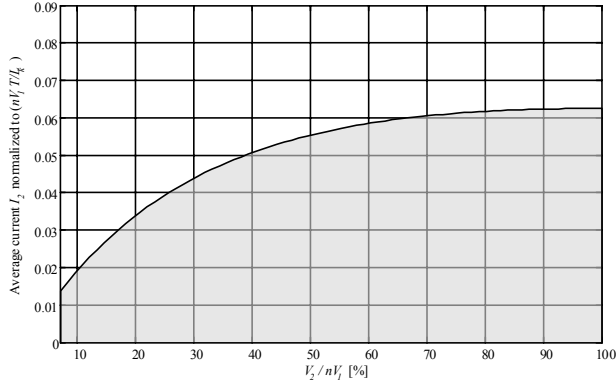
Figure 4.17: Operating area of the triangular DAB modulation
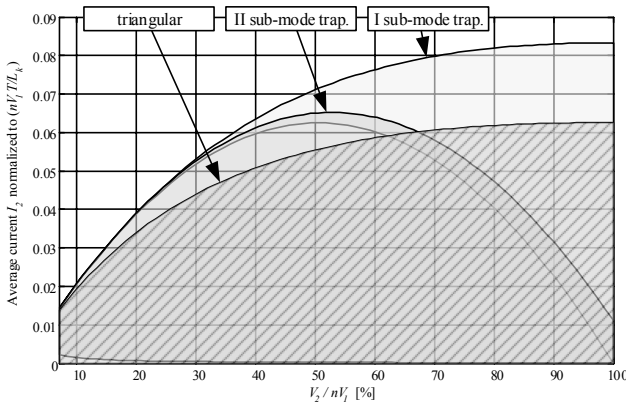
Figure 4.18: Operating areas of all three investigated DAB modulation modes. The II trapezoidal sub-mode is presented for $I_L = 1$ A

4.4 VARIABLE FREQUENCY AND OPTIMAL DUAL ACTIVE BRIDGE MODULATION METHOD

As it has been shown, the DAB can employ many modulation techniques that provide a wide range of freedom for the current control and efficiency manipulations. However, if it is necessary to keep a constant (high) current level at the output while the output voltage is changing in almost its full range, constant frequency methods are not the preferred solutions for some modulation methods because of high rms to average current ratios ($I_{(rms)}/I_{(av)}$) in the circuit. Hence, for a very wide output voltage range and constant,

maximum output current, it is preferred to decrease the switching frequency, as is the case with trapezoidal and triangular modulations.

Because of the presented trapezoidal and triangular modulation limitations, the following work was carried out to investigate possible solutions and increase operation areas. The phase-shift modulation is analysed efficiency-wise and compared after other modulations become suitable for the required power range.

4.4.1 Extended modulation mode operating areas

In the previous section, the operation range of the average DAB output current I_2 is presented for different modulation modes. To extend the operation area, the parameter T (switching period) can be varied easily. Nonetheless, the maximum value of T determines the size of filter components (capacitors). However, the size of the transformer is determined with a minimum T, which significantly reduces the converter volume. In the case of trapezoidal modulation, this follows from the fact that with V_2 decreases, x_3 and T increase, but x_1 and x_2 decrease more, thus, resulting in less volts-seconds over the transformer winding. The same is valid for the triangular modulation. Figure 4.19 presents the calculated transformer fluxes for individual modulations, as well as the corresponding switching frequencies, for the case of the modelled converter with parameters listed in Table 6.2. Note that the triangular constant frequency modulation is also included in Figure 4.19 for comparison purposes.

Since the DEAP generator requires a wide variety of voltage and current coupled with the high efficiency, the switching period must be changed to follow the output voltage level. The switching frequency should be adapted to the output current if conduction losses are the dominant factor. Since IGBT switches (Infineon–IKW40N120H3 [87]) were employed for the first setup, the frequency was not changed for different current levels, as these switches have significant switching losses. Therefore, the increase of the switching frequency resulting in a decrease of the converter output current would affect the efficiency at low power levels.

Figure 4.20 presents the results of the variable frequency DAB modulation method used to extend the operating areas of the investigated modulation techniques. The switching frequency is changed only for the varying V_2 levels, while the output current I_2 is kept constant and maximum for the calculation of the frequency. In this way, it is ensured that the maximum current can be delivered from each control mode. Switching periods are calculated using (4.20) and (4.26), from which it is possible to express T, while I_2 is set to desired maximum value. However, in this case, T is set as a limiting factor and its minimum value defines the maximum average I_2.

The first and second trapezoidal sub-modes use the same calculation for the switching period. This follows from (4.18), which describes both sub-modes for the case when $x_1+x_2+x_3=0.5$ (maximum output current delivery) and mentions the case where the

switching period changes only with V_2. Again, there is a slight overlap of the operating areas in Figure 4.20 between I and II sub-modes.

On its own, the variable frequency triangular DAB control mode is capable of delivering the whole required voltage-current range (see Figure 4.20), but its maximum current capability is lower. Therefore, it overlaps all trapezoidal sub-modes' operating areas. This makes the triangular mode ideal for implementation in the converter control system, since the control algorithm would be simple. However, nowadays, with the rapid development of microcontrollers and FPGAs, processing power becomes more affordable. Hence, a more complex control is usually easily justified.
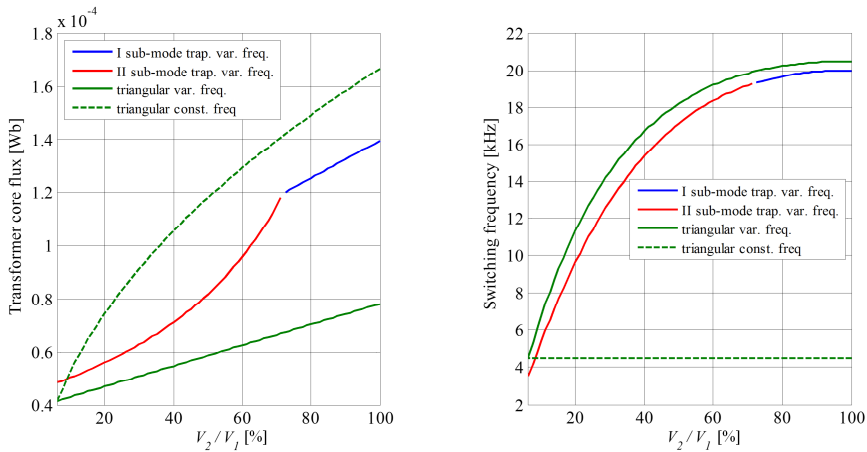
Figure 4.19: Transformer flux (left) and corresponding frequency (right) of the modelled DAB module
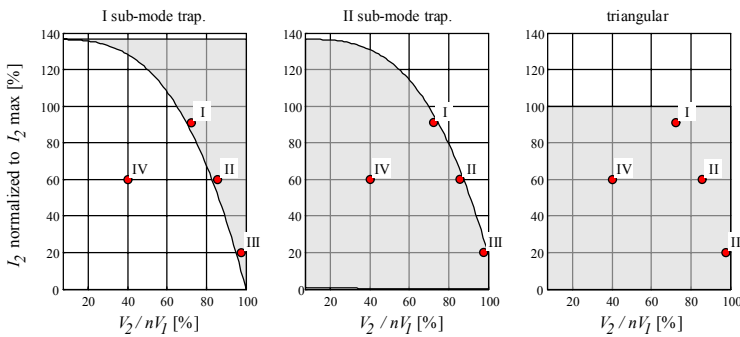
Figure 4.20: Operating areas of all three investigated DAB modulation modes when T is changed with V_2 varying. The II trapezoidal sub-mode is presented for $I_L = 0.2 \cdot I_{2(max)}$. The average of current I_2 is normalized to the maximum required output current $(I_{2(max)})$. Four chosen operating points are marked on each graph

4.4.2 Loss estimation

Loss modelling is carried out to provide preliminary efficiency results and for comparison purposes. Assuming that modules are the same and operated by the same control signals, the total efficiency of the converter is equal to the efficiency of a single module.

Modelled power losses of the converter module consist of: conduction losses of switches, switching losses, transformer losses and power given by auxiliary power supplies for electronics. Loss modelling is done for the steady state of the converter.

It is important to state that for a more precise loss calculation, several modifications were made to the loss modelling method from Chapter 3 of this thesis. Now, transformer ferrite core losses include an additional temperature scaling coefficient, as the losses are up to 3 times higher for 30 °C than for 100 °C.

Losses because of the ZCS exist and are usually calculated as the energy stored in the switch output equivalent capacitance. This energy is dissipated during the turn-on transition on the switch's body, while the switch output voltage decreases. However, this is not the only source of loss taken into consideration during the ZCS. Since modulation is calculated based on a lossless circuit model, it is necessary to account for some mismatch between the calculated and actual transformer current signals. The mismatch occurs due to voltage drops over different conductive components in the circuit, thus, the transformer current slopes are different than what are calculated. The effect can be explained using Figure 4.21. The focus is on the first DAB leg, i.e., switches $S1$ and $S2$, where the ZCS turn-off and turn-on transitions should occur. Instead in zero current, the transition occurs in the current different for ΔI_{ZVS}, as the actual current slope is larger due to the additional voltage seen
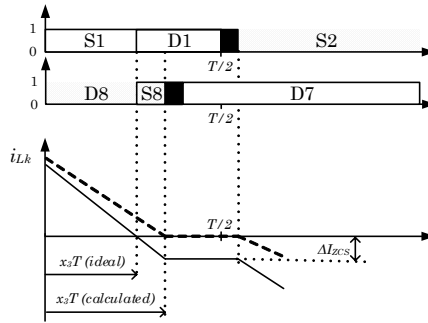
Figure 4.21: Transformer current at the ZCS because of ideal and actual modulation parameter mismatches

by the leakage inductor. This additional voltage is caused by resistive components carrying the current, including switches and transformer windings. The ΔI_{ZVS} is very small, approximately 0.5 A, which in combination with the leakage inductance is insufficient to provide the switch output capacitance discharge, thus, the ZVS turn-on. Now, since the current is not zero, the diode $D1$ is taking over the whole current. This is feasible, as

previously, the switch *S1* was conducting; therefore, almost any current can make the diode be forward-biased. Furthermore, during the switch dead-time, the diode still conducts the current, and after, the dead-time switch *S2* receives the gate signal to turn on. *S2* has to take over the current from the diode *D1* before it is actually turned on, including the diode reverse recovery charge. The reverse recovery charge mainly depends on the diode forward current, current slope, temperature and the diode type. Even if the current is very low, the reverse recovery charge exists until charges in the junction are depleted.

The same zero current mismatch is happening with the last DAB leg (*S7* and *S8*), but there are no additional losses because of diode reverse recovery, as the diode *D7* starts to conduct after *S8* is turned off.

Table 6.2 gives the overview of parameters of the modelled DAB converter module. Figure 4.22 presents the calculated losses of the DAB module in four selected points (see Figure 4.20), chosen for comparison purposes, in the overlapping operating area of trapezoidal and triangular modulation, all within the required DAB power range.

From the calculated losses for the first point, it can be seen that the II trapezoidal sub-mode provides the lowest losses. The same can be observed for the second, third and fourth point. The I sub-mode and the II sub-mode have similar switching losses in the overlap area, even though the I sub-mode does not operate with ZVS inside the overlap. However, the transformer (core) losses are the main difference, in favour of the II sub-mode. The triangular mode always has the highest losses when compared with the trapezoidal modulation. The main reason for this is the triangular current shape. Therefore, a very high
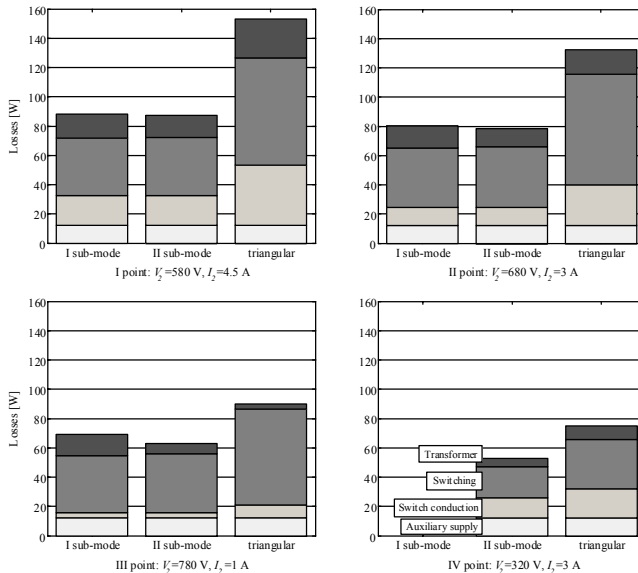
Figure 4.22: Calculated DAB loss distribution for four selected operating points at the operating area overlap. $V_1 = 800$ V and $L_k = 465$ µH

i_{Lk} current peak occurs, and an indirect power transfer characteristic is in process. At every current peak, four switching transitions occur. Additionally, the triangular current shape is undesirable for the conduction losses as it produces high rms-to-average current ratio value. The calculated efficiency surfaces for both trapezoidal sub-modes and triangular modulation are given in Figure 4.23.

4.4.3 Optimal dual active bridge modulation method

To deliver the optimized efficiency of the DAB and the dc-dc multilevel converter as a whole, a comparison of the represented modulation is carried out.

For the trapezoidal and the triangular modulations, a combination is required, since the trapezoidal cannot operate standalone, while the triangular has a very low efficiency overall. From the analysis of those modulation modes, for the given DAB converter, particularly the losses, a definitive operating area for each of the modes is obtained. Figure 4.24 depicts the entire domain of the required voltage-current range for the DEAP generator and the various modulation modes and their operating areas. The phase-shifted is excluded from this graph as it can operate standalone and is compared in the next step.

Using the calculated losses and limitations of each DAB modulation mode, a new modulation method is provided, which is a hybrid modulation. Three areas of operation are distinguished for the entire voltage and current ranges: I sub-mode, II sub-mode trapezoidal and triangular. Furthermore, the hybrid modulation method ensures that the efficiency is high at any operating point, therefore resulting in less losses during the energy harvesting cycles. The calculated peak efficiency using IGBT switches is 97.1%.
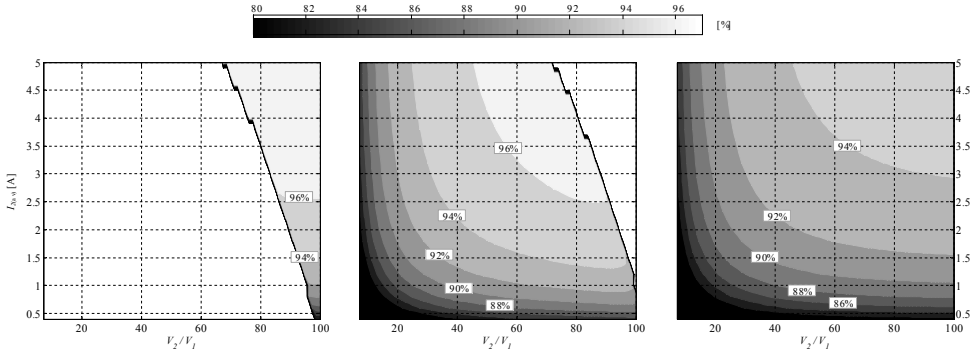
Figure 4.23: Calculated efficiency surfaces for three variable frequency DAB modulations: I sub-mode trapezoidal, II sub-mode trapezoidal and triangular variable frequency modulation

Furthermore, the efficiency surfaces of the hybrid variable frequency and phase-shift DAB modulation are presented in Figure 4.25 for the single DAB module. Note that the hybrid modulation manages to keep the efficiency surface quite flat, while phase-shift modulation has a large efficiency drop with the power.
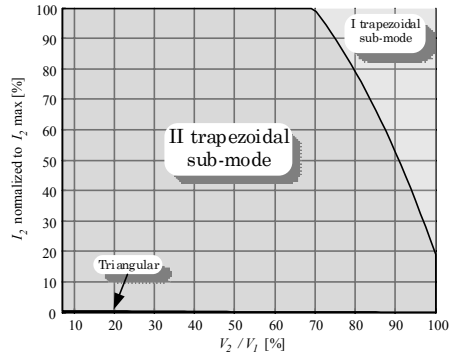
Figure 4.24: Definitive modulation mode operating areas of the modelled DAB module with variable frequency – hybrid modulation. Only the required operating area is shown

Since both modulation methods require optimization of the leakage inductance to deliver low losses, Figure 4.26 shows how the IPOS converter efficiency during the harvesting cycle is changing with the transformer leakage inductance variation applied on the 6 s time period and 0.36 capacitance ratio sea wave conditions. The best results are provided for the hybrid variable frequency modulation, however, just slightly better. Additionally, the cycle efficiency of the hybrid modulation does not have high variations with the leakage inductance, while the phase-shift drops rapidly with the leakage. The reason behind that large efficiency drop is the loss of the ZVS, as the phase-shift modulation has a very narrow ZVS operation range. Only large leakage inductances could help the phase-shift modulation to maintain the ZVS, however, this causes higher conduction losses because of the high transformer rms current. Note that if both modulations are applied to the same DAB module (therefore, the leakage inductance is fixed), the hybrid modulation would provide a much larger cycle efficiency (see Figure 4.27); for example, for $L_k = 500$ µH, the hybrid cycle efficiency is for 4.3% larger, which is a substantial difference. In the Figure 4.26, the calculated converter efficiency during the harvesting cycle for the CM converter is also presented. It maintains almost a constant value of the efficiency for different leakage inductances, however, the overall value is lower than for the IPOS converter under phase-shift or hybrid modulation, as expected.

4.5 CONCLUSIONS

In this chapter, firstly, the basic operation principle of the DAB circuit is presented. Furthermore, benefits of the DAB over the dual active half-bridge and the diode-clamped DAB are explained. The basic DAB does not have to process a two-times higher current like other two DAB variations and provides high redundancy. Therefore, the DAB is selected for further investigation.

Since in Chapter 3 the investigation results in the cascaded multilevel converter topology, the proposed modification is made on the CM's module to increase efficiency. The half-bridge is removed at the output, thus, resulting in a single-stage module and input-parallel-output-series connection of DAB modules. However, with the applied modification, the requirements for the DAB are changed in a way that the operating output voltage range is very wide, which is not common.

Next, the analysis provides an overview of the suitable modulation modes commonly used with DABs. The variable frequency operation is proposed for the DAB modules to provide a wide variety of voltage and current at its output. Moreover, the analysis deals with the limitations and losses of each modulation mode and, finally, presents a hybrid DAB modulation method, which is optimized for efficiency. Additionally, a comparison between hybrid and phase-shift modulation is performed to directly demonstrate their efficiency impact on the harvesting cycle losses. Overall, the hybrid variable frequency DAB modulation shows slightly better results for the selected sea wave conditions when appropriate (optimized) leakage inductances are used. On the other side, if the same transformer leakage inductance is employed, the hybrid modulation demonstrates above 4% higher efficiency than the phase-shift modulation.

Within the hybrid modulation, the analysed first trapezoidal sub-mode performs the best at high voltage-current levels, although the second trapezoidal sub-mode covers most of the operating power range while delivering the lowest losses. The variable frequency triangular modulation mode covers the entire power range without limitations but delivers higher losses than the other two investigated modes. Therefore, the triangular mode should only operate at low power levels, which are not covered by the trapezoidal sub-modes in the hybrid modulation.
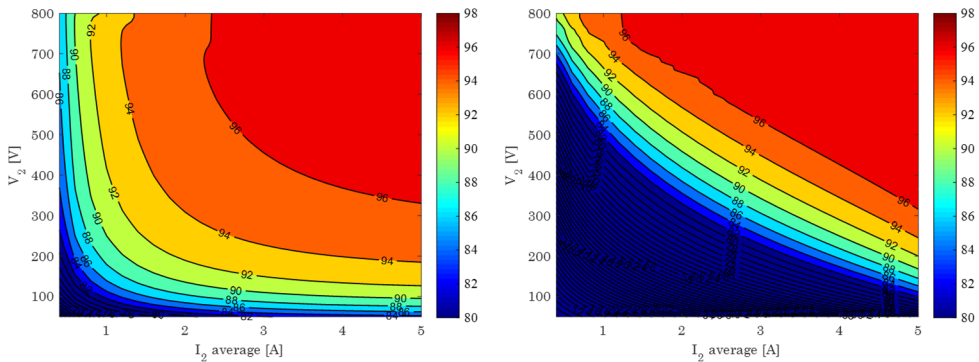
Figure 4.25: Hybrid variable frequency (left) and phase-shift (right) DAB modulation efficiency curves for the single DAB module and the largest allowed transformer leakage inductance necessary to provide 6 A to the DEAP generator
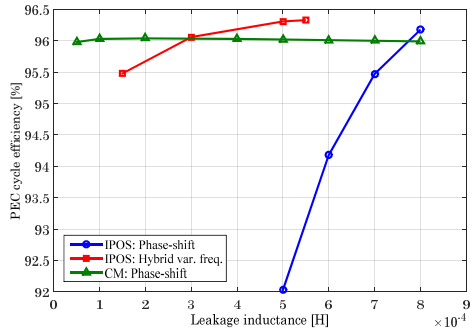
Figure 4.26: Converter cycle efficiencies for different DAB modulation methods and transformer leakage inductances, sea wave conditions: 6 s period and 0.35 capacitance ratio
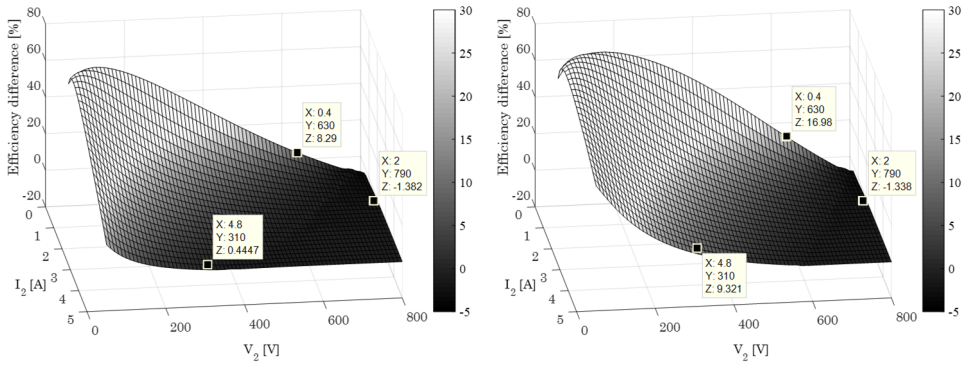
Figure 4.27: Efficiency difference surfaces: Hybrid minus Phase-shift modulation point efficiency. Both modulations for their maximum allowed leakage inductance (left) and both modulations for the same 500 µH leakage inductance (right)

Chapter 5

Individual module control method for an IPOS-connected converter

5.1 INTRODUCTION

Chapter 4 of this thesis deals with the proposed single DAB module modulation techniques to provide overall low losses in an IPOS-connected PEC during DEAP energy harvesting. Now, when the best modulation is selected for modules, further investigation focuses on additional possibilities for efficiency improvements, not at the individual module level but for the entire multilevel converter. The following study provides optimal control of the IPOS-connected converter modules to minimize losses. The previously estimated DAB module efficiency curves are used for the overall converter efficiency calculation, as the internal DAB behavioural is not discussed.

Since large voltage and current variations are required, different methods for delivering power from each individual module have to be investigated to provide lower overall converter losses, and therefore, a higher energy yield during wave energy harvesting. However, it is shown that the IPOS-connected converter mostly operates with pulse current and a wide voltage range, and therefore, the investigation results of the module control methods are limited to the constant DEAP generator current mode. Nevertheless, the conclusions are applicable to any system, as well as when current varies.

The main issues addressed in this chapter are:

- Investigation of module control methods;
- Power converter efficiency improvements by optimal control.

5.2 MODULE CONTROL APPROACHES

Three different module control modes (or methods) of the IPOS-connected converter are investigated and later compared in terms of total PEC efficiency. These are: all modules active, step module activation and variable module activation control modes.

5.2.1 All modules active control

In the all modules active (AMA) control method, the same control signals are employed to each of the modules, thus, each module provides the same output power (voltage and current), see Figure 5.1. It is advisable to use the phase-shift between each individual module PWM signals (interleaving) to minimize the overall voltage and current ripples. The phase-shift is accomplished by employing synchronization between the dedicated PWM module signals.
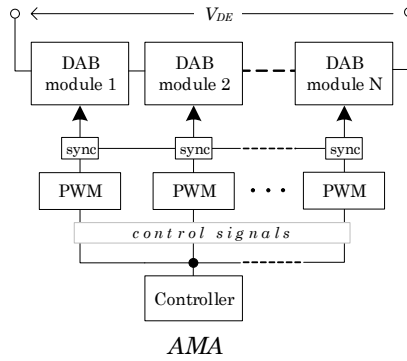
Figure 5.1: Control signals for the all modules active control method applied to a PEC consisting of three modules

Since the IPOS-connected modular converter has modules connected in a series at the DEAP generator side, each module provides the Nth part of the entire DEAP generator voltage when the AMA control is applied, where N is the number of modules. The output current (the DEAP generator current) is, naturally, the same for each module, and any of the module controls when the converter operates in steady state. Figure 5.2 presents how the DEAP generator voltage is distributed over the individual modules for the AMA control applied to the IPOS-connected converter consisting of just three modules. The number of active modules (N_{am}) is equal to N for the case of AMA control.

5.2.2 Step module activation control

The step module activation (SMA) control method is an approach where modules of the modular converter are individually controlled, see Figure 5.3. The modules are increasing the power (voltage) at the output, one by one, until the maximum rated power transfer is reached. The same interleaving is applied as in the AMA control for ripple minimization.
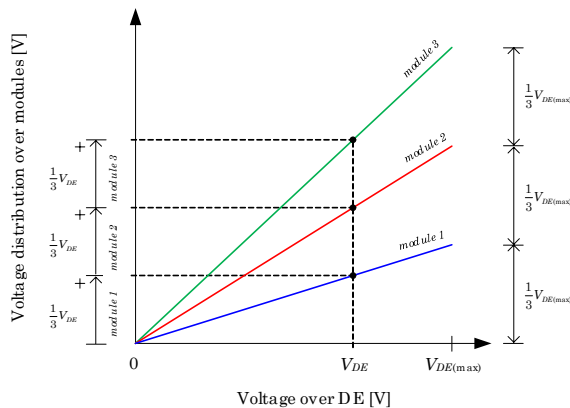
Figure 5.2: Module output voltage distribution for the AMA control method

SMA
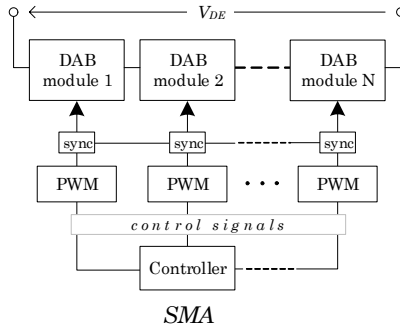
Figure 5.3: Control signals for the step module activation control method applied to a PEC consisting of three modules

Figure 5.4 shows how the DEAP generator voltage is distributed over the modules when the SMA control is used. The same three-module sample IPOS-connected converter is employed as in the AMA module control method, $N = 3$. Note that for the maximum DEAP generator voltage all modules equally share the DEAP generator voltage, the same as for the AMA control. However, the difference in module operation is at voltages lower than $V_{DE(\max)}$. For the V_{DE} example given in Figure 5.4, only two modules are operating, while third module is bypassed (shorted). Additionally, the first module provides the maximum rated voltage, whereas the second module delivers the rest of the voltage to reach V_{DE}. The number of active modules (N_{am}) is equal to:

$$N_{am} = \left\lceil \frac{V_{DE}}{V_{DE(\max)}/N} \right\rceil , \tag{5.1}$$

where the given notation corresponds to the ceiling function, i.e., the smallest following integer defined with the general expression:

$$\lceil x \rceil = \min\{n \in \mathbb{Z} \,|\, n \geq x\} . \tag{5.2}$$

5.2.3   Variable module activation control

The variable module activation (VMA) control method uses the approach where modules are individually controlled, as it is done for the SMA control, see Figure 5.3. However, the VMA takes into account the efficiency behavioural data of the modules, and therefore, can provide better efficiency performance.

The VMA operation principle can be described as follows: If demand for power is increasing from zero, the modules follow it, one by one, until each reaches a power point where the efficiency is the highest. Inactive modules are bypassed (in the case of module in series connection at the output side) or inactive (in case of modules in parallel connection at the output side). When all modules are at their maximum efficiency points (MEPs, see Figure 5.5) and the power is increasing further, the modules increase their output power, one by
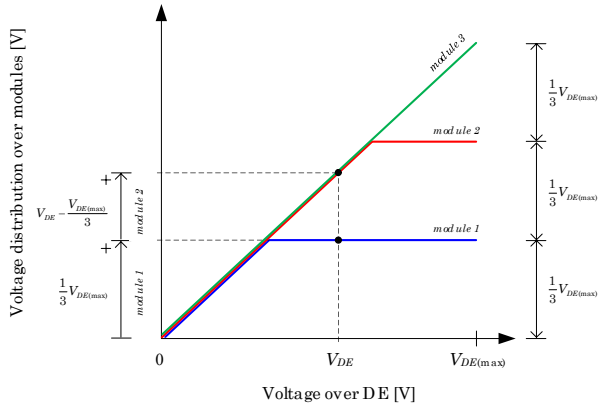
Figure 5.4: Module output voltage distribution for the SMA control method

one, until all modules reach their maximum power point. If the power decreases from the point of maximum efficiency, the modules decrease power, one by one, until they are bypassed. During the bypassed period the output DAB capacitor is shorted by turning on switches connected in parallel with the output capacitor, and if the module is inactive, all switches are turned off.

Figure 5.6 presents the DEAP generator voltage distribution over each module when the VMA control is utilized. The same as before, the given example is for three modules of the IPOS-connected converter, while the power variation is translated into the output voltage variation as the assumed output current level is constant. Note that the voltage at the maximum efficiency point, V_{MEP}, is used for the determination of the modules' output voltages in the control process. Therefore, the V_{MEP} data values have to be known (usually from the measurement) and built into the converter control algorithm. Additionally, if $V_{MEP} = V_{DE(\max)}/3$, then the VMA actually operates as the SMA module control. The number of active modules (N_{am}) is equal to:
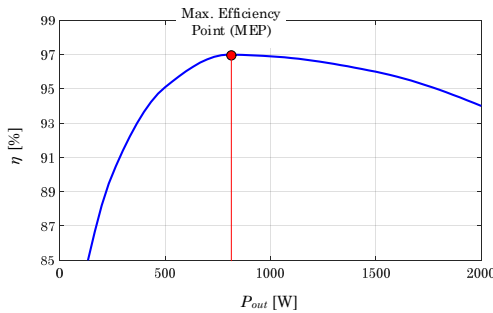
Figure 5.5: Typical efficiency curve example of the electrical power converter module. The power and efficiency levels are arbitrary

$$N_{am} = \begin{cases} \left\lceil \dfrac{V_{DE}}{V_{MEP}} \right\rceil, & V_{DE} \leq N V_{MEP} \\ N, & V_{DE} > N V_{MEP} \end{cases} . \tag{5.3}$$
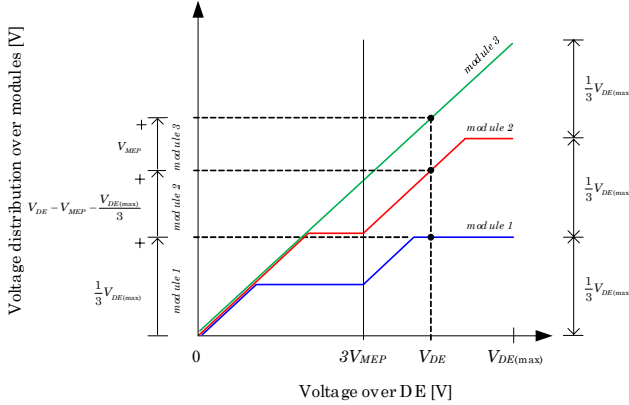
Figure 5.6: Module output voltage distribution for the VMA control method

5.3 SUGGESTED OPTIMIZED MODULE CONTROL METHOD

As shown in previous sections, the different control strategies that can be employed for module control, in a modular IPOS-connected converter, reflect the proposed topology versatility. In the following analysis, a simple efficiency calculation is made for three modules connected in series at the output side and with the same efficiency characteristic, as given in Figure 5.5. The goal is to detect the optimized module control method, from the overall PEC efficiency point of view, while dealing with the generic module efficiency characteristic. Furthermore, the resulting module control method is applied on the proposed IPOS converter for DEAP energy harvesting, and the outcome is presented.

5.3.1 Efficiency curve estimation

Figure 5.5 presents the example efficiency curve of a DAB module. It is assumed that one of the output parameters (e.g., current) is kept constant, while the other one (e.g., voltage) is changing, thus, varying the output power. This is convenient for the case of a series connection of modules, as in the IPOS-connected converter, and for the application pulse current requirement.

The efficiency curves are obtained by applying the mentioned AMA, SMA and VMA module control modes on the given converter system with three modules. The VMA control mode consists of six stages, in the case of the converter comprised of three modules (see Figure 5.7):

- I stage: only one module is active, while the other two are bypassed;

- II stage: two modules are employed of which the first is at its MEP, and the second varies its output power. The third module is bypassed;

- III stage: two modules are in their MEPs, and the third module is active. At the end of part III, the maximum efficiency point is reached for the overall converter system;

- IV stage: two modules are at their MEP, and the third module varies its output power above the MEP;

- V stage: one module is at its MEP, one delivers its maximum rated power, and the last module varies its power above the MEP;

- VI stage: two modules deliver their maximum rated power, and third varies its power above the MEP.

The SMA module control mode consists of three stages. These stages behave in the same manner as the first three stages given for the VMA control, with one important difference, the MEP is not considered, but each module pushes the power to its maximum, see Figure 5.8.
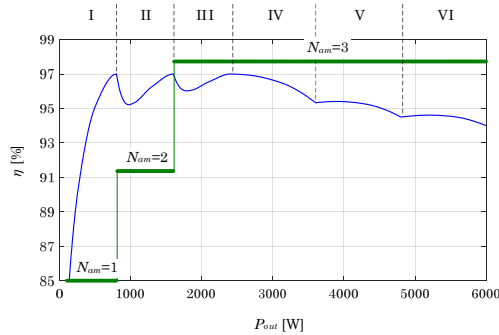
Figure 5.7: Calculated efficiency curve for the VMA module control mode of the given converter system consisting of three modules. Marked are parts of the VMA method for different operation stages
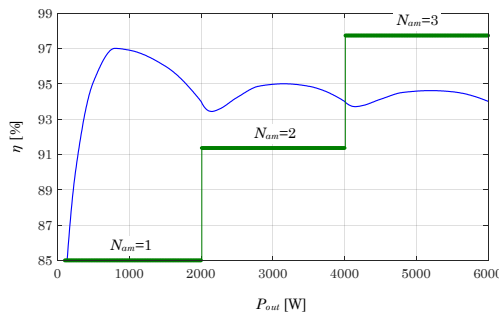
Figure 5.8: Calculated efficiency curve for the SMA module control mode of the given converter system consisting of three modules

Since the AMA control mode dictates the same operation of each module, the overall converter efficiency curve shape is the same as that of the single module, however, it is spread over a larger power range. Figure 5.9 shows all three module control modes on a single graph to compare the calculated overall efficiency curves. As it can be seen, the AMA provides the highest efficiency at the operational point above 3·MEP. However, at the operation points below 3·MEP, the VMA shows better overall results when compared with both the AMA and SMA. Furthermore, the transition from the VMA to AMA, and vice versa, is suitable due to the voltage (power) match at the transition point – 3·MEP.
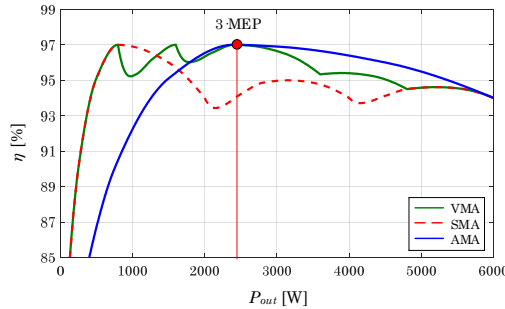
Figure 5.9: Calculated efficiency curves for all three module control modes applied on the converter system consisting of three modules

5.3.2   Hybrid module control method

It can be seen from Figure 5.9 that the VMA mode provides a higher efficiency for the power levels below the 3·MEP. Above the maximum efficiency point, the AMA module control mode delivers better results. Therefore, the best module control approach would be a combination of AMA and VMA modes – a hybrid module control method, as shown in Figure 5.10. For positive $\Delta\eta/\Delta P_{out}$, the VMA control should be used, while for negative $\Delta\eta/\Delta P_{out}$ the AMA control should be employed to increase overall converter efficiency, as given in:

$$Hybrid\ module\ control\ method\ = \begin{cases} \dfrac{\Delta\eta}{\Delta P_{out}} \geq 0,\ \text{VMA} \\[2mm] \dfrac{\Delta\eta}{\Delta P_{out}} < 0,\ \text{AMA}. \end{cases} \tag{5.4}$$

Figure 5.11 depicts the modules' output voltage distribution for arbitrary V_{DE} values and a three-module IPOS-connected converter with the applied hybrid module control method as the optimal solution. The VMA control mode is utilized at the low DEAP generator voltage levels, below the V_{MEP} voltage point, and the AMA control mode for high voltages over the DEAP generator.
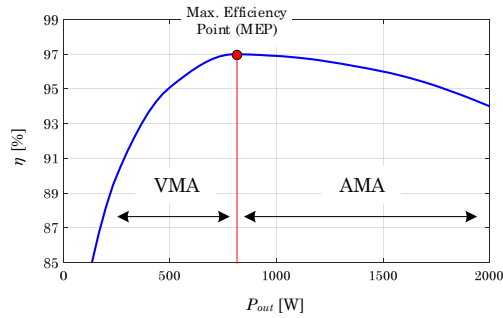
Figure 5.10: Example efficiency curve of the single converter module with marked VMA and AMA control mode domains – the hybrid module control method
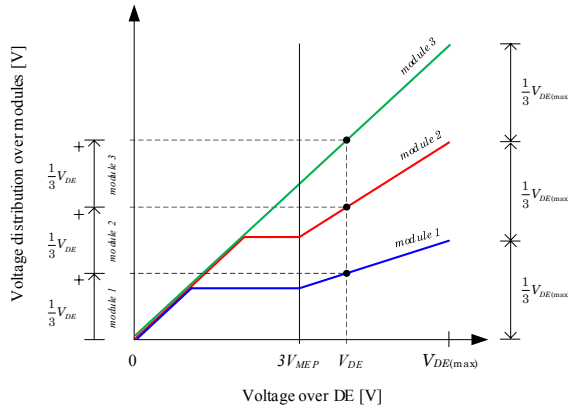
Figure 5.11: Module output voltage distribution for the hybrid module control method

Overall, the hybrid module, or the VMA, control method improves the efficiency at the lower voltage (power) levels, as demonstrated. However, it does not come without additional expenses in some cases. All analyses are performed for the steady-state converter operation to simplify the procedure, yet the DEAP generator requires variable voltage for the harvesting cycles. Since the required DEAP generator voltage slopes are low (10 kV/s at the max.), the steady-state operation approximation is justified for the AMA module control, as each module has to provide 800 V/s max. slope. However, the SMA and VMA demand (800 $\cdot N$) V/s slopes at maximum; this results in a N times higher average current supplied to the module output capacitor, and consequently, a larger power loss for the same power at the module output. The increase of the processed power, within the module, directly depends on the size of the module output filter capacitor, while the module is in the voltage transition operation. Since the capacitance is not taken into account for the basic module control operation analysis, the calculated efficiency curves are an approximation. Moreover, each bypassed module only dissipates power as it doesn't participate in the power transfer while conducting the output current through the bypass circuit. For more accurate

estimations, the additional loss has to be considered for the actual voltage slopes and employed module output filter capacitance, as well as for the bypass circuit.

5.4 EFFICIENCY OF IPOS CONVERTER WITH THE HYBRID MODULE CONTROL

As the module, presented in the Chapter 4 of the thesis, can provide maximum of 800 V at the DEAP generator side, the necessary number of modules to cover the whole 10 kV range is N = 13. Figure 5.12 shows how the number of active modules changes with the variation of the DEAP generator voltage if the SMA module control method is applied.
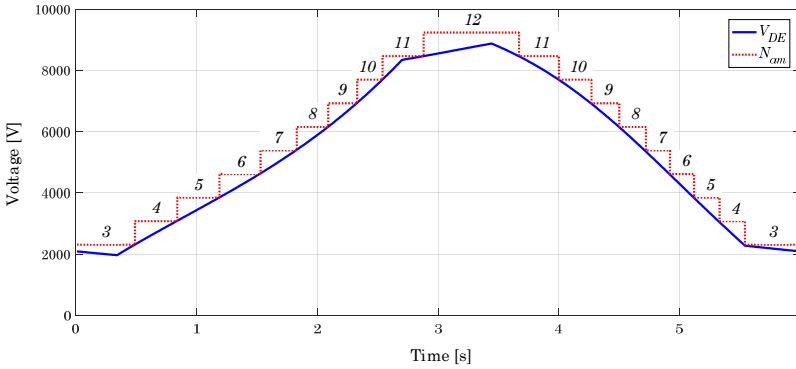
Figure 5.12: Change in the number of active modules with the DEAP generator voltage variation for the SMA module control applied with the full scale IPOS converter

Figure 5.13 presents the calculated efficiency curves of the IPOS converter for different module control methods applied over the full power range during the charging of the DEAP generator. The hybrid modulation is utilized for the DAB modules, as applied on the previously described prototype DAB setup. It can be seen that the efficiency curves have positive $\Delta\eta/\Delta P_{out}$ in the used power range for the AMA control mode. Therefore, the VMA/SMA mode will provide higher efficiencies at low voltage levels compared with the AMA mode, as expected, making the overall efficiency surface flatter. Although the hybrid control method is employed, the modules are kept in the VMA/SMA control mode because of the generally positive $\Delta\eta/\Delta P_{out}$ in the required power range. In the presented case, the VMA and the SMA operate in the same manner, since the MEP is equal to the maximum module power point. The overall efficiency improvement can be detected already at DEAP generator voltages below 6 kV, and for the DEAP generator voltage of 3 kV, the $\Delta\eta$ is approx. 2.5%. However, note that for the DEAP generator current values below 2 A and

(a)   (b)
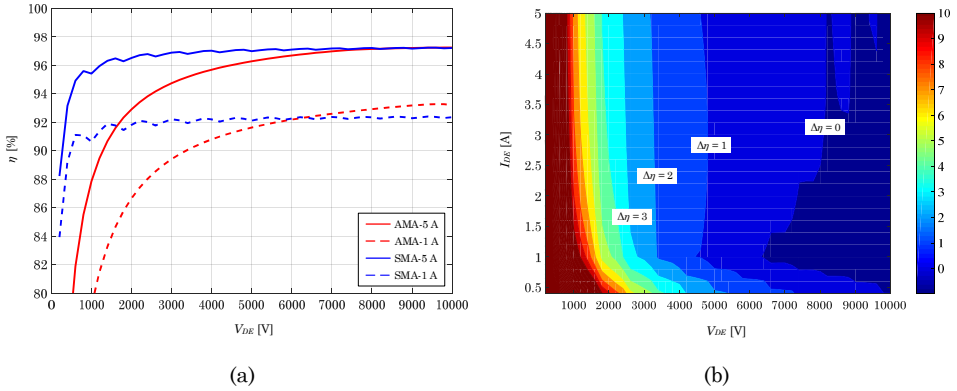
Figure 5.13: Calculated efficiencies of the AMA and VMA/SMA module control methods for different operating points of the IPOS-connected converter ($N = 13$) during the DEAP charging: (a) Efficiency curves for DEAP generator currents of 1 A and 5 A, and (b) the efficiency difference at each operating point (η_{SMA}-η_{AMA}), $V_{BUS} = 800$ V

voltages above 7 kV, the AMA control delivers higher efficiency with a peak difference of 0.9%. Overall, the hybrid (VMA/SMA) module control provides a 96.86% cycle converter efficiency compared with the 96.29% of the AMA control, for a sea wave of 6 s period and 0.35 capacitance ratio. Therefore, the hybrid module control is substantially closer to the calculated peak PEC efficiency of 97.24%.

The utilization of modules to reach higher efficiencies by applying a specific control method is one of the advantages of the modular converter design. This is one of the cases where modular converters demonstrate flexibility and versatility.

5.5   CONCLUSIONS

Since the proposed IPOS multilevel power electronic converter has a modular topology, individual control of the modules can improve efficiency at the lower DEAP generator voltage levels, which is shown in this chapter through the calculated efficiency curves. The performed analysis gives an overview of the three basic module control approaches: all modules active, step module activation and variable module activation control modes.

The proposed individual module control method combines AMA and VMA module control modes, thus, creating a hybrid module control. The hybrid module control delivers 2.5% higher efficiency than the AMA control at one third of the rated voltage and an overall 0.6% higher converter cycle efficiency for the specific wave conditions. The voltage that each module has to deliver is determined based on the module efficiency curves and required output voltage of the IPOS-connected modular multilevel converter.

As each module has a dedicated controller unit, the proposed hybrid efficiency improvement method is achieved without applying any additional hardware to the converter. Therefore,

the suggested hybrid module control method is a benefit that is realized by using the module efficiency characteristic in the control loop of the multilevel converter.

Chapter 6

DAB module design and experimental verification

6.1 INTRODUCTION

In the previous chapters, the loss modelling was performed based on the described method. However, experimental validation is necessary to support the loss model and to provide details about hardware realization. As the high-frequency high-voltage-isolation transformer is the main bottleneck of the proposed IPOS-connected DAB-based multilevel converter, its design and leakage inductance have to fit into the converter requirements.

The main issues addressed in this chapter are:

- Design of the Si IGBT-based DAB single module;
- Efficiency and signal measurements on the realized DAB experimental setup;
- Verification of the calculated efficiencies and signals;
- Implementation of SiC MOSFET switches in the DAB module and achieved efficiency gain.

6.2 SPECIFICATIONS AND COMPONENTS

The goal the DAB test setup is mainly to validate the developed loss model, while volume-efficiency optimization is not considered. The key parameters that determine basic DAB components are provided by the DEAP WEC application, described previously. The input specifications for the DAB module are listed in Table 6.1, while referring to Figure 4.3.

Table 6.1: DAB converter module specifications

Parameter	Value
Power rating	4 kW
Input voltage, V_1	800 V dc
Output voltage, V_2	50 – 800 V
Output current, I_2	± 5 A
Switching frequency, f_{sw}	3.6 – 21 kHz
Transformer turn ratio, N	1
Target leakage inductance, L_k	500 µH

6.2.1 Components

6.2.1.1 Switch

Since the IPOS-connected converter employs a number of DAB modules, while each DAB module comprises eight switches, it is taken that the minimization of the modules' number may be a benefit, from a reliability point of view. However, choosing modules with 6.5 kV switches, for example, to operate at a 4 kV dc blocking voltage may not be a good solution,

since those switches introduce large switching losses. On the other hand, going low with the blocking voltage (the voltage rating of each individual module) may result in a lower reliability of the system but could provide higher efficiency overall.

One of the limitations on the minimum DAB voltage is the voltage overshoot that appears over the switch during the turn-off transition and is caused by the stray inductances in the circuit. The voltage overshoot may remain almost constant for lower DAB voltages, and at a certain point, is larger than the dc DAB voltage. Furthermore, the biggest benefit of using low voltage switching devices is the low switching loss, which can allow for higher switching frequencies, and therefore, minimize the converter volume. However, the main constrain in the IPOS-connected DAB-based converter is the voltage isolation requirement between primary and secondary side of the transformer. The voltage isolation layer has to be thick enough to provide the required isolation barrier and is, generally, independent on the switching frequency. Therefore, a switching frequency point below which the transformer size is practically unchanged can be determined. However, these constraints are not considered for the prototype DAB setup design, but should be taken into account for the DAB module optimization purposes.

The chosen DAB module voltage is set to 800 V, which allows the use of switches rated for a 1.2 kV blocking voltage. Currently on the market, there are a large number of Si based IGBT switches with a 1.2 kV voltage rating, low on-resistance and low switching losses. Moreover, new SiC devices introduce even lower losses than the Si switches and are mostly rated for voltages of 1.2 kV and above. Additionally, at the dc-bus voltage side, the inverter is intended to be employed with the 800 V dc voltage requirement. This makes the choice of the DAB voltage easier, as the 800 V is a good match for 1.2 kV switching devices. On the DEAP generator side, the 10 kV voltage is necessary. However, going for lower voltage rated switching devices is avoided due to possible reliability issues and communication line problems. On the other hand, larger voltage switching devices may not deliver the performance of the 1.2 kV switches.

As mentioned, for the first setup, Si IGBT switches are used, specifically Infineon IKW40N120H3, with built-in soft diodes. These switches are intended for use with high switching frequencies, since they provide very low switching losses. They can handle collector current at a value of 40 A at 100 °C, which is significantly larger than the required application current. The reason for the current overrating is the minimization of conduction losses, as the switching losses should be reduced through the soft switching.

6.2.1.2 Transformer

The transformer test design has to be flexible, like the rest of the DAB setup; therefore, the leakage inductance should be first minimized using proper windings position. Furthermore, if necessary, the additional inductance could be added in series with the transformer leads to fulfil the leakage inductance requirement. The transformer windings are winded one on top of another, as shown in Figure 6.1.
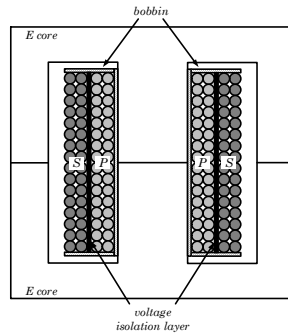
Figure 6.1: Example of the transformer cross-section with windings (P-primary and S-secondary) positioned for minimization of leakage inductance

The voltage isolation provided by the coil former, or bobbin, has to be enough to deal with a dc-bus voltage of 800 V, since the transformer core is grounded to the grounding point of the DAB's primary side (low voltage potential side). For that purpose, an epoxy glass FR4 sheet material can be used, if the bobbin is not the standard shape usually made for the single pair of cores.

To determine the size of the transformer core, a design procedure is followed given in the Appendix. For the core calculation, standard manufactured cores geometries are used, thus, the design procedure results in the four E100/60/28, i.e., two pairs of cores. Since the considered frequencies are in the range of tens of kilohertz, the ferrite materials are investigated, and the Ferroxcube 3C92 is selected due to its high flux density and good thermal stability characteristics. The number of turns per winding is also determined through the design procedure, while the maximum winding area and the maximum flux density are the major constraints. This results in 61 turns per winding allows for use of 2 mm^2 Litz wire that provides a low current density value of 2.5 A/mm^2. Figure 6.2, Figure 6.3 and Figure 6.4 show the bobbin transformer design results. The measured leakage inductance is 75 µH, thus, additional inductance is added to the transformer using an auxiliary inductor of 390 µH.
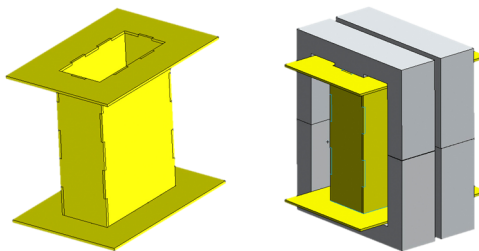
Figure 6.2: Bobbin three-dimensional (3D) model and bobbin core fit
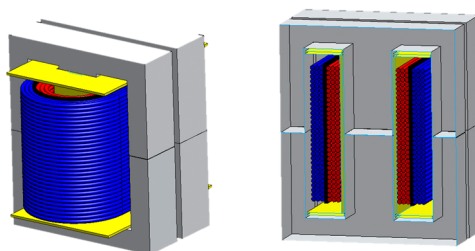
Figure 6.3: 3D model of the designed transformer with the cross-section
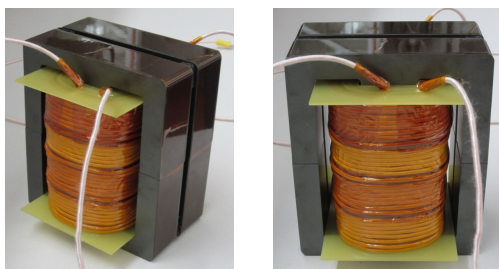
Figure 6.4: Actual transformer for test purposes

6.2.1.3   *Capacitors*

For the filter dc capacitors, a value of 27 µF is selected as the frequency varies down to 3.5 kHz, thus, increasing the voltage ripple over the capacitor significantly. For the selected value at the 50 V output voltage, a ripple of 16 V is observed, that is 30% ripple. However, the size of the input filter capacitance can be significantly lower, since it has the operating voltage of 800 V constantly. The final list of DAB converter module parameters is listed in Table 6.2.

6.3   SPATIAL LAYOUT

The spatial layout of the realized DAB converter is mainly determined with the voltage isolation requirement, besides the cooling method. Since the voltage of approx. 10 kV can appear between the primary and secondary sides of the DAB, the separation of the different voltage potentials has to be solved. However, the toughest task remains to be solved within the transformer, which provides galvanic isolation and power transfer.

Figure 6.5 presents the DAB module two-dimensional model which consists of the primary side connected to V_1 and the secondary side connected to V_2, as well as the isolation transformer. The isolation transformer has windings positioned in such a way that the resulting leakage inductance is low. However, it is possible to further minimize leakage

inductance by creating more layers of the sandwiched windings, but this complicates the isolation design.

Table 6.2: Parameters of the modelled and realized DAB converter with variable frequency modulation

Parameter	Value
Power rating	4 kW
Input voltage, V_1	800 V dc
Output voltage, V_2	50 – 800 V
Output current, I_2	5 A
Junction temperature, T_j	80 °C max
Filter dc capacitor	27 µF
Switch model, S	IKW40N120H3
Switching frequency, f_{sw}	4.6 – 21 kHz
Transformer core	4 x E100, 3C92
Number of primary turns	61
Winding dc resistance, R_{tr_w}	130 mΩ
Turn ratio, n	1
Total inductance, L_k	465 µH
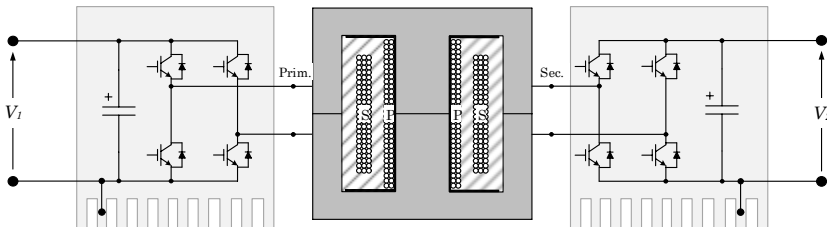
Figure 6.5: Two-dimensional DAB representation with the transformer as the intermediate stage

Both primary and secondary DAB sides are grounded and connected to respective heatsinks. Those grounds have to be separated safely from each together because of the high voltage requirement. Switches are mounted to the heatsinks using screws to tighten them properly. However, switches are mounted through a collector (the drain, in the case of a MOSFET) plate for heat exchange. Therefore, each switch is separated from the heatsink using a highly thermally conductive voltage isolation pad, see Figure 6.6. These thermal pads need to provide an isolation of 800 V (operational, the pad material must be able to withstand at least 3 kV), since that is the maximum voltage that could appear between the two switch collectors in the converter leg and is defined with the dc-bus voltage.

To solve the electrical isolation requirement between two sides of the DAB, the design showed in Figure 6.7 is proposed. The same design provides not only the simple isolation solution but also the simple cooling method. To provide mechanical support for the created
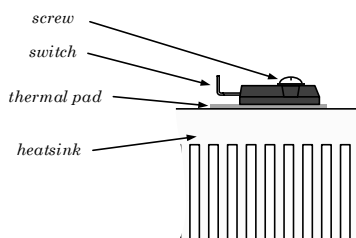
Figure 6.6: Switch mounted on the heatsink

structure, both DAB sides are mechanically connected using electrically isolating material (e.g., polyvinyl chloride – PVC).

6.3.1 Power loss distribution and thermal management

Since the DAB prototype is developed for test purposes, the cooling system has to be able to remove heat and keep the temperature in the component operation range. For the switches, it is recommended to operate at junction temperatures up to 80 °C, as the high temperature reduces the switch lifetime. Figure 6.8 presents the loss distribution over the single DAB module. Power loss values are estimated based on the developed loss model, and the worst-case scenario is taken as a reference for the thermal design considerations. As it can be seen, most of the losses are dissipated through switches.

To remove the heat from the heatsinks and the transformer, a forced-air cooling is employed. The forced-air cooling is the simplest solution because of the DAB structure and voltage isolation requirements. It is accomplished by employing a single fan at one side of the structure, as shown in Figure 6.9. Air flow provided by the fan is forced to go through heatsink extrusions by putting an air separation block. Furthermore, the air flow removes the heat from the transformer windings and the core. It is advisable to use smaller cores for the transformer, if possible, since the overall cooling surface is larger in that case. By inserting a small separation distance between each transformer core pair, it is ensured that the cooling surface is maximized. Figure 6.10 depicts the switches position on the DAB's single side heatsink.

6.3.2 Realized DAB test setup

The realized DAB test setup is shown with the photographs in Figure 6.11. It consists of four different printed circuit boards (PCBs), out of which two are power PCBs, and the other two are control PCBs. The test setup is built for different tests and conditions; therefore, it is designed with flexibility in mind. An additional switch leg is added to the output side of the DAB to test the CMC module operation as well. However, two outputs are left to connect test loads, one from the DAB and one from the added switch legs.
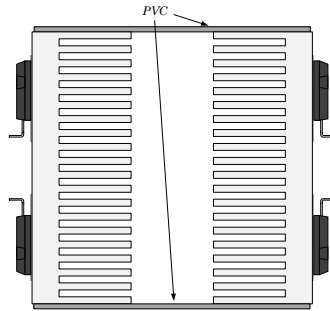
Figure 6.7: Front view of the DAB heatsink structure with mounted switches, and the anti-parallel diode share the same package (integrated) with the appropriate full-controllable switch
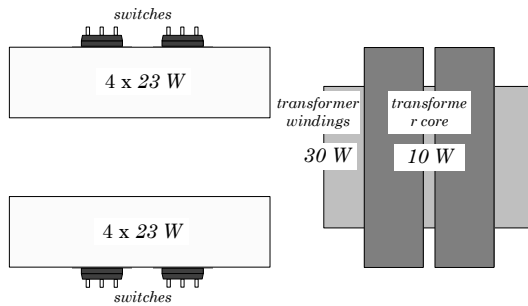
Figure 6.8: Power loss distribution over the DAB, auxiliary power supply omitted, top view
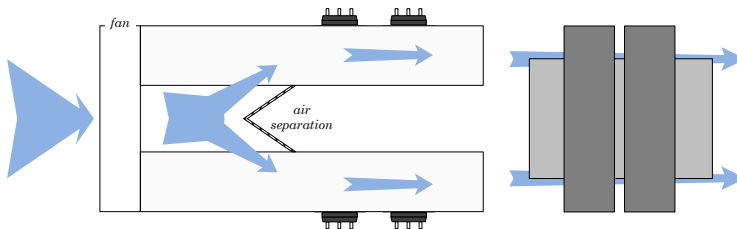
Figure 6.9: DAB module cooling method employing forced-air, top view
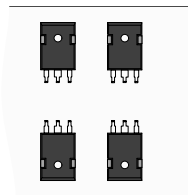
Figure 6.10: Switches' positions on the DAB's single side heatsink, mounting screws omitted, side view
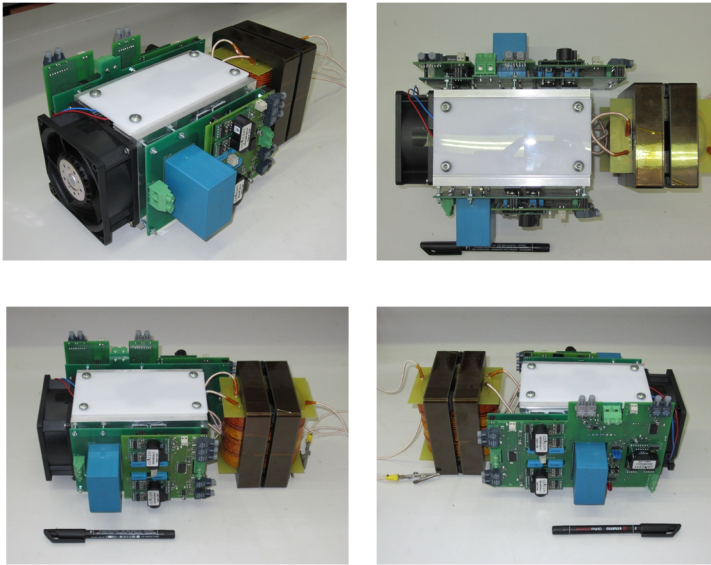
Figure 6.11: Realized DAB setup

Since all communication with the microcontroller is done via optical fibres, an additional adjustment board is designed to provide proper signal conversion, see Figure 6.12.

6.4 MODIFICATIONS FOR USING SiC MOSFETs

This section presents modification of the DAB setup for further efficiency improvements of the proposed dc-dc converter by employing new SiC MOSFET [88] switches, instead of the previously used Si IGBTs. As a large amount of energy circulates through the system, efficiency is a crucial parameter, the comparison between the SiC-MOSFET- and Si-IGBT-based converters is performed through a loss model. Experimental SiC-based DAB setup measurements are performed to support the loss model.

For both types of switches, the experimental work is carried out on a single module of the multilevel converter. Therefore, some small modifications are made in the converter circuit to provide proper function of the very fast SiC MOSFETs.

Figure 6.12: Optical fibre link adjustment board

The switch driver circuit provides +15/-8 V (V_H/V_L) to the gate of the switch, as these gate voltage levels are suitable for IGBTs. Figure 6.14 shows the measured switch gate driver output voltage. However, SiC MOSFETs have a maximum voltage rating of +25/-10 V, which makes the existing drivers on the setup not appropriate. A negative voltage of V_L = -8 V during the switch off-state is too close to the minimum rating, hence, the inclusion of a Zener diode over the gate-emitter to limit the voltage could be a solution. On the other hand, V_H = 15 V during the MOSFET's conduction period (on-state) provides a high drain-source resistance, thus, affecting the conduction losses of the switch and overall converter efficiency. Therefore, a small modification is performed on the existing IGBT driver circuit to make it more suitable for the driving of MOSFETs.

A detailed schematic of the IGBT driver is not provided by the manufacturer (Concept), and some components are integrated in a specially designed chip (integrated circuit). Hence, an analysis of the circuit was performed to investigate the limitations of the driver. From the datasheet, the minimum supply voltage for the IGBT driver is 12 V (tested as well), below which the under-voltage protection reacts. Figure 6.13 depicts the block diagram of the driver circuit. For a V_{DC} = 15 V supply voltage, the voltage on the secondary side is 23 V after rectification, and it is split into +15 V and -8 V relative to the common point. A change in the primary side supply voltage is directly reflected to the secondary. Therefore, setting the supply voltage of V_{DC} to 13 V does not trigger the under-voltage protection and provides
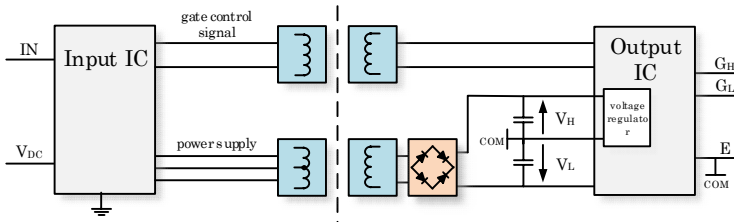
Figure 6.13: Switch driver block diagram

(a)   (b)
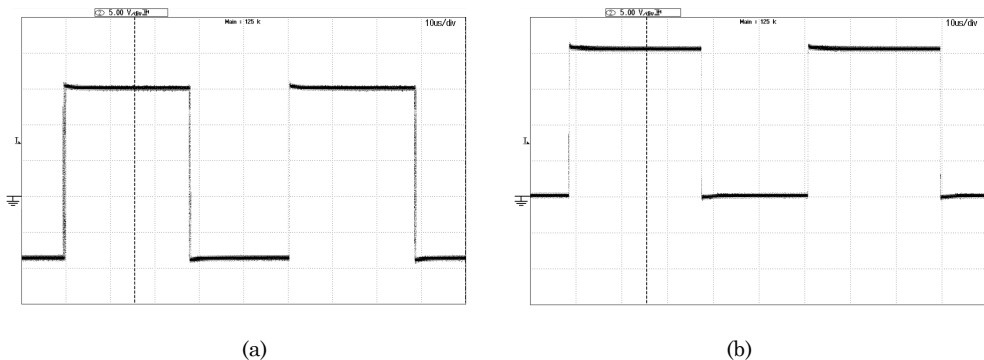
Figure 6.14: Measured gate driver signals before (a) and after (b) voltage level modification

21 V on the secondary side. V_H is regulated to 15 V using the output integrated circuit (IC), as now voltages are split into +15 V and -6 V relative to the common point. By short-circuiting the -6 V, the entire voltage (21 V) is applied to V_H, and during the switch off-state, the gate is connected to the common point of the driver's secondary side, $V_L = 0$ V. Figure 6.14 shows the measured switch gate driver output voltage after modification of the voltage levels.

Providing +21/0 V to the MOSFET's gate ensures the low conduction resistance of the switch. However, to keep the off-state ensured, negative voltage is preferable over the gate-source, as some current might flow through the Miller capacitance and charge the switch input enough to reach the gate threshold level and turn on the device. To prevent switch self-turn-on, an additional capacitance is added in parallel to the gate-source of the switch. Furthermore, a low resistance is put between the gate driver and the switch gate to comply with the datasheet values (switching energy test conditions). An extra transient voltage suppressor diode is added as well, with the purpose of providing the gate-source overvoltage protection.

6.5   EXPERIMENTAL VERIFICATION AND MEASUREMENTS

6.5.1   Single DAB setup measurements

Experimental efficiency measurements on the DAB setup are performed to validate the accuracy of the loss model. Measurements are obtained in predetermined voltage-current points using a Yokogawa PZ4000 power analyser. Open loop control is realized using a Texas Instruments microcontroller TMS320F2808.

Figure 6.15 presents a comparison of the calculated DAB efficiency curves and measured points, where the input voltage is kept constant while the output voltage is varying, as well as the output current. Overall, the calculated efficiency shows good agreement with the measurements, especially at the high power levels. The observed difference at the high power levels is less than 0.7% of the efficiency. However, at the lower power levels the difference becomes higher, mostly because of the fact that the model does not take into account voltage drop over the resistive components that carry the current. The measured peak efficiency is 97.1% for the Si-IGBT-based DAB. Figure 6.16 depicts the measured transformer primary and transformer secondary voltages and transformer current signals of the DAB under hybrid modulation. Figure 6.17 shows a comparison of the efficiency measurements points and calculated curves for the SiC-MOSFET-based DAB. Relatively good agreement is also achieved at high power levels with the observed difference below 1% and a measured maximum efficiency of 98.5%. Similar to the IGBT-based DAB, the error becomes larger at the low power level. However, some other effects cause a larger difference, like the inaccuracy of the transformer core loss model and the loss of the ZVS because of the high current ripple caused by the fast MOSFET transitions.
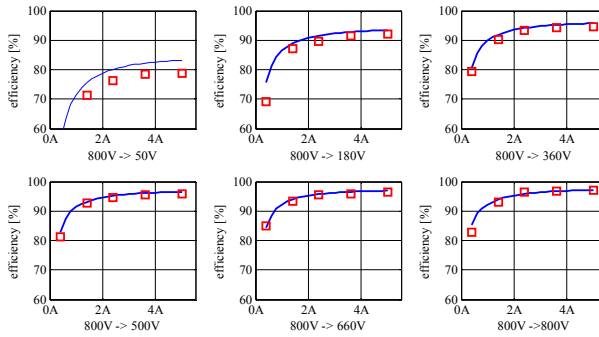
Figure 6.15: Measured (red □) and calculated (solid blue line) efficiencies for different operating points and output voltages of the IGBT-based DAB under trapezoidal control method and used IGBTs; V_1 = 800 V, V_2 is changing.

(a)   (b)   (c)
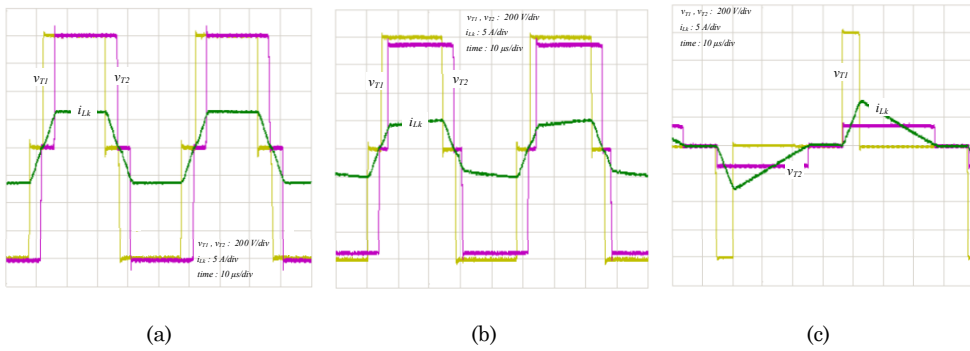
Figure 6.16: Measured DAB signals during charging of the DEAP at V_1 = 800 V and (a) V_2 = 800 V, I_2 = 5 A, f_{sw} = 20 kHz, measured efficiency of 97.1%; (b) V_2 = 750 V, I_2 = 3.5 A, f_{sw} = 21 kHz; (c) V_2 = 150 V, I_2 = 3 A, f_{sw} = 12 kHz.
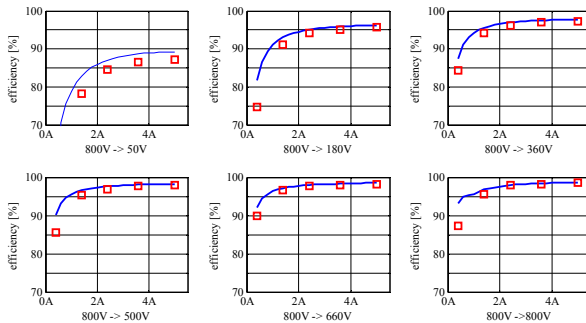
Figure 6.17: Measured (red □) and calculated (solid blue line) efficiencies for different operating points and output voltages of the SiC-MOSFET-based DAB under trapezoidal control method; V_1 = 800 V, V_2 is changing.

6.5.2 Triple DAB setup measurements

A test setup realized with three dual-active-bridge modules is assembled and tested to prove the concept of module stacking.

For the triple DAB test setup, three industrial grade transformers are designed and obtained from the manufacturer. The achieved leakage inductance in these transformers is 120 µH, which is close to laboratory obtained 75 µH, and still less than required for the modulation. Therefore, an auxiliary inductor is added in series with the winding of each transformer.

Figure 6.18 shows the triple DAB setup including the industrial transformers. Figure 6.19 presents the entire triple DAB test setup including power sources and load, while Figure 6.20 depicts the measured voltages and current within the triple DAB IPOS converter setup. Actual test was not up to the full voltage but at the 2.22 kV.
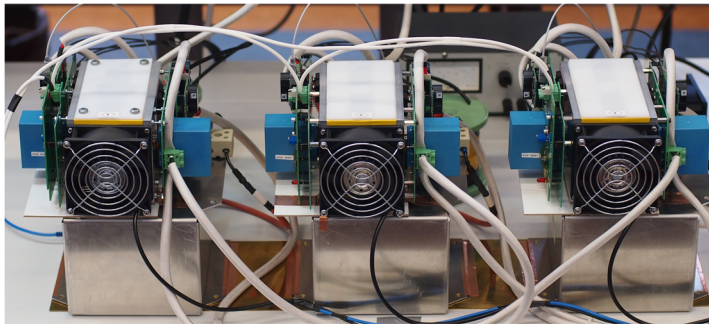
Figure 6.18: Triple DAB test setup close-up photo
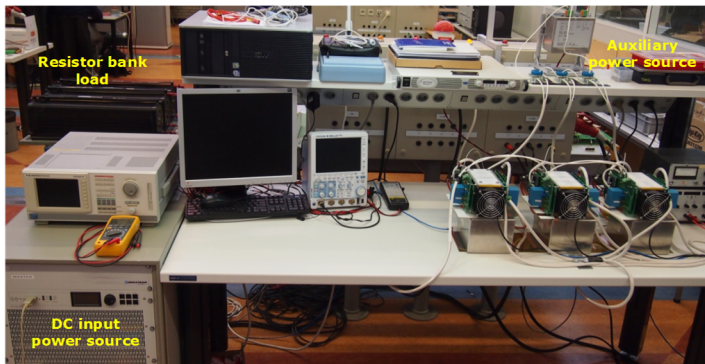
Figure 6.19: Entire triple DAB test setup with power sources and load
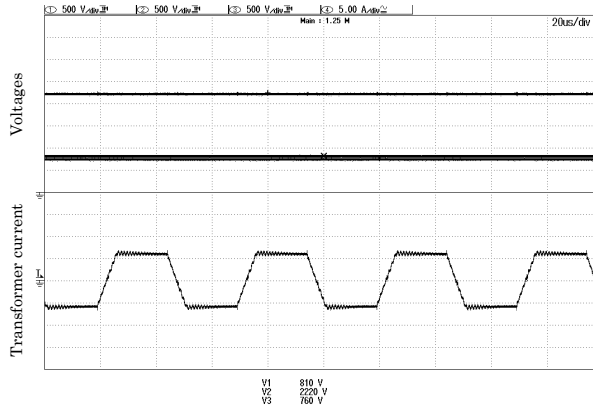
Figure 6.20: Oscilloscope screenshot showing the achieved high voltage of 2.22 kV at the high voltage side and the transformer current of the single DAB module. V1 – input voltage (dc source), V2 – output voltage (dc load), V3 – output voltage of the single DAB module

6.6 CONCLUSIONS

The most difficult design constrain is the required high-voltage isolation between the primary and secondary sides of the DAB module. The required high voltage isolation affects both the converter volume and design freedoms, and therefore, is the main limiting factor.

Experimental measurements show that the loss model is accurate enough with the error below 1% efficiency (at higher power levels), thus, it can be used for any future efficiency and harvesting cycle energy loss optimizations. However, the measured efficiency values should be used for long term system loss estimations, since they represent more realistic values.

Significant efficiency improvements are obtained by changing the converter switches from Si ($\eta_{peak} = 97.1\%$) to SiC ($\eta_{peak} = 98.5\%$). Overall, in one energy cycle, up to 50% less energy loss is observed with the developed loss model. The same DAB setup is used for both switch technologies, with the necessary gate driver modification to properly drive the MOSFETs. Overall, the achieved efficiency improvement makes SiC switches a competitive technology for the given sea wave energy application.

Chapter 7

Conclusions, contributions and future recommendations

7.1 CONCLUSIONS

The conclusions drawn from this thesis can be classified into five categories corresponding to the thesis objectives presented in Chapter 1, namely:

- Determine power electronic converter requirements;
- Identify suitable power electronic converter topologies and select the best one based on specifications of the DEAP WEC application;
- Model the selected power electronic converter topology and its interaction with the electro active polymer;
- Find converter operation modes to minimize overall conversion losses in the power electronic converter;
- Design and implement the power electronic converter, the proposed modulation strategy and validate loss models and modulation approaches.

7.1.1 Power electronic converter specifications

The power electronic converter needs an efficiency above 95% to produce power using the DEAP WEC within the selected operating area of the sea wave states. The lower limit of the efficiency is set by the smallest DEAP stretch ratio within the operating area (i.e., smaller waves that carry low power) and by the used segment dimensioning method together with the energy harvesting approach. The constant electric field yields the highest energy among three basic harvesting approaches. However, the energy yield difference is small for those three methods when very small relative deformations are applied to the dielectric elastomer (< 40%). Nonetheless, the design of the electrical system interaction with the DEAP is optimized for the constant electric field harvesting operation because of the highest energy yield potential. Considering the range of wave conditions, dielectric elastomer characteristics and energy production demand, an initial efficiency goal of 95% led to the dimensioning of the used DEAP material (10 m width and 250 m length), which is rolled to create a single DEAP WEC segment.

The spatial operation characteristic of the DEAP WEC allows for usage of a lower power rated inverters. At the same time, large power circulates between separated segments and other DEAP WECs in the energy harvesting farm. The DEAP WEC's mechanical structure and sea wave propagation define the shifted converter operation allocated to each segment within the same DEAP WEC.

The current rating is determined by the ratio between the converter's peak power and the power yield of the harvesting cycle. The maximum current is initially set to 5 A, as higher values would lead to excessive rated-to-yield power ratios. The present ratio is 10:1.

The converter has to provide a wide output voltage operation between 1 kV and 10 kV, while delivering the pulsed current required by the constant electric field harvesting approach.

The PEC is a bidirectional converter because the DEAP has to be charged and discharged in every cycle. Therefore, bidirectional converter operation is necessary. In addition, high PEC efficiency is desirable in the full power range to generate energy for the specified DEAP geometry and assumed sea wave conditions. The maximum DEAP material voltage is defined by the maximum allowed electric field strength and the largest thickness of the material. However, the maximum operating voltage because of the DEAP pre-stretch is lower and is set to 10 kV, which also represents the PEC output voltage rating.

7.1.2 Power electronic converter topology selection

The cascaded multilevel converter topology is the most suitable topology for the given dielectric elastomer energy harvesting application. Several topologies are investigated, and only three candidate topologies are selected for further detailed modelling and comparison through the defined comparison framework. These topologies are: two-quadrant half-bridge, flying-capacitor multilevel and cascaded multilevel.

The cascaded multilevel converter demonstrates higher frequency operation while delivering similar efficiency as the other analysed converter topologies. Additionally, the cascaded multilevel converter is able to fully discharge the dielectric elastomer, whereas the other two topologies' discharge depth is limited by the input dc-bus voltage. The cascaded multilevel topology consists of a number of identical modules. As a result, a high flexibility for control and design is provided, while avoiding the necessity of switch stacking. On the other hand, the cascaded multilevel converter requires a large number of switch components and accompanying driver circuits, as well as a high voltage isolation in the transformers of the modules.

The proposed modification to the cascaded multilevel topology, as presented in Chapter 4, removes one conversion stage within the module, i.e., the half-bridge. Consequently, the connection of dual-active-bridge modules are left to form the input-parallel-output-series connected converter. The potential for efficiency improvements of the DAB is high due to many modulation techniques that can be employed within this stage. The proposed IPOS-connected converter has 20% less switching components than the cascaded multilevel converter and a higher peak efficiency because of a smaller number of power conversion stages.

7.1.3 Power electronic converter loss modelling during harvesting cycle

A loss calculation method is developed to provide preliminary efficiency results used for cycle energy loss estimation in the power electronic converter. Additionally, the switching frequency is determined, as it is required for the size calculation of the converter magnetic and electrostatic components. The loss calculation relies on the developed analytical model of the converter for the steady state. The voltage transition modes are not considered in

some cases because of the low required output voltage slopes. Most of the power losses are calculated using component parameters obtained from the manufacturer's documentation. Effects caused by the parasitic elements appearing in the converter circuit, e.g., PCB layout stray inductance, are not considered at this stage. The calculated total power losses are later validated, proving that the loss model can be used for initial estimations.

The converter efficiency during harvesting cycle is defined to determine the converter efficiency influence on the energy circulation. It takes into account all operation points (voltage-current pairs) of the converter during the harvesting cycle and calculates losses accordingly. The calculated steady-state power electronic converter efficiency is used as an input and has different values for different voltages and currents, as required by the dielectric elastomer harvesting cycle. Therefore, the commonly used peak or average efficiency value does not provide any valuable information about the converter efficiency effect during the energy harvesting.

7.1.4 Power electronic converter operation modes for loss minimization

The combination of different modulation methods is required to meet the DEAP's wide voltage and current requirements coupled with the high efficiency. Since the proposed PEC consists of DAB modules, several modulation methods of the single dual-active-bridge module are investigated to maximize efficiency. The modulation approaches and their limitations are presented in this thesis.

A hybrid variable frequency modulation shows a higher efficiency during the harvesting cycle than the well-known phase-shift modulation, when both are applied on the same Si-IGBT-based PEC modules. The main constraint is the module operating output voltage range that originates from the entire converter output voltage requirement, when all modules operate the same way – deliver the same voltage and current.

The required output voltage range of the module limits the output current capability in case of trapezoidal and triangular DAB modulation modes, operating with a constant frequency, zero-current- and zero-voltage-switching. Since the pulsed current operation is required, the output current limitation is overcome by varying frequency according to the output voltage. Thus, the whole power range is covered with the hybrid variable frequency modulation method, i.e., the combination of two trapezoidal sub-modes and the triangular modulation mode. The first trapezoidal sub-mode performs the best at high power levels, within the hybrid modulation, whereas the second trapezoidal sub-mode covers most of the operating power range while delivering the lowest losses. The phase-shift modulation does not suffer from a current limiting drawback as the constant frequency trapezoidal and triangular modulations. However, the phase-shift modulation loses the soft-switching capability below a certain output voltage and becomes very inefficient causing efficiency to decrease substantially more than in the case of trapezoidal modulation.

The converter's topology modularity allows control freedom that increases the efficiency at the level of the full converter. Modules can be controlled individually, since each module has a dedicated controller unit. From the given generic example, in Chapter 6, it follows that for a positive change of module efficiency per power, the variable module control should be used. Otherwise, the all module active approach is the best option from the efficiency point of view. The hybrid module control method is introduced to ensure high conversion efficiency at almost any operating point. By applying the hybrid module control on the IPOS-connected converter during the harvesting cycle, the calculated efficiency improvement is 0.6% when compared with all module active approaches alone. The voltage that each module has to deliver to the output is determined with a module efficiency curve characteristic and required output voltage of the IPOS-connected converter. The proposed hybrid module control method is realized by employing knowledge about the module efficiency in the control loop of the multilevel converter, since it does not require any additional hardware for the converter.

7.1.5 Loss model and modulation strategy validation on an experimental setup

The single module dual-active-bridge converter test setup is built to validate the loss model and modulation strategy, while the IPOS consisting of three DABs is assembled for the validation of the IPOS concept.

It is shown that the anticipated largest IPOS topology bottleneck, i.e., the presence of a high-voltage isolation transformer, is not an obstacle in the module design. The achieved transformer leakage inductance is 75 µH for the laboratory assembled transformer and 120 µH for the industrial transformer. Nevertheless, the trapezoidal modulation requires a leakage inductance of approximately 500 µH and the phase-shift modulation in range of 800 µH. However, the high-voltage isolation requirement and transformer still represent the most difficult design constraints affecting volume and design freedoms.

Experimentally obtained measurements of the efficiency showed good agreement with the calculated values, especially at high power levels and for both utilized switch technologies, i.e., Si IGBT and SiC MOSFET. Overall, up to 50% less power loss is observed when SiC MOSFETs are used instead of Si IGBTs in the dual-active-bridge module. Therefore, the achieved efficiency improvement makes SiC switches a competitive technology for the given sea wave energy harvesting application.

7.2   CONTRIBUTIONS

The main thesis contributions can be summarized as follows:

- The thesis deals with the electric system for DEAP-based wave energy harvesting at the large scale. Up to now, only small scale DEAP-based systems, for converting mechanical to electric energy, have been analysed in the literature through simulations or prototype tests. System overview is shown for the large scale DEAP wave energy conversion, while focusing on the power electronics converter stage responsible for energy harvesting;

- Overview and study of candidate PEC topologies are provided. While some topologies are analysed in depth, some are briefly explained as they could be better candidates in a case of a different system. Thus, the thesis gives a wide spectrum of possibilities through the PEC topologies overview;

- The framework is developed to identify the best topology for PEC. This framework is a tool the can be used to help choosing among different topologies and it is not limited to the DEAP WEC, but can be adapted for any other PEC application. Specifically for the DEAP application, definition of the power converter efficiency during harvesting cycle is introduced;

- A systematic and clear description on the DAB loss modelling is provided and it is further validated on the experimental setup. Therefore, it can be considered as a valid method for efficiency estimation;

- Different DAB modulation techniques are analysed in depth for the required wide-voltage operation and pulse current output for this application. Variable frequency modulation is introduced to cover output current requirement over the wide voltage operation; hence, improving efficiency at low voltages as the switching frequency decreases with the output voltage. Normally, this kind of requirements for DAB circuit are not common in the literature, thus, the study results and methodology presented in this thesis are a valuable source. The limitation of the modulation techniques are clearly derived and the combination of triangular and trapezoidal modulations (hybrid modulation) is suggested as the optimal solution for loss minimization;

- The hybrid method is proposed to optimize efficiency of the entire IPOS-connected converter by individually controlling modules, while taking into account the efficiency curve as the input parameter function;

- The thesis clearly suggests that the IPOS-connected converter is the best for the DEAP WEC application at this scale. Other topologies, among those presented and more, can be considered if the electrical requirements are very different than those studied here. However, the IPOS-connected converter is a versatile circuit with many advantages that are difficult to suppress: high efficiency, modularity, scalability, large spectrum of known modulations and control methods.

7.3 FUTURE WORK RECOMMENDATIONS

7.3.1 Other modulation methods for the DAB

Implementing additional modulation approaches for the DAB could result in a higher power electronic converter efficiency if coupled with optimal switch technology. The dual-active-bridge is a well-known converter topology with a large number of proposed modulation techniques in the literature and practice. The modulation approaches used in this thesis are selected based on their actual usage, wide voltage operation and estimated efficiency. However, some other modulations could also be applied to the proposed IPOS-connected converter modules as well.

7.3.2 Loss model improvement

The loss model could be improved based on the converter test setup measurements. In the first step, the loss values are obtained from the manufacturer documentation, and therefore, efficiency is estimated. The next step would be an improvement of the loss model according to the measurements of devices under actual operation conditions. Additionally, the used method for calculation of losses in the inductor core material does not take into account the effect of dc bias flux. Therefore, including dc bias flux will result in a more accurate model for inductor loss estimation.

7.3.3 Optimization of the module

The converter module optimization has to be done to deliver the optimal design from an efficiency and volume point of view. The DAB module test setup in this thesis is not entirely optimized for the proposed modulation method nor for the volume requirement. On top of that, the latest standards concerning voltage insulation have to be taken into account while designing the power converter, which will also affect its size.

7.3.4 Power electronic converter and system control

The entire power electronic converter can use a master-slave control approach, where individual modules have a dedicated slave controller that communicates only with the master controller. The master controller takes care of the dielectric elastomer voltage and current control by sending requested voltages to modules. Furthermore, the slave controller takes the received voltage as the reference value for the dual-active-bridge module, and via generated PWM signals, provides the current necessary to keep the output voltage according to the reference. The slave controller also sends information signals to the master controller, e.g., status and low sample rate measurement. The proposed DAB modulation modes and module control strategies require intensive and complex signal processing, which is a challenging task for the future research.

To increase the robustness of the power electronic converter control, a distributed control can be utilized. In the case of distributed control, there is no need for a separate master controller, as each individual module controller can act as the master, while communication is done through a common signal bus.

At the system level, the system controller that sends the required optimal current waveforms to the individual DEAP generator power electronic converters (master controllers) can control the entire DEAP WEC structure. Each current waveform has a precise timing and is defined by time length of the charging, discharging and constant electric field periods, as well as with the appropriate current values. The control loop of the system controller is closed through a pressure sensor, used for the detection of sea wave amplitudes and time periods, positioned ahead of the DEAP WEC and in the direction of the coming waves.

7.3.5   EMC investigation

For the converter to operate in the DEAP WEC system and because of the sensitivity of the measurement equipment, the internal EMC has to be addressed in future research. This is especially valid if zero-current soft switching and hard switching are applied.

7.3.6   DEAP energy harvesting optimization with respect to converter efficiency

There is the possibility to increase overall energy yield if the electroactive polymer current is adjusted to the efficiency curve shape of the converter. Basic approaches for energy harvesting from dielectric elastomers used in this thesis are not the taking the power electronic converter efficiency behaviour into account. This thesis deals with the maximization of the converter efficiency for the assumed dielectric elastomer current waveforms, which are not proven to be optimal. However, another approach can be used, i.e., for the given converter efficiency, the dielectric elastomer current shape can be modified to deliver an overall higher energy. Nevertheless, since this thesis's approach already maximizes the converter efficiency for the assumed dielectric elastomer current shape, there is not much freedom for further energy yield improvements through the current shape optimization for the proposed PEC.

Appendix

A.1. COMPONENT DESIGN

A.1.1. Inductor

All inductors in the converters are designed using known method described in [89]. Basically, the design procedure of the non-air core inductors can be described as shown in Figure A.1 (on the left).

First, the required inductance is determined for the given current ripple. Thus, the maximum current in the inductor is obtained as well. These two parameters are main inputs for the inductor design procedure. Next step is the core geometry and material choices. In this thesis, used frequencies are in range of tens of kilohertz, therefore, the ferrite material is utilized for the inductor core. At this stage the desired maximum wire resistance is set, as well as the specific wire resistance for the given temperature and material. Winding wire fill factor is the ratio of the effective wire area to the total wire cross section area. The winding wire fill factor usually have a value of 0.4 for the Litz wire, for example, as the multiple wire strings share the total wire area.

Next, K_{g1} and K_{g2} factors are calculated and compared. If relation $K_{g1} \geq K_{g2}$ is satisfied, the core choice is good and other parameters of the inductor design can be calculated. These are: air gap inserter between cores, number of winding turns, cross section area of the wire that can be implemented and dc resistance of the winding. If the relation is not satisfied, the core geometry and material have to be changed and the whole process repeated until the relation is fulfilled.

The previously described inductor design procedure does not take into account the loss calculation within the inductor and optimization of the design regarding the loss minimization. Therefore, the additional blocks are added to the existing design procedure in order to minimize inductor losses, see Figure A.1 (right). Here, most of the procedure from Figure A.1 (left) is included in the block that calculates K_{g1}, K_{g2} and R_{wire}. However, the iteration has been removed and put outside. After all necessary parameters are known, the calculation of losses in the inductor winding wire and core is performed. The calculation of these losses is described in Chapter 3.3 of this thesis.

In Figure A.1 (right), block Change core geometry refers to a process where the core dimensions are changed. For sake of simplicity, core geometry changes only with number of identical cores added or removed from the inductor structure. Therefore, further loss optimization within the selected core geometry is not performed. The determined inductor designs for each converter topology are given in the following text.

Determine:
L – inductance
$I_{L(max)}$ – inductor peak current

Change core geometry

Set:
B_{max} – max. flux density
A_{core} – core effective cross section area
V_{core} – core volume
$A_{winding}$ – winding area
$R_{wire(max)}$ – max. wire resistance
ρ_{wire} – wire specific resistance
MLT – mean length per turn
K_u – winding wire fill factor

Calculate:
$$K_{g1} = \frac{A_{core}^2 A_{winding}}{MLT}$$
$$K_{g2} = \frac{\rho_{wire} L^2 I_{max}^2}{B_{max}^2 R_{wire} K_u}$$

Check:
Is $K_{g1} \geq K_{g2}$?   NO   YES

Calculate new:
$$l_g = \mu_o \frac{LI_{max}^2}{B_{max}^2 A_{core}} \rightarrow \text{air gap}$$
$$n_{turn} = \frac{LI_{max}}{B_{max} A_{core}} \rightarrow \text{No. of turns}$$
$$A_{wire} = K_u \frac{A_{winding}}{n_{turn}} \rightarrow \text{wire area}$$
$$R_{wire} = \rho_{wire} \frac{n_{turn} MLT}{A_{wire}}$$

Determine:
L – inductance
$I_{L(max)}$ – inductor peak current

P_{total_min} = infinite
$i = 1$; $i_{stored} = 0$; i_{max} = max. iterations

Calculate:
K_{g1}, K_{g2}, R_{wire}
If $(K_{g1} \geq K_{g2})$ $P_{design}(i) = 1$
else $t_{design}(i) = 0$

Calculate:
$P_{total}(i) = P_{core}(i) + P_{wire}(i)$

Check:
Is $(P_{total}(i) \leq P_{loss(min)})$ & $(P_{design}(i)=1)$?   YES

New minimum:
$P_{total(min)} = P_{total}(i)$
$i_{stored} = i$

Change core geometry   NO

Next step:
$i = i + 1$
Is $i > i_{max}$?   NO   YES

Design under ordinal number
i_{stored}
chosen

Figure A.1: Inductor design procedure [89] (left) and modified design procedure with minimization of losses (right)

A.1.1.1. *Input inductor*

For the two-quadrant converter, input inductor L value is determined based on a maximum accumulated energy that appear during converter operation. Thus, maximum value of volt-seconds is for the maximum voltage step-up ration, i.e. $V_{DE} = 10$ kV. Input inductor current ripple is set to $\Delta I_L = 40$ A, hence giving the peak inductor current of $I_{L\_max} = 82.5$ A. The input inductor design results are given in Table 3.1, in Chapter 3. Figure A.2 shows number of core pairs determination through the utilized design procedure and calculated core and winding losses individually. The utilized core geometry is E100/60/28 from Ferroxcube and ferrite material 3C92 with maximum B_{max} set to 200 mT. The value of R_{wire_max} is set to 0.2 Ω. Maximum winding current density is 3 A/mm².
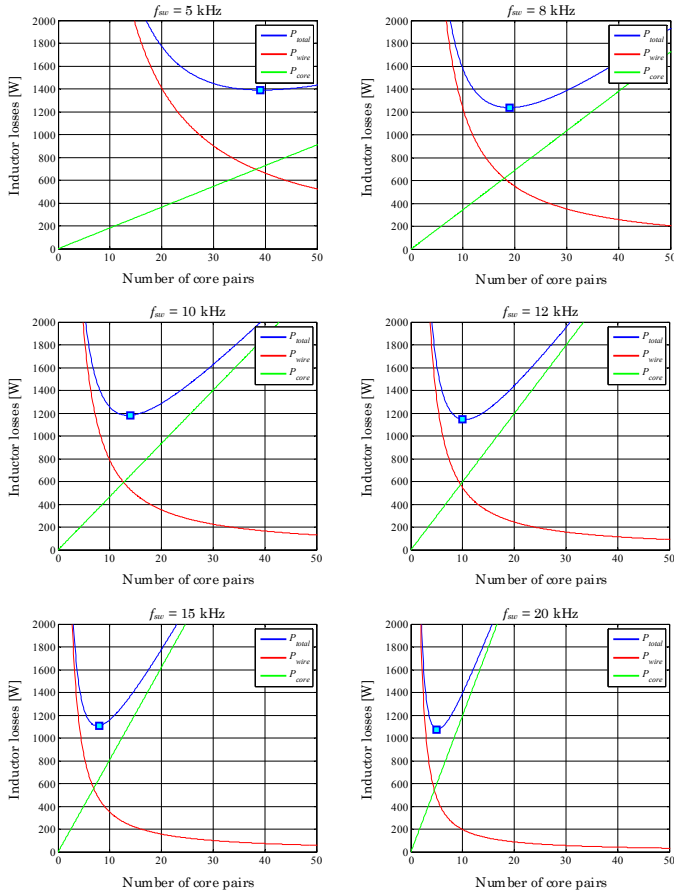
Figure A.2: Number of core pairs determination for input inductor of the two-quadrant converter

The flying-capacitor converter input inductor L value is also determined based on a maximum accumulated energy that appear during converter operation. The maximum value of volt-seconds is for the maximum voltage step-up ration, i.e. V_{DE} = 10 kV. Input inductor current ripple is set to ΔI_L = 1.5 A, hence giving the peak inductor current of I_{L_max} = 63.26 A. The input inductor design results are given in Table 3.3, in Chapter 3. Figure A.3 shows number of core pairs determination through the utilized design procedure and calculated core and winding losses individually. The utilized core geometry is E65/32/27 from Ferroxcube and ferrite material 3C92 with maximum B_{max} set to 200 mT. The value of R_{wire_max} is set to 0.1 Ω. Maximum winding current density is 3 A/mm².
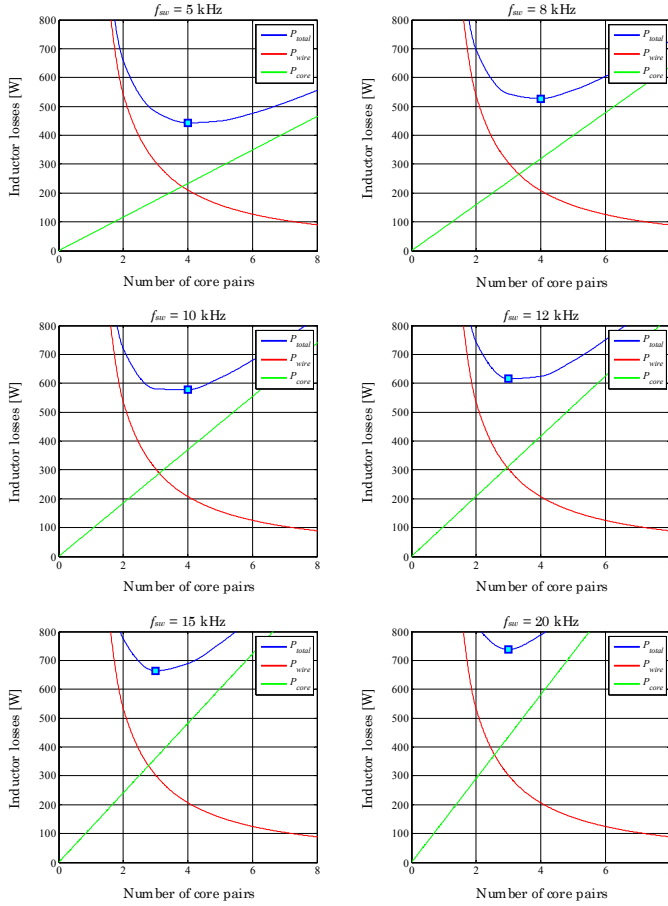
Figure A.3: Number of core pairs determination for input inductor of the flying-capacitor multilevel converter

The specific resistance of the winding wire is determined as:

$$\rho_{wire} = 1.68 \times 10^8 \left(1 + 0.004041 \left(T_{wire} - 20\right)\right), \tag{A.1}$$

where T_{wire} is set to 60 °C.

A.1.1.2.   Output filter inductor

The output filter inductor for 2QC and FCMC are taken to be the same. Since power dissipated within the filter inductor is assumed to be low, additional design procedure for loss minimization is not performed. Therefore, applied design procedure is the one given in Figure A.1 (left). The results of the design are presented in Table 3.1 and Table 3.3. The inductor size is calculated as:

$$L_{filter} = \frac{V_{Lfilter}D_{\max}}{\Delta I_{Lfilter}f_{sw}} , \tag{A.2}$$

where $D_{\max}$ is maximum duty cycle, $\Delta I_{Lfilter}$ inductor current ripple. Inductor ripple current is set to $\Delta I_{Lfilter} = 1$ A. The $V_{Lfilter}$ is determined by the output filter capacitor voltage ripple, that is 40 V. For desing procedure, the following values are set: $B_{\max} = 300$ mT and $R_{wire(\max)} = 0.2$ Ω. Number of core pairs is fixed to two of E42/21/20, from Ferroxcube manufacturer and 3C92 ferrite material. Filter inductor peak current value is calculated as

$$I_{Lfilter(\max)} = I_{DE} + \frac{\Delta I_{Lfilter}}{2} . \tag{A.3}$$

A.1.2. Transformer

Transformer in the converter is designed using known method described in [89]. Basically, the design procedure of the non-air core transformer can be described as shown in Figure A.5. Maximum winding current density is 3 A/mm², while maximum flux density of the core is $B_{\max} = 200$ mT. Number of primary turns is calculated based on the maximum winding voltage value applied for a half of the switching period. By this, the transformer core is slightly oversized. Further, the wire cross section area is determined in a way that primary and secondary windings share equally the winding area, since the transformer turns ratio is one. Also, the winding area is reduced by 30% in order to leave space for the required isolation layers. Next, the resistance of the single winding is calculated and further used for estimation of winding losses. Both winding and core losses are calculated according to method described in Chapter 3 of this thesis.

In order to determine maximum transformer core flux density, a voltage over magnetizing inductance V_{Lm} has to be calculated. It is assumed that the magnetizing inductance is much larger than the leakage inductance, $L_m \gg L_k$. The leakage inductance is measured on the primary terminal of the transformer, while the secondary terminal is shorted. Therefore, the leakage inductance is $L_k = L_{pri} + L_{sec}/n^2$. Assuming winding turns ration of 1 and identical primary and secondary windings inductances, the voltage over magnetizing current can be calculated as:

$$v_{Lm}(t) = v_{T1}(t) - \frac{v_{T1}(t) - v_{T2}(t)/n}{2} . \tag{A.4}$$
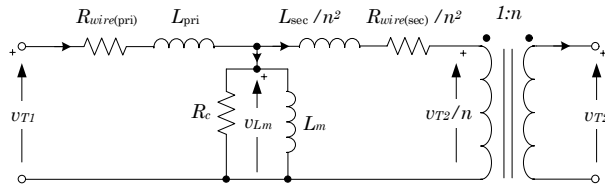
Figure A.4: Transformer equivalent circuit
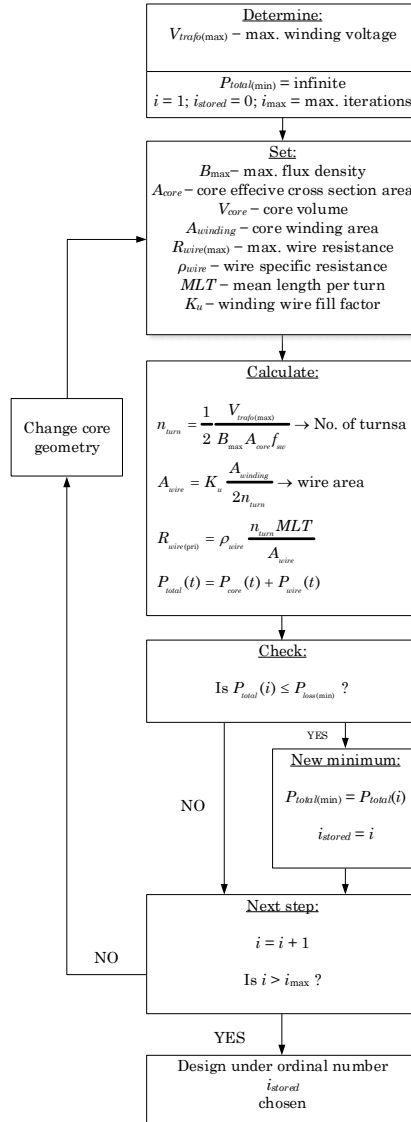
Figure A.5: Transformer design procedure with loss minimization

For the case when $V_1 = V_2/n$, magnetizing inductance for phase-shift and trapezoidal DAB modulations is:

$$v_{Lm}(t) = \begin{cases} 0, & 0 < t \leq xT \\ V_1, & xT < t \leq \dfrac{T}{2} \\ 0, & \dfrac{T}{2} < t \leq xT + \dfrac{T}{2} \\ -V_1, & xT + \dfrac{T}{2} < t \leq T \end{cases} \tag{A.5}$$

for the phase-shift modulation and

$$v_{Lm}(t) = \begin{cases} \dfrac{V_1}{2}, & 0 < t \leq x_1 T \\ V_1, & x_1 T < t \leq (x_1 + x_2)T \\ \dfrac{V_2}{2n}, & (x_1 + x_2)T < t \leq (x_1 + x_2 + x_3)T \\ 0, & (x_1 + x_2 + x_3)T < t \leq \dfrac{T}{2} \\ -\dfrac{V_1}{2}, & \dfrac{T}{2} < t \leq x_1 T + \dfrac{T}{2} \\ -V_1, & x_1 T + \dfrac{T}{2} < t \leq (x_1 + x_2)T + \dfrac{T}{2} \\ -\dfrac{V_2}{2n}, & (x_1 + x_2)T + \dfrac{T}{2} < t \leq (x_1 + x_2 + x_3)T + \dfrac{T}{2} \\ 0, & (x_1 + x_2 + x_3)T + \dfrac{T}{2} < t \leq T \end{cases} \tag{A.6}$$

for the trapezoidal modulation. Figure A.6 shows number of core pairs determination through the utilized design procedure and calculated core and winding losses individually. The utilized core geometry is E100/60/28 from Ferroxcube and ferrite material 3C92.

Transformer leakage inductance for Cascaded Multilevel converter module and applied phase-shift modulation is determined using:

$$L_k = \frac{x V_{Lk(\max)}}{\Delta I_{Lk} f_{sw}}, \tag{A.7}$$

where x denotes phase-shift value, $V_{Lk(\max)}$ denotes maximum voltage applied over the leakage inductance and ΔI_{Lk} current change through the leakage inductance for the applied voltage during phase-shift period x/f_{sw}. In order to simplify calculation and modelling, for CM converter module a value of 0.1 is set for the phase-shift x applied over all investigated frequencies.
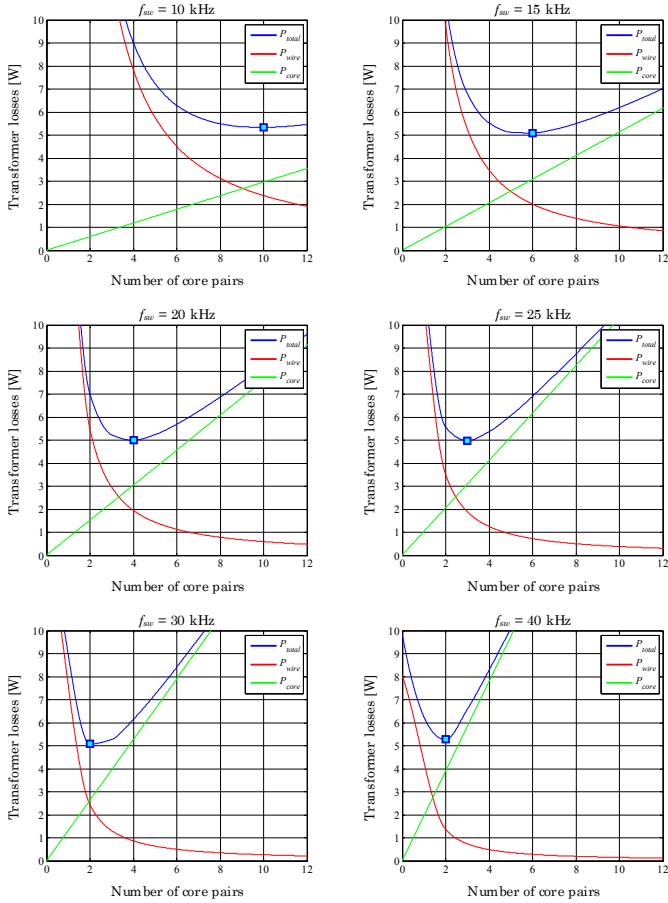
Figure A.6: Number of core pairs determination for transformer of the cascaded multilevel converter

A.1.3. Capacitor

All filter dc capacitors for converters are calculated using known equation:

$$C = \frac{\Delta Q_c}{\Delta V_c},$$ (A.8)

where ΔQ_c denotes amount of charge delivered or removed from the capacitor while causing ΔV_c change in capacitor voltage. The value of ΔV_c for the input and output filter capacitors is set to 40 V, which is 5% of the specified input voltage (800 V) of the dc-bus. The input capacitor $\Delta Q_{c(in)}$ for 2QC and FCMC is calculated as:

$$\Delta Q_{c(\text{in})} = \frac{1}{2}\frac{\Delta I_L}{f_{sw}}, \quad \text{for 2QC}$$

$$\Delta Q_{c(\text{in})} = \frac{1}{2}\frac{\Delta I_L}{N_m f_{sw}}, \quad \text{for FCMC}$$

(A.9)

where N_m denotes number of modules within multilevel converter, while for the output high voltage capacitor $\Delta Q_{c(\text{out})}$ is determined using:

$$\Delta Q_{c(\text{out})} = \frac{D_{\max}I_{DE}}{f_{sw}}, \quad \text{for 2QC and FCMC}$$

$$D_{\max} = 1 - \frac{V_{BUS}}{V_{DE(\max)}}$$

(A.10)

The FCMC has a large number of clamping dc capacitors that carry the full current of the converter. The clamping capacitor $\Delta V_{c(\text{clamp})}$ is determined by the maximum operating blocking voltage of the switches, which is in this case set to 850 V, therefore giving $\Delta V_{c(\text{clamp})} = 100$ V. The amount of charge $\Delta Q_{c(\text{clamp})}$ is calculated as:

$$\Delta Q_{c(\text{clamp})} = \frac{D_{\max}I_{L(\text{av})}}{N_m f_{sw}},$$

(A.11)

where $I_{L(\text{av})}$ is the input inductor (or converter input) average current value.

The high voltage capacitors in the converter are design in a way the one basic unit has rating of 800 V dc, and if higher voltage is needed the basic units are stacked in series to reach required voltage level and in parallel to keep desired capacitance. Number of output filter capacitors in 2QC and FCMC is given as:

$$N_{c(\text{out})} = \left\lceil \left(\frac{V_{DE(\max)}}{800 \text{ V}}\right)\right\rceil^2,$$

(A.12)

while number of clamping capacitors within FCMC is:

$$N_{c(\text{clamp})} = \frac{N_m(2N_m+1)(N_m+1)}{6} - N_m^2 .$$

(A.13)

For the CMC, both input and output filter dc capacitor amount charges are calculated as:

$$\Delta Q_{c(\text{DAB})} = \frac{1}{2}\frac{I_{DE}^2 x}{I_H f_{sw}},$$

(A.14)

where I_H denotes the peak current through the DAB transformer leakage inductance and x the phase-shift value of the applied phase-shift modulation.

A.1.4. Component characteristics

A.1.4.1. Switch

Switch parameters are obtained from the manufacturer datasheet. Two different types of switches are used for the investigation, i.e. Si IGBT from Infineon [87] and SiC MOSFET from Cree [88].

The switching energy loss is sampled from the provided datasheet graph, then interpolated and finally scaled to applied conditions. Two linear scaling functions are used for switching energy: blocking voltage k_v and junction temperature k_{Ts} scaling functions. The purpose of scaling functions is to scale datasheet values according to the conditions under which the switch operates. Linear scaling functions for both switches are given in Table A.1, where k_{Ts} scales the sampled datasheet value of the switching energy obtained for the given junction temperature. V_{dc} referes to the applied dc blocking voltage over the switch, V_{test} is the datasheet test blocking voltage for which all values are given and T_j refers to the switch junction temperature. The junction temperature is estimated using:

$$T_j = T_{j(\max)}\left(1 - \frac{T_{j(\max)} - T_{j(\min)}}{P_{\max} - P_{\min}}\frac{P_{\max} - I_{DE}V_{DE}}{T_{j(\max)}}\right),\qquad(A.15)$$

where $T_{j(\max)}$ and $T_{j(\min)}$ are junction temperatures at maximum ($P_{\max}$) and minimum ($P_{\min}$) power transfers, respectively. Switch on-state resistance is also scaled with the linear function regarding the junction temperature. The datasheet sampled on-state resistance is obtained for the maximum junction temperature and then scaled down to a calculated junction temperature.

Table A.1: Switch linear scaling functions

Scaling function	IGBT IKW40N120H3	MOSFET C2M0080120D
$k_{Ts(\text{off})}$	$1 - \dfrac{0.01\left(175°\text{C} - T_j\right)}{2.7}$	$1 + \dfrac{0.56\left(T_j - 25°\text{C}\right)}{210}$
$k_{Ts(\text{on})}$	$1 - \dfrac{0.01\left(175°\text{C} - T_j\right)}{4.5}$	$1 - \dfrac{0.16\left(T_j - 25°\text{C}\right)}{310}$
k_v	$1 + \dfrac{0.19\left(V_{dc} - V_{test}\right)}{200}$	$1 + \dfrac{\left(V_{dc} - V_{test}\right)}{V_{test}}$
k_{Tc}	$1 - \dfrac{0.067\left(175°\text{C} - T_j\right)}{45}$	$1 - \dfrac{0.48\left(150°\text{C} - T_j\right)}{113}$

A.1.4.2. Diode

Diode parameters are obtained from the manufacturer datasheet. Since used diodes are built-in as the anti-parallel diodes in the switch case, the same datasheets are used as for the switches. However, it is assumed that for the SiC MOSFET, a built-in diode does not conduct as the MOSFET takes over all the current. Therefore, the MOSFET built-in diode conducts only during dead time, thus diode conduction losses are neglected, if SiC MOSFET is utilized.

For the built-in diode within the IGBT case, on-state resistance linear scaling function is:

$$k_{Tc} = 1 - \frac{0.1\left(175°C - T_j\right)}{50}. \tag{A.16}$$

A.1.4.3. Core material

Core material losses are calculated using equations from Chapter 3 in this thesis. Equation (3.15) requires core material constants which are not provided in the manufacturer datasheet, in this case Ferroxcube [90]. For the used ferrite material type 3C92, the following system of equation is obtained from the datasheet documentation:

$$\begin{bmatrix} a\left(25\times10^{-3}\right)^b 0.2^c - 55\times10^{-3} \\ a\left(25\times10^{-3}\right)^b 0.3^c - 200\times10^{-3} \\ a\left(100\times10^{-3}\right)^b 0.1^c - 40\times10^{-3} \end{bmatrix}. \tag{A.17}$$

Further, solving the system of equation the 3C92 core material constants are obtained as:

$$\begin{aligned} C_m &= a = 9.43 \\ \alpha &= b = 1.36 \\ \beta &= c = 3.18 \end{aligned} \quad . \tag{A.18}$$

References

[1]   E. U. C.-H. o. Lords, "The EU's Target for Renewable Energy: 20% by 2020," in "27th Report of Session 2007–08," 2008.

[2]   Energy Efficiency and its contribution to energy security and the 2030 Framework for climate and energy policy.

[3]   REN21, "Renewables 2018 Global Status Report," REN21 2018.

[4]   J. Cruz, *Ocean wave energy*. Springer, 2008.

[5]   B. Drew, A. R. Plummer, and M. N. Sahinkaya, "A review of wave energy converter technology," *Journal of Power and Energy,* vol. Vol. 1, 2009.

[6]   M. Andersen, K. Argyriadis, and S. Butterfield, "Ocean wind and wave energy utilazition," *17th   International Ship and Offshore Structures Congress,* no. Seoul, Korea, August 2007.

[7]   M. Previsic, "Offshore wave energy conversion devices," Electrical Power Research Institute2004.

[8]   M. Previsic, "Wave Power Technologies," *Power Engineering Society General Meeting,* vol. Vol. 2, June 2005.

[9]   J. Falnes, "A review of wave-energy extraction," *Marine Structures,* vol. 20, no. 4, pp. 185-201, 10// 2007.

[10]   J. F. Chozas and H. C. Soerensen, "State of the Art of Wave Energy in Spain," in *Electrical Power & Energy Conference (EPEC), 2009 IEEE*, 2009, pp. 1-6.

[11]   R. Bedard, G. Hagerman, M. Previsic, O. Siddiqui, R. Thresher, and B. Ram, "Final summary report - Project definition study, offshore wave power feasibility demonstration project," September 22 2005.

[12]   B. Czech and P. Bauer, "Wave Energy Converter Concepts : Design Challenges and Classification," *Industrial Electronics Magazine, IEEE,* vol. 6, no. 2, pp. 4-16, 2012.

[13]   T. W. Thorpe, "The Wave Energy Programme in the UK and the European Wave Energy Network " in *Fourth European Wave Energy Conference*, Denmark, 2000, pp. 19-27.

[14]   F. G. Nielsen *et al.*, "Ocean wind and wave energy utilization," presented at the 17th *International Ship and Offshore Structures Congress* Aug. 16–21, 2006.

[15]   T. W. Thorpe, "A brief review of wave energy," Energy Technology Support Unit (ETSU)1999.

[16]   A. Clément *et al.*, "Wave energy in Europe: current status and perspectives," *Renewable and Sustainable Energy Reviews,* vol. 6, no. 5, pp. 405-431, 10// 2002.

[17]   http://www.emec.org.uk/marine-energy/wave-developers/.

[18]   http://www.ey.com/Publication/vwLUAssets/.

[19]   P. Jean *et al.*, "Standing wave tube electro active polymer wave energy converter," presented at the *SPIE Proceedings, Electroactive Polymer Actuators and Devices (EAPAD) 2012*, 2012.

[20]   R. v. Kessel, A. Wattez, and P. Bauer, "The effect of converter efficiency on DEAP-based energy conversion: an overview and optimization method," in *Proc. SPIE 9056, EAPAD 2014*, 2014.

[21]   R. D. Kornbluh *et al.*, "From boots to buoys: promises and challenges of dielectric elastomer energy harvesting," presented at the Proc. *SPIE 7976, Electroactive Polymer Actuators and Devices (EAPAD) 2011*, 29 March, 2011.

[22]   Y. Bar-Cohen, "Electroactive polymer (EAP) actuators as artificial muscles: reality, potential, and challenges," vol. PM136, 18 March ed: *SPIE press*, 2004, p. 816.

[23]   F. Carpi, D. De Rossi, R. Kornbluh, R. Perline, and P. Sommer-Larsen, Dielectric Elastomers as Electromechanical Transducers - Fundamentals, Materials, Devices, Models and Applications of an Emerging Electroactive Polymer Technology. 2008.

[24]   A. S. C. Lagomarsini, C. Jean-Mistral and S. Monfray, "Coupling of electro-active polymers for energy harvesting applications," *2016 IEEE International Conference on Dielectrics (ICD),* pp. 443-446, 2016.

[25]   P. C. B. a. K. K. Ahn, "Investigation on optimization the performance of a wave energy converter using Dielectric electro-active polymers," *2015 15th International Conference on Control, Automation and Systems (ICCAS),* pp. 1915-1919, 2015.

[26]   C. Mangeot. Development of a low voltage Dielectric Electro-Active Polymer actuator [Online].

[27]   D. Gatti, H. Haus, M. Matysek, B. Frohnapfel, C. Tropea, and H. F. Schlaak, "The dielectric breakdown limit of silicone dielectric elastomer actuators," *Applied Physics Letters,* vol. 104, no. 5, pp. 052905-052905-4, 2014.

[28]   D. Gatti, H. Haus, M. Matysek, B. Frohnapfel, C. Tropea, and H. F. Schlaak, "The dielectric breakdown limit of silicone dielectric elastomer actuators," *Applied Physics Letters 104, 052905 (2014),* 2014.

[29]   R. van Kessel, "Innovative wave energy conversion: Optimization of the energy harvesting cycle and converter design for a wave energy converter with Electro Active Polymers," MSc, Delft University of Technology, October 2010.

[30]   R. van Kessel, B. Czech, P. Bauer, and J. A. Ferreira, "Optimizing the dielectric elastomer energy harvesting cycles," *IECON 2010 - 36th Annual Conference on IEEE Industrial Electronics Society* pp. 1281 - 1286 2010.

[31]   C. Graf, L. Eitzen, and J. Maas, "Multilevel high voltage converter driving dielectric elastomer generators," *Power Electronics and Applications (EPE 2011), Proceedings of the 2011-14th European Conference on* pp. 1 - 10 2011.

[32]   C. Graf, J. Maas, and D. Schapeler, "Optimized energy harvesting based on electro active polymers," *Solid Dielectrics (ICSD), 2010 10th IEEE International Conference,* July 2010.

[33]   E. Dimopoulos and S. Munk-Nielsen, "A tapped-inductor buck-boost converter for a dielectric electroactive polymer generator," in *Applied Power Electronics Conference and Exposition (APEC), 2014 Twenty-Ninth Annual IEEE*, 2014, pp. 3125-3131.

[34]   L. Eitzen, C. Graf, and J. Maas, "Bidirectional HV DC-DC converters for energy harvesting with dielectric elastomer generators," in *Energy Conversion Congress and Exposition (ECCE), 2011 IEEE*, 2011, pp. 897-901.

[35]   J. Maas and T. Hoffstadt, "Model-based control of a dual active bridge for bidirectional feeding of DEAP transducers," in *Advanced Intelligent Mechatronics (AIM), 2014 IEEE/ASME International Conference on*, 2014, pp. 310-315.

[36]   L. Eitzen, C. Graf, and J. Maas, "Modular converter system for driving DEAP transducers," in *Power Electronics and Motion Control Conference (EPE/PEMC), 2012 15th International*, 2012, pp. LS7d.3-1-LS7d.3-8.

[37]   H. Lina, Z. Zhe, and M. A. E. Andersen, "Detailed behavior analysis for high voltage bidirectional flyback converter driving DEAP actuator," in *Industrial Electronics Society, IECON 2013 - 39th Annual Conference of the IEEE*, 2013, pp. 625-630.

[38]   M. Gerber, J. A. Ferreira, I. W. Hofsajer, and N. Seliger, "Interleaving optimization in synchronous rectified DC/DC converters," in *Power Electronics Specialists Conference, 2004. PESC 04. 2004 IEEE 35th Annual*, 2004, vol. 6, pp. 4655-4661 Vol.6.

[39]   C. Chin and M. A. Knights, "Interleaving technique in distributed power conversion systems," *Circuits and Systems I: Fundamental Theory and Applications, IEEE Transactions on,* vol. 42, no. 5, pp. 245-251, 1995.

[40]   D. J. Perreault and J. G. Kassakian, "Distributed interleaving of paralleled power converters," *Circuits and Systems I: Fundamental Theory and Applications, IEEE Transactions on,* vol. 44, no. 8, pp. 728-734, 1997.

[41]   P. Xu, R. Yuan-Chen, M. Ye, and F. C. Lee, "A family of novel interleaved DC/DC converters for low-voltage high-current voltage regulator module applications," in *Power Electronics Specialists Conference, 2001. PESC. 2001 IEEE 32nd Annual*, 2001, vol. 3, pp. 1507-1511 vol. 3.

[42]   J. Rodriguez, J.-S. Lai, and F. Z. Peng, "Multilevel inverters: a survey of topologies, controls, and applications," *Industrial Electronics, IEEE Transactions,* vol. vol.49, pp. pp. 724- 738, Aug 2002.

[43]   A. Pandey, B. Singh, B. N. Singh, A. Chandra, K. Al-Haddad, and D. P. Kothari, "A Review of Multilevel Power Converters," *IE (I) Journal – EL,* vol. 86, no. March 2006, 2003.

[44]   Z. Fan, F. Z. Peng, and Q. Zhaoming, "Study of the multilevel converters in DC-DC applications," *Power Electronics Specialists Conference, 2004. PESC 04. 2004 IEEE 35th Annual* vol. 2, pp. 1702 - 1706 Vol.2 2004.

[45]   H. Holtz, W. Lotzkat, and K. H. Werner, "A high-power multi transistor inverter uninterruptible power supply system," *IEEE Transactions on Power Electronics,* pp. 278-285, 1988.

[46]   F. Defay, A. M. Llor, and M. Fadel, "Direct Control Strategy for a Four-Level Three-Phase Flying-Capacitor Inverter," vol. 57, no. 7, p. 2248, 2010.

[47]   W. Liu, G. Yan, Y. Chen, X. Zhang, and Y. Han, "A generic PWM control method for flying capacitor inverter," vol. 3, p. 1690 Vol.3, 2004.

[48]   L. Xu and V. G. Agelidis, "Active capacitor voltage control of flying capacitor multilevel converters," vol. 151, no. 3, p. 320, 2004.

[49]   L. Zhang, S. J. Watkins, and C. Duan Qi, "Control of Multilevel Flying Capacitor Inverters for High Performance," vol. 3, p. 6, 2006.

[50]   Y. Zhang and L. Sun, "An Efficient Control Strategy for a Five-Level Inverter Comprising Flying-Capacitor Asymmetric H-Bridge," vol. 58, no. 9, p. 4009, 2011.

[51]   T. A. Meynard, M. Fadel, and N. Aouda, "Modeling of multilevel converters," *Industrial Electronics, IEEE Transactions on,* vol. 44, no. 3, pp. 356 - 364, 1997.

[52]   C. Feng and V. G. Agelidis, "PWM Control Methods for Five-level Flying Capacitor Multilevel Converters," 7th International Conference on Modeling and Simulation of Electric Mashines, Converters and Systems (ELECTRIMACS 2002), 2002.

[53]   F. Chunmei, L. Jun, and V. G. Agelidis, "A novel voltage balancing control method for flying capacitor multilevel converters," vol. 2, p. 1184 Vol.2, 2003.

[54]   S. Thielemans, A. Ruderman, B. Reznikov, and J. A. A. Melkebeek, "Self-precharge for single-leg odd-level multilevel converter," *Power Electronics, Machines and Drives (PEMD 2010), 5th IET International Conference,* pp. pp.1-6, 19-21 April 2010.

[55]   S. Busquets-Monge, S. Alepuz, and J. Bordonau, "A novel bidirectional multilevel boost-buck dc-dc converter," p. 714, 2009.

[56]   N. Schibli, "Symmetrical multilevel converter with two quadrant dc-dc feedings," PhD thesis, EPFL, Thesis Nr. 2220, 2000.

[57]   F. Krismer, J. Biela, and J. W. Kolar, "A comparative evaluation of isolated bi-directional DC/DC converters with wide input and output voltage range," *Industry Applications Conference, 2005. Fourtieth IAS Annual Meeting. Conference Record of the 2005,* vol. vol.1, no. 2-6 Oct. 2005, pp. 599- 606, 2005.

[58]   Y. Wang, S. W. H. de Haan, and J. A. Ferreira, "Optimal operating ranges of three modulation methods in dual active bridge converters," in *Power Electronics and Motion Control Conference, 2009. IPEMC '09. IEEE 6th International*, 2009, pp. 1397-1401.

[59]   F. Krismer, S. Round, and J. W. Kolar, "Performance Optimization of a High Current Dual Active Bridge with a Wide Operating Voltage Range," in *Power Electronics Specialists Conference, 2006. PESC '06. 37th IEEE*, 2006, pp. 1-7.

[60]   G. Ortiz, C. Gammeter, J. W. Kolar, and O. Apeldoorn, "Mixed MOSFET-IGBT bridge for high-efficient Medium-Frequency Dual-Active-Bridge converter in Solid State Transformers," in *Control and Modeling for Power Electronics (COMPEL), 2013 IEEE 14th Workshop on*, 2013, pp. 1-8.

[61] F. Krismer and J. W. Kolar, "Closed Form Solution for Minimum Conduction Loss Modulation of DAB Converters," *Power Electronics, IEEE Transactions on,* vol. 27, no. 1, pp. 174-188, 2012.

[62] F. Krismer and J. W. Kolar, "Efficiency-Optimized High-Current Dual Active Bridge Converter for Automotive Applications," *Industrial Electronics, IEEE Transactions on,* vol. 59, no. 7, pp. 2745-2760, 2012.

[63] D. Costinett, D. Maksimovic, and R. Zane, "Design and Control for High Efficiency in High Step-Down Dual Active Bridge Converters Operating at High Switching Frequency," *Power Electronics, IEEE Transactions on,* vol. 28, no. 8, pp. 3931-3940, 2013.

[64] D. Costinett *et al.*, "Active balancing system for electric vehicles with incorporated low voltage bus," in *Applied Power Electronics Conference and Exposition (APEC), 2014 Twenty-Ninth Annual IEEE*, 2014, pp. 3230-3236.

[65] F. K. P. A. M. Bezerra, R. M. Burkart and J. W. Kolar, "Bidirectional isolated non-resonant DAB DC-DC converter for ultra-wide input voltage range applications," *2014 International Power Electronics and Application Conference and Exposition,* pp. 1038-1044, 2014.

[66] F. J. a. J. Biela, "Combined Phase-Shift and Frequency Modulation of a Dual-Active-Bridge AC–DC Converter With PFC," *IEEE Transactions on Power Electronics,* vol. 31, no. 12, pp. 8387-8397, Dec. 2016.

[67] R. M. B. a. J. W. Kolar, "Comparative η– ρ– σ Pareto Optimization of Si and SiC Multilevel Dual-Active-Bridge Topologies With Wide Input Voltage Range," *IEEE Transactions on Power Electronics,* vol. 32, no. 7, pp. 5258-5270, July 2017.

[68] Y. T. a. H. M. X. Han, "The switching frequency optimization of dual phase shift control for dual active bridge DC-DC converter," *IECON 2017 - 43rd Annual Conference of the IEEE Industrial Electronics Society,* pp. 1610-1615, 2017.

[69] S. Allebrod, R. Hamerski, and R. Marquardt, "New transformerless, scalable Modular Multilevel Converters for HVDC-transmission," in *Power Electronics Specialists Conference, 2008. PESC 2008. IEEE*, 2008, pp. 174-179.

[70] R. Marquardt, "Modular Multilevel Converter: An universal concept for HVDC-Networks and extended DC-Bus-applications," in *Power Electronics Conference (IPEC), 2010 International*, 2010, pp. 502-507.

[71] A. Lesnicar and R. Marquardt, "An innovative modular multilevel converter topology suitable for a wide power range," in *Power Tech Conference Proceedings, 2003 IEEE Bologna*, 2003, vol. 3, p. 6 pp. Vol.3.

[72] W. Kawamura, M. Hagiwara, and H. Akagi, "Experimental verification of a modular multilevel cascade converter based on triple-star bridge-cells (MMCC-TSBC) for motor drives," in *Future Energy Electronics Conference (IFEEC), 2013 1st International*, 2013, pp. 454-459.

[73] W. Kawamura, M. Hagiwara, and H. Akagi, "A broad range of frequency control for the modular multilevel cascade converter based on triple-star bridge-cells (MMCC-TSBC)," in *Energy Conversion Congress and Exposition (ECCE), 2013 IEEE*, 2013, pp. 4014-4021.

[74]   N. Kawakami *et al.*, "Development of a 500-kW Modular Multilevel Cascade Convertor for battery energy storage systems," in *Energy Conversion Congress and Exposition (ECCE), 2013 IEEE*, 2013, pp. 3375-3381.

[75]   M. Hagiwara, I. Hasegawa, and H. Akagi, "Start-Up and Low-Speed Operation of an Electric Motor Driven by a Modular Multilevel Cascade Inverter," *Industry Applications, IEEE Transactions on,* vol. 49, no. 4, pp. 1556-1565, 2013.

[76]   J. A. Ferreira, "The Multilevel Modular DC Converter," *Power Electronics, IEEE Transactions on,* vol. 28, no. 10, pp. 4460-4465, 2013.

[77]   T. Todorcevic and J. A. Ferreira, "A DC-DC modular multilevel topology for electrostatic renewable energy converters," in *Industrial Electronics Society, IECON 2013 - 39th Annual Conference of the IEEE*, 2013, pp. 175-180.

[78]   X. Z. a. T. C. Green, "The Modular Multilevel Converter for High Step-Up Ratio DC–DC Conversion," *IEEE Transactions on Industrial Electronics,* vol. 62, no. 8, pp. 4925-4936, 2015.

[79]   J. Reinert, A. Brockmeyer, and R. W. A. A. D. Doncker, "Calculation of losses in ferro- and ferrimagnetic materials based on the modified Steinmetz equation," *IEEE Transaction on Industry Applications,* vol. Vol. 37, 2001.

[80]   C. P. Steinmetz, "On the law of hysteresis," *Proceedings of the IEEE,* vol. 72, no. 2, pp. 197-221, 1984.

[81]   J. Walter and R. W. De Doncker, "High-power galvanically isolated DC/DC converter topology for future automobiles," in *Power Electronics Specialist Conference, 2003. PESC '03. 2003 IEEE 34th Annual*, 2003, vol. 1, pp. 27-32 vol.1.

[82]   H. van Hoek, M. Neubert, A. Kroeber, and R. W. De Doncker, "Comparison of a single-phase and a three-phase dual active bridge with low-voltage, high-current output," in *Renewable Energy Research and Applications (ICRERA), 2012 International Conference on*, 2012, pp. 1-6.

[83]   R. W. A. A. De Doncker, D. M. Divan, and M. H. Kheraluwala, "A three-phase soft-switched high-power-density DC/DC converter for high-power applications," *Industry Applications, IEEE Transactions,* vol. vol.27, pp. pp.63-73, Jan/Feb 1991.

[84]   M. N. Kheraluwala, R. W. Gascoigne, D. M. Divan, and E. D. Baumann, "Performance characterization of a high-power dual active bridge DC-to-DC converter," *Industry Applications, IEEE Transactions on,* vol. 28, no. 6, pp. 1294-1301, 1992.

[85]   K. Florian, "Modeling and Optimization of Bidirectional Dual Active Bridge DC–DC Converter Topologies," PhD thesis, ETH Zurich, Diss. ETH No. 19177, 2010.

[86]   Z. Haihua and A. M. Khambadkone, "Hybrid Modulation for Dual Active Bridge Bi-Directional Converter With Extended Power Range For Ultracapacitor Application," *Industry Applications Society Annual Meeting, 2008. IAS '08. IEEE,* no. 5-9 Oct. 2008, pp. 1 - 8, 2008.

[87]   https://www.infineon.com/.

[88]   http://www.cree.com/.

[89]   R. W. Erickson and D. Maksimovic, *Fundamentals of Power Electronics*. Springer, 2001.

[90]   http://www.ferroxcube.com/.

Abbreviations

2QC	Two-quadrant converter
ac	Alternating current
AMA	All modules active
CMC	Cascaded multilevel converter
DAB	Dual active bridge
dc	Direct current
DCM	Discontinuous conduction mode
DCMC	Diode-clamped multilevel converter
DEAP	Dielectric electroactive polymer
EAP	Electroactive polymer
FCMC	Flying-capacitor multilevel converter
FPGA	Field-programmable gate array
HB	Half-bridge
IGBT	Insulated-gate bipolar transistor
IPOS	Input parallel output series
M2C	Modular multilevel converter
M2DC	Modular multilevel dc-dc converter
MOSFET	Metal-oxide-semiconductor field-effect transistor
MPC	Multiphase converter
MPE	Maximum efficiency point
MSE	Modified Steinmetz equation
PEC	Power electronic converter
PS-SPWM	Phase-shifted sinusoidal pulse width modulation
PTO	Power take-off
PWM	Pulse width modulation
SiC	Silicon carbide
SMA	Step module activation
VMA	Variable module activation
WEC	Wave energy converter
ZCS	Zero current switching
ZVS	Zero voltage switching

List of Publications

As author:

[1]   T. Todorčević, R. van Kessel, J. Ferreira and P. Bauer, "A Modulation Strategy for Wide Voltage Output in DAB-Based DC–DC Modular Multilevel Converter for DEAP Wave Energy Conversion," *IEEE Journal of Emerging and Selected Topics in Power Electronics,* vol. vol. 3, no. no. 4, pp. pp. 1171-1181, Dec. 2015.

[2]   T. Todorcevic, P. Bauer and J. Ferreira, "Efficiency improvements using SiC MOSFETs in a dc-dc modular multilevel converter for renewable energy extraction," *2014 16th International Power Electronics and Motion Control Conference and Exposition,* pp. pp. 514-520, 2014.

[3]   T. Todorčević, P. Bauer, J. Ferreira and R. van Kessel, "A modulation strategy for wide voltage output in DAB based DC-DC modular multilevel converter," *IECON 2014 - 40th Annual Conference of the IEEE Industrial Electronics Society,* pp. pp. 4514-4520, 2014.

[4]   T. Todorčević and J. A. Ferreira, "A DC-DC modular multilevel topology for electrostatic renewable energy converters," *IECON 2013 - 39th Annual Conference of the IEEE Industrial Electronics Society,* pp. pp. 175-180, 2013.

[5]   T. Todorčević, P. Bauer, J. Ferreira and R. van Kessel, "Bidirectional modular multilevel DC-DC converter control and loss modeling for energy extraction from Electro Active Polymer Wave Energy generator," *2013 IEEE ECCE Asia Downunder,* pp. pp. 461-467, 2013.

[6]   T. Todorčević, P. Bauer, J. Ferreira and R. van Kessel, "Bidirectional modular multilevel DC-DC converter control and efficiency improvements through separate module control method," *2013 IEEE Energy Conversion Congress and Exposition,* pp. pp. 2038-2043, 2013.

[7]   T. Todorcevic, P. Bauer and J. Ferreira, "Comparison of bidirectional medium-voltage DC-DC converters for energy harvesting using dielectric elastomers," *Proceedings - PCIM Europe: International Exhibition and Conference for Power Electronics, Intelligent Motion, Renewable Energy and Energy Management,* pp. pp. 1-8, 2013.

As Co-Author:

[8]   S. Rodrigues, A. Papadopoulos, E. Kontos, T. Todorcevic and P. Bauer, "Steady-State Loss Model of Half-Bridge Modular Multilevel Converters," *IEEE Transactions on Industry Applications,* vol. vol. 52, no. no. 3, pp. pp. 2415-2425, May-June 2016.

[9] A. Papadopoulos, S. Rodrigues, E. Kontos, T. Todorcevic, P. Bauer and R. Pinto, "A fast steady-state loss model of a modular multilevel converter for optimization purposes," *2015 9th International Conference on Power Electronics and ECCE Asia (ICPE-ECCE Asia),* pp. pp. 1967-1975, 2015.

[10] A. Papadopoulos, S. Rodrigues, E. Kontos, T. Todorcevic, P. Bauer and R. Pinto, "Collection and transmission losses of offshore wind farms for optimization purposes," *2015 IEEE Energy Conversion Congress and Exposition (ECCE),* pp. pp. 6724-6732, 2015.

[11] D. Voglitsis, V. Prasanth, T. Todorčević and P. Bauer, "Theoretical analysis and experimental investigation of high frequency bidirectional CPT system," *2014 IEEE Transportation Electrification Conference and Expo (ITEC),* pp. pp. 1-8, 2014.

[12] D. Voglitsis, T. Todorčević, V. Prasanth and P. Bauer, "Loss model and control stability of bidirectional LCL-IPT system," *2014 4th International Electric Drives Production Conference (EDPC),* pp. pp. 1-8, 2014.

Acknowledgements

Work toward obtaining a Ph.D. degree requires high level of personal dedication and focus. From the beginning to the end, this journey had many curves, ups and downs... mostly ups I would say. On this path, many persons contributed in different ways and, here, I would like to show my appreciation to them.

Firstly, I would like to express my gratitude to professors who significantly contributed to my work during the Ph.D. I am deeply grateful to my promotor and supervisor Prof. Pavol Bauer for giving me the opportunity to pursue a Ph.D. on this very interesting topic and for all effort, guidance and research freedom entrusted to me. Thank you for all the advices and thoughts on scientific and technical subjects, but also on various topics on management, geography and history of the world, that I have truly enjoyed and learned. I would like to sincerely thank my promotor Prof. Jan A. Ferreira for numerous meetings on technical subjects, for all ideas, guidance, scientific conversations and highly respected advices and criticism. You greatly influenced the way I developed myself as a researcher.

Important part of the Ph.D. is the collaboration. Here, I would like to thank Rick who was important link between university and industry from project definition to final reports, as well as for being a very good host in Monaco during project meetings. I express my gratitude to Philippe and Ambroise for their support, valuable technical information and feedbacks.

I acknowledge my doctoral examination committee, Prof. C.G.E. Wijnands, Prof. H. Polinder, Prof. P.T.M. Vaessen, Prof. V. Katić and Prof. A.H.M. Smets, for spending their valuable time and giving valuable comments and suggestions on my draft thesis.

I would like to thank all the colleagues with whom I have shared office space over the years: Rodrigo, Xun, Minos, Carlos, Tsegay and Laurens. Thank you for all the sessions on knowledge transfer, valuable scientific feedbacks, great trips we had together and for making our office an enjoyable place. Also, I would like to thank other colleagues from the group for having all the interesting research discussions, sharing experience, lunches enriched with chats and jokes, short breaks, out-of-office time: Ilija, Ivan, Miloš, Johan, Yeh, Gautham, Balazs, Rick, Martin, Prasanth, Silvio, Anoop, Emile, Swagat, Marcelo, Wim, Jianing, Wenbo, Dionisis, Mladen, Laura, Samuel, Andreja, Udai and Victor. I sincerely gratitude all the group supporting stuff: Bart, Sharmila, Laura, Ellen, Harrie, Rob, Kasper and Joris, but also Prof. J. Popović-Gerber, Mark Gerber, Prof. H. Polinder and Sjoerd de Haan for all the discussions and advices. Many thanks go to Wiljan Vermeer for translating the thesis summary and the propositions into Dutch.

An essential part of my life are my friends. Here, I would like to thank all the dear people who made my stay in The Netherlands enjoyable: Ilija, Nikola, Tijana, Stojan, Blagoj, Ilinka,

Biography

Todor Todorčević was born in Valjevo, Serbia, on April 23rd, 1985. In 2004 he started his studies in Electrical Engineering and in 2009 he obtained his diploma of Master in Electrical and Computer Engineering from University of Novi Sad, Serbia. In December 2010, he started working as a Ph.D. researcher on the Marie Curie project Wavetrain2 at the Electrical Sustainable Energy (ESE) department of Delft University of Technology, The Netherlands. The project was carried out in collaboration with the SBM Offshore company.